

REPORT DOCUMENTATION PAGE

Form Approved
OMB No. 0704-0188

Public reporting burden for this collection of information is estimated to average 1 hour per response, including the time for reviewing instructions, searching existing data sources, gathering and maintaining the data needed, and completing and reviewing the collection of information. Send comments regarding this burden estimate or any other aspect of this collection of information, including suggestions for reducing this burden, to Washington Headquarters Services, Directorate for Information Operations and Reports, 1215 Jefferson Davis Highway, Suite 1202, Arlington, VA 22202-4302, and to the Office of Management and Budget, Paperwork Reduction Project (0704-0188), Washington, DC 20503.

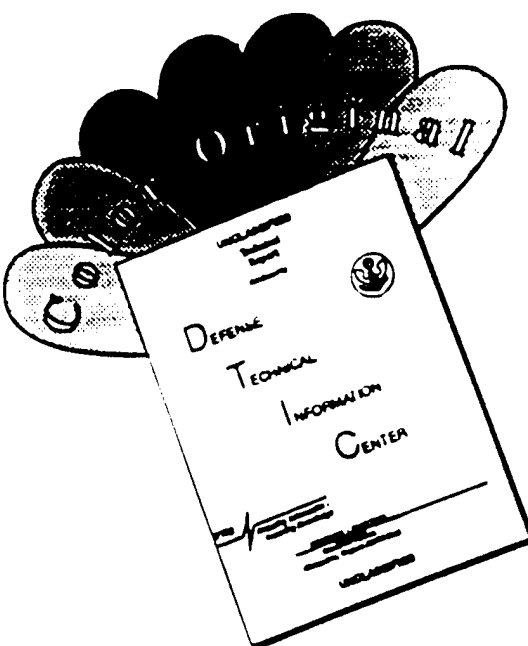
1. AGENCY USE ONLY (Leave blank)	2. REPORT DATE	3. REPORT TYPE AND DATES COVERED
	2/29/96	Final Technical Report
4. TITLE AND SUBTITLE		5. FUNDING NUMBERS
(U) Droplet-Turbulence Interactions Over A Wide Spectral Range		PE - 61102F PR - 2308 SA - BS G - F49620-93-1-0028
6. AUTHORS		W.A. Sirignano S.E. Elghobashi I. Kim M. Masoudi
7. PERFORMING ORGANIZATION NAME(S) AND ADDRESS(ES)		
Department of Mechanical and Aerospace Engineering University of California, Irvine Irvine, CA 92717-3975		
8. SPONSORING/MONITORING AGENCY NAME(S) AND ADDRESS(ES)		
AFOSR/NA 110 Duncan Avenue, Suite B115 Bolling AFB DC 20332-0001		
9. SPONSORING/MONITORING AGENCY REPORT NUMBER		
NA 93-1-0028		
11. SUPPLEMENTARY NOTES		
12a. DISTRIBUTION/AVAILABILITY STATEMENT		
Approved for public release; distribution is unlimited		
13. ABSTRACT (Maximum 200 words)		
<p>The unsteady, three-dimensional, incompressible, viscous flow interactions between a single vortex tube or a pair of vortex tubes advected by a uniform free stream and a spherical particle held fixed in space were investigated numerically for a range of particle Reynolds numbers between 20 and 100. Useful correlations of lift coefficient, moment coefficient, and drag coefficient with velocity fluctuation, Reynolds number, offset distance, and initial vortex size were obtained and reported. A new mechanism based upon droplet lift has been suggested for the dispersion of sprays. The mechanism of particle dispersion due to the interaction with small vortices was quite different from that due to the interaction with a large vortex. A new improved equation of particle (or droplet) motion has been demonstrated to be superior to the previously proposed equations of particle motion. The droplet heating study showed the very significant response of the Nusselt number to vortical disturbances. The new computations with thermocapillary effects showed another coupling of the fluid motion to the thermal field.</p>		
14. SUBJECT TERMS		15. NUMBER OF PAGES
Droplet or Spray and Vortex or Turbulence; Droplet Dispersion		92
16. PRICE CODE		
17. SECURITY CLASSIFICATION OF REPORT	18. SECURITY CLASSIFICATION OF THIS PAGE	19. SECURITY CLASSIFICATION OF ABSTRACT
Unclassified	Unclassified	Unclassified
20. LIMITATION OF ABSTRACT		
UL		

DISCLAIMER NOTICE



**THIS DOCUMENT IS BEST
QUALITY AVAILABLE. THE
COPY FURNISHED TO DTIC
CONTAINED A SIGNIFICANT
NUMBER OF PAGES WHICH DO
NOT REPRODUCE LEGIBLY.**

DISCLAIMER NOTICE



**THIS DOCUMENT IS BEST
QUALITY AVAILABLE. THE COPY
FURNISHED TO DTIC CONTAINED
A SIGNIFICANT NUMBER OF
COLOR PAGES WHICH DO NOT
REPRODUCE LEGIBLY ON BLACK
AND WHITE MICROFICHE.**

Final Technical Report

**DROPLET-TURBULENCE INTERACTIONS
OVER A WIDE SPECTRAL RANGE**

AFOSR Grant/Contract No. F49620-93-1-0028

November 1, 1992 to January 31, 1996

Prepared by :

Professor W. A. Sirignano, Principal Investigator

Professor S. E. Elghobashi

Dr. I. Kim

Mr. M. Masoudi

Department of Mechanical and Aerospace Engineering

University of California, Irvine, California

Submitted to: Dr. J. Tishkoff, Program Manager

February 29, 1996

Table of Contents

I ABSTRACT	1
II OBJECTIVES	1
III SUMMARY OF RESEARCH	2
1. Unsteady flow interactions between an advected cylindrical vortex tube and a sphere	2
2. Unsteady flow interactions between a pair of advected vortex tubes and a sphere	2
3. Interactions of an array of vortex tubes of like rotation with a moving sphere	3
4. The motion of a sphere in unsteady axisymmetric flows at moderate Reynolds numbers	4
5. The motion of a sphere in unsteady three-dimensional flows at moderate Reynolds numbers	5
6. Unsteady thermal interactions between a liquid sphere and an advecting vortex	7
Acknowledgement	8
References	8
IV PROFESSIONAL PERSONNEL	9
V PUBLICATIONS	9
VI PRESENTATIONS	11
VII INTERACTIONS	12
ADDENDA	
1. Unsteady flow interactions between a pair of advected vortex tubes and a rigid sphere.	
2. The motion of a spherical particle in unsteady flows at moderate Reynolds numbers.	
3. The influence of an advecting vortex on the heat transfer to a liquid droplet.	

I ABSTRACT

The unsteady, three-dimensional, incompressible, viscous flow interactions between a single vortex tube or a pair of vortex tubes advected by a uniform free stream and a spherical particle held fixed in space were investigated numerically for a range of particle Reynolds numbers between 20 and 100. Useful correlations of lift coefficient, moment coefficient, and drag coefficient with velocity fluctuation, Reynolds number, offset distance, and initial vortex size were obtained and reported. A new mechanism based upon droplet lift has been suggested for the dispersion of sprays. The mechanism of particle dispersion due to the interaction with small vortices was quite different from that due to the interaction with a large vortex. A new improved equation of particle (or droplet) motion has been demonstrated to be superior to the previously proposed equations of particle motion. The droplet heating study showed the very significant response of the Nusselt number to vortical disturbances. The new computations with thermocapillary effects showed another coupling of the fluid motion to the thermal field.

II OBJECTIVES

The objectives of this research program are to investigate the interactions of vaporizing droplets with a turbulent field of the type encountered in gas turbine combustors. It is intended to develop predictive capability through the use of correlations. There is special interest in the important and challenging high-frequency end of the energy spectrum where turbulent length scales are comparable to droplet size. The full Navier-Stokes equations were numerically solved and a simple mathematical description for the turbulent velocity fluctuation was employed. In the mathematical description, turbulent-like fluctuations were simulated in a controlled way by introducing cylindrical vortices which have a length scale of the order of that of the droplet and a strength corresponding to a turbulent velocity fluctuation. From the calculations, instantaneous lift, drag, and torque coefficients, Nusselt number, and Sherwood number are determined. Time-averaged values of these fluctuating quantities are also determined. Such quantities should be useful in modelling droplet dispersion and modifications of heating and vaporization rates due to turbulence.

III SUMMARY OF RESEARCH

1. Unsteady flow interactions between an advected cylindrical vortex tube and a sphere

As a preliminary step towards understanding the interactions between a droplet and the carrier turbulent flow, the unsteady, three-dimensional, incompressible, viscous flow interactions between a vortical (initially cylindrical) structure advected by a uniform free stream and a spherical particle held fixed in space was investigated numerically for a range of particle Reynolds numbers between 20 and 100. The counter-clockwise rotating vortex tube was initially located ten sphere radii upstream from the sphere center.

The computed velocity and pressure fields provided the lift, moment, and drag coefficients on the sphere as a function of time for a range of offset distance, vortex core radius, and maximum fluctuation velocity induced by the vortex tube. Initially, the lift forces were positive due to upwash on the sphere, then became negative due to downwash and higher fluid velocity near the bottom of the sphere when the vortex tube passed the sphere.

Varying the vortex core radius showed that the maximum positive and negative lift coefficients and the rms lift coefficient were *linearly* proportional to the *circulation* of the vortex tube at small values of the core radius while they were linearly proportional only to the maximum fluctuation velocity and *independent* of the core radius at large values of the core radius. For mid-range values of the core radius, they depended on both the core radius and the maximum fluctuation velocity (or equivalently both the core radius and circulation). Some interesting unsteady flow phenomena occurred in the near wake on the passage of the vortex tube.

The paper [1] describing the details of this work was published in the *Journal of Fluid Mechanics* and was appended to the September 1995 Progress Report.

2. Unsteady flow interactions between a pair of advected vortex tubes and a sphere

The interactions between a pair of vortex tubes and a sphere were studied in order to generalize the findings from the previous investigation.

When the top and bottom (see Figure 2 of Reference 2) vortex tubes have positive and negative circulations, respectively, the magnitude of the induced velocity due to the vortex tubes is added to the base flow velocity along the stagnation streamline. This causes the pressure at the stagnation point and the shear stresses in the upper and lower left regions to be higher than those of the axisymmetric flow past a sphere, thus increasing the drag. On the other hand, when the top and bottom vortex tubes have negative and positive

circulations, respectively, the induced velocity due to the vortex tubes is subtracted from the base flow velocity along the stagnation streamline. This causes the pressure at the stagnation point and the shear stresses in the upper and lower left regions to be lower than those of the axisymmetric flow past a sphere, thus reducing the drag. The lift and moment are zero for this symmetric configuration.

The interactions between a sphere and like-rotating a pair of cylindrical vortex tubes initially located ten radii upstream from the center of the sphere were investigated. The lift and moment coefficients of the sphere interacting with a pair of vortex tubes as a function of time are nearly identical, respectively, to those of the sphere interacting with a single vortex tube if the separation distance between the tube centers is less than $2\sqrt{\sigma}$ vortex tube diameter for the lift coefficient and less than $\sqrt{\sigma}$ vortex tube diameter for the moment coefficient; here, v_{maxt} instead of v_{max} is used in the case of a pair of vortex tubes, where v_{max} is the maximum induced velocity due to one vortex without presence of the other, v_{maxt} is the total maximum induced velocity due to the pair of vortices and σ is the radius of initial vortex core normalized by the sphere radius. In particular, lift and moment coefficients are linearly proportional to the maximum induced velocity. The moment coefficient is negligible compared to the lift coefficient.

The paper [2] describing this work in detail was submitted to the *International Journal of Multiphase Flow* and is appended to this report.

3. Interactions of an array of vortex tubes of like rotation with a moving sphere

The two-dimensional trajectories of a spherical particle interacting with an array of vortices whose sizes are comparable to the sphere size were examined. The time-dependent drag and lift forces (Ref. [1]) for the case of a sphere interacting with a single vortex were used to calculate the two-dimensional trajectory of a moving spherical particle interacting with an array of vortex tubes of like rotation. The results show that the shear flow across the sphere induced by a vortex tube is responsible for the net deflection of a sphere interacting with an array of vortex tubes. Thus, the sphere eventually deflects in the direction of increasing relative velocity. The deflection ratio (ratio of sphere final location in z and x directions) of the sphere increases with decreasing initial Reynolds number and with decreasing density ratio. However, the total deflection increases with increasing the initial Reynolds number and the density ratio because higher momentum causes the sphere to travel farther. See Ref. [2] for details.

4. The motion of a sphere in unsteady axisymmetric flows at moderate Reynolds numbers

A turbulent flow possesses a wide spectrum of eddy sizes. In order to enhance the understanding of droplet motion in a turbulent flow, we have been investigating the motion of a *freely moving* sphere interacting with a large vortex tube whose size is of the order of an integral length scale, i.e. at the other end of the spectrum relative to the previous cases. The goals of this study are to derive not only a relationship of interaction between a small droplet and a large vortex but also an accurate equation for the motion of a spherical droplet in finite-Reynolds-number turbulent flows.

The equations of sphere motion proposed by previous workers were examined and compared with the results of the full Navier-Stokes equations for unsteady, axisymmetric flow around a *freely moving* sphere initially injected into a stationary or oscillating fluid. As a result, we have proposed a modified equation of sphere motion and demonstrated its superiority to the previously proposed equations of sphere motion. This work is described in the AIAA preprint 96-0081 by Kim, Elghobashi & Sirignano [3] which is an addendum to this report.

The new equation contains a modified history term with an integral kernel weighted by the acceleration magnitude and a new term accounting for the initial velocity difference between the particle and the carrier fluid. The weighting function contains the time derivative of the relative velocity M_{A1} and the ratio ϕ_r of M_{A2} to M_{A1} . M_{A1}, M_{A2} , and ϕ_r are defined by

$$M_{A1} = \frac{2a}{|\mathbf{u} - \mathbf{v}|^2} \left| \frac{d|\mathbf{u} - \mathbf{v}|}{dt} \right| ; \quad M_{A2}(t) = \frac{(2a)^2}{|\mathbf{u} - \mathbf{v}|^3} \left| \frac{d^2|\mathbf{u} - \mathbf{v}|}{dt^2} \right|$$

$$\phi_r(t) = \frac{M_{A2}}{M_{A1}}$$

These dimensionless groups can be introduced through dimensional analysis to obtain the forces on the particle of unsteady motion.

The new proposed equation of particle motion is expressed as:

$$m_p \frac{dv}{dt} = \frac{1}{2} C_{Dstd} \pi a^2 \rho_f |\mathbf{u} - \mathbf{v}| (\mathbf{u} - \mathbf{v}) + \frac{1}{2} m_f \left(\frac{Du}{Dt} - \frac{dv}{dt} \right) + m_f \frac{Du}{Dt} + (m_p - m_f)g + 6\pi\mu_f a \int_0^t K(t - \tau, \tau) \frac{d(\mathbf{u} - \mathbf{v})}{d\tau} d\tau + 6\pi\mu_f a K_1(t) [\mathbf{u}(0) - \mathbf{v}(0)] \quad (1a)$$

with the integral kernel $K(t - \tau, \tau)$ given by

$$K(t - \tau, \tau) = \left\{ \left[\frac{\pi(t - \tau)\nu_f}{a^2} \right]^{0.5/c_1} + G(\tau) \left[\frac{\pi |u(\tau) - v(\tau)|^3}{2 a \nu_f f_H^3(Re_t)} (t - \tau)^2 \right]^{1/c_1} \right\}^{-c_1} \quad (1b)$$

$$G(\tau) = \frac{1}{1 + \beta \sqrt{M_{A1}(\tau)}} \quad (1c)$$

$$\beta = \frac{c_2}{1 + \phi_r \phi_r^{c_4} / [c_3(\phi_r + \phi_r^{c_4})]} \quad (1d)$$

$$f_H = 0.75 + c_5 Re_t(\tau), \quad (1e)$$

and with the function $K_1(t)$ given by

$$K_1(t) = \left\{ \left[\frac{\pi t \nu_f}{a^2} \right]^{0.5/c_1} + G_1 \left[\frac{\pi |u(0) - v(0)|^3}{2 a \nu_f f_H^3(Re_{to})} t^2 \right]^{1/c_1} \right\}^{-c_1} \quad (1f)$$

$$G_1 = \frac{1}{1 + c_6 Re_{to}^{-0.25} (\rho_r + 0.5)^{-0.5}}, \quad (1g)$$

where $Re_t = |u(\tau) - v(\tau)|2a/\nu_f$ and $Re_{to} = |u(0) - v(0)|2a/\nu_f$.

The six constants c_i ($i = 1, \dots, 6$) in the above equations are determined by comparing the solutions from Equation (1a) with those from the Navier-Stokes equations and given for $0 \leq \omega' < \infty$ by

$$c_1 = 2.5, \quad c_5 = 0.126, \quad c_6 = 15,$$

$$c_2 = 45.5, \quad c_3 = 0.03, \quad c_4 = 0.1. \quad (1h)$$

ω' is the dimensionless frequency of the flow and defined by $\omega' = \omega a/v_o$, where v_o is the initial injection velocity of the particle.

For low frequencies $0 < \omega' < 0.3$, the following values of c_2 , c_3 , and c_4 provide slightly better results than those of Equation (1h). The values of c_1 , c_5 , and c_6 are kept fixed as in (1h).

$$c_2 = 13.9, \quad c_3 = 0.12, \quad c_4 = 0.5. \quad (1i)$$

5. The motion of a sphere in unsteady three-dimensional flows at moderate Reynolds numbers

In order to extend Equation (1a) to a vector form for two- or three-dimensional case, we consider the time-dependent, three-dimensional, incompressible, flow around a small spherical solid particle injected into a counter-clockwise rotating large vortex which is

located at the origin of the coordinates (X, Y, Z) fixed in space. The net gravity force acting on the particle is neglected. The origin of a nonrotating noninertial reference frame (x, y, z) is chosen at the center of the particle.

All the variables are nondimensionalized using the sphere radius a as the characteristic length and the initial injection velocity of the sphere v_o as the characteristic velocity.

The initial velocity field induced by the vortex tube is analytically computed by considering the evolution of a point vortex and is given by

$$U_\phi = \frac{\Gamma}{2\pi R} [1 - \exp(-\frac{R^2}{4\nu_f(t + t_o)})] \quad (2a)$$

$$t_o = \frac{\sigma_o^2}{4\nu_f (1.12)^2}, \quad (2b)$$

where $R = \sqrt{X^2 + Y^2}$, $\phi = \arctan Y/X$, and t_o is a parameter defined by initial size of the vortex core (σ_o) and the fluid kinematic viscosity (ν_f).

The initial maximum induced velocity u_{maxo} due to the vortex tube occurs on the edge of the vortex core $R = \sigma_o$ at $t = 0$ and can be obtained from Equation (2a). The pressure field due to the vortex tube is also analytically computed by integrating the radial component of the momentum equation which is $\rho U_\phi^2/R = \partial p/\partial R$.

It is assumed that the vortex is so large that the flow field induced by the vortex is not affected by the moving sphere except locally in the region around the sphere. The boundary conditions of the flow field are obtained by superimposing the sphere velocity and the induced velocity due to the vortex tube at the computational outer boundary relative to the sphere, and the pressure field due to the vortex tube is also imposed at the computational outer boundary. Although the flow computation is three-dimensional, the particle path remains in the plane of symmetry ($X - Y$ plane). Therefore, the trajectory computation is made for the case of a freely moving particle in two-dimensions. After computing the forces on the sphere, the deceleration (or acceleration) of the sphere is obtained via Newton's second law of motion, and then the new location of the sphere is obtained.

Preliminary results of the large vortex study show that the lift force on the particle is much smaller than that due to the small vortices with the same maximum induced velocity. Our direct solution of the three-dimensional Navier-Stokes equations over a freely moving particle confirms that due mainly to the drag force, the particle travels in a curved trajectory that depends on the direction of vortex rotation and the Stokes number of the particle. This indicates that the mechanism of particle dispersion due to the interaction with small vortices is quite different from that due to the interaction with a large vortex. Refer to [3] for details of the work.

6. Unsteady thermal interactions between a liquid sphere and an advecting vortex

Within the scope of our planned study on the thermal aspects of the droplet-turbulence interaction, we have completed quantifying the effect of an advecting vortex near the droplet on the droplet convective heat transfer. Also, prompted by recent publications, we have included the effect of Marangoni stresses in the dynamics. We intend to study in the future a coupled effect of the gas field temperature stratification and advecting vortical structures on the droplet heating.

We successfully completed our study of droplet heating influenced by an advecting vortex. Since the problem is unsteady by nature, we paid particular attention to time-averaged and root-mean-squared values of the droplet Nusselt number. All the existing available correlation⁴ for droplet heat transfer are for a steady axisymmetric flow; thus, they can not be applied when there exists asymmetry or unsteadiness in the gas field, such as that induced by an advecting vortex. It is noteworthy that, in practice, droplets do not experience a perfectly symmetric field but an asymmetric one. This introduces serious limitation on the applicability of existing correlations.

We have successfully produced the first known self-similar correlation predicting the unsteady droplet heating due to the advecting vortex; this finding well complements the existing correlations for droplet heating in symmetric flows. Our results include several interesting observations: first, self-similarity in the droplet heating exists for the unsteady droplet-vortex interaction; second, it is not the vortex initial distance from the droplet but its ratio to the vortex core size that plays a major role in droplet heating; this ratio determines whether the droplet would be embedded inside the vortex inner core in the course of the interaction. Third, if this ratio is larger than a certain value, the droplet heating merely depends on the vortex circulation and, surprisingly, has little dependence on the vortex distance from the droplet. The role of the flow Reynolds number itself appears to be crucial as well: droplet heating shows stronger response to the *same* vortex in a flow with a higher Reynolds number. In general, it was found that the droplet Nusselt number variation is qualitatively similar to change in droplet fluid dynamic properties observed in previous studies of this research group; coupling between the fluid dynamics and heat transfer phenomena justifies this similarity. These findings [4] were presented at the 24th Aerospace Sciences Meeting, January 1996, in Reno, Nevada, and are attached to this report as an Addendum. An expanded version of this paper is being submitted to the International Journal of Heat and Mass transfer for publication.

Recent publications by Niazmand *et al* [5] and Shih and Megaridis [6] signify some importance of thermocapillary effects on the droplet response in a hot gaseous axisymmetric environment. Most previous publications in the field of spray droplet computations have neglected these effects. Following these findings, we included the effect of surface tension, the so-called Marangoni stresses, in the force-balance at the droplet-gas interface and so

in the numerical simulation. This task is completed and the code has been benchmarked after this upgrade. We have successfully reproduced the effect of thermocapillary stresses on the droplet internal circulation underlined in said publications, the most important ones being the slow-down on the droplet internal circulation and the detachment and gradual disappearance of the droplet wake.

Droplets in a combustion chamber do not experience a perfectly-uniform temperature field but a spatially varying one. The effect of temperature stratification, coupled with the influence of vortical structures, therefore pose interesting questions on the dynamics of the said coupling; e.g. it is unclear how the vortex-induced variations in the droplet heating [4] will change due to gas-field temperature stratification. In spite of the serious practical applications for such findings, there exist no available information shedding light on the coupled temperature stratification-vortical stratification effects on droplet heating.

We therefore intend to study simultaneous thermal and aerodynamic effects of the temperature field and the vortical structures on the droplet heating in a combustion chamber. We assume a profile for the surrounding gas temperature whose length-scale of its gradient is comparable to that of the droplet and the vortex. Otherwise stated, there are three important length scales in this study: the vortex core size , droplet size, and the length scale for the temperature stratification. Special interest occurs when the three length scales are comparable.

Acknowledgement

The support of the San Diego Supercomputer Center and the San Diego Supercomputer Center under a block grant of the Office of Academic Computing of UCI are gratefully appreciated.

References

1. Kim, I., Elghobashi S. & Sirignano, W. A. (1995) Unsteady flow interactions between an advected cylindrical vortex tube and a spherical particle. *J. Fluid Mech.* **288**, 123-155.
2. Kim, I., Elghobashi S. & Sirignano, W. A. (1995) Unsteady flow interactions between a pair of advected vortex tubes and a rigid sphere. submitted to *Int. J. Multiphase flow* (also see AIAA preprint 95-0105).
3. Kim, I., Elghobashi S. & Sirignano, W. A. (1996) The motion of a spherical particle in unsteady flows at moderate Reynolds numbers. 34th AIAA Aerospace Sciences Meeting, Paper 96-0081.

4. Masoudi, M. & Sirignano, W.A. (1996) The influence of an advecting vortex on the heat transfer to a liquid droplet. 34th AIAA Aerospace Sciences Meeting, Paper 96-0087.
5. Niazmand, H., Shaw, B.D., Dwyer, H.A., and Aharon, I. (1995) Effects of Marangoni convection on transient droplet evaporation. *Combust. Sci. and Tech.* **103**, 219.
6. Shih, A.N., Megaridis, C.M. (1996) Thermocapillary flow effects on convective droplet evaporation. *Intl J. Heat and Mass Transfer.* **39**, 2, 247-57.

IV PROFESSIONAL PERSONNEL

W. A. Sirignano, Professor, Principal investigator.

S. E. Elghobashi, Professor.

I. Kim, Postdoctoral research associate, January 1990 – present.

M. Masoudi, research assistant, Ph.D. student.

V PUBLICATIONS

The following papers and book articles have resulted at least partially from the research performed under this research program.

1. Sirignano, W. A., 1993, Computational spray combustion, in Numerical Modelling in Combustion, (Chung, T. J. ed.), Hemisphere Publication.
2. Chiang, C. H. & Sirignano, W. A., 1993, Interacting, convecting, vaporizing fuel droplets with variable properties. *Int. J. Heat Mass Transfer* **36**, No. 4, 875-886.
3. Chiang, C. H. & Sirignano, W. A., 1993, Axisymmetric calculations of three-droplet interactions. *Atomization and Sprays* **3**, No. 1, 91-107.
4. Kim, I., Elghobashi S. & Sirignano, W. A., 1993, Three-dimensional flow over two spheres placed side by side. *J. Fluid Mech.* **246**, 465-488.
5. Sirignano, W. A., 1993, Fluid dynamics of sprays (invited Freeman Scholar paper). *J. Fluids Engineering* **115**, No. 3, 345-378.

6. Sirignano, W. A., Delplanque, J. P., Chiang, C. H. & Bhatia R., 1995 Liquid propellant droplet vaporization, Driving mechanism for rocket combustion instability *AIAA progress in Aeronautics and Astronautics book series 169* (V. Yang, ed). Also presented at the First International Symposium on Liquid Rocket Combustion Instability.
7. Kim, I., Elghobashi, S. & Sirignano, W. A., 1993, Three-dimensional flow interactions between a cylindrical vortex tube and a sphere, presented at the *46th Annual Meeting of the Division of Fluid Dynamics of American Physical Society*, Albuquerque, New Mexico.
8. Kim, I., Elghobashi S. & Sirignano, W. A. 1995 Unsteady flow interactions between a pair of advected cylindrical vortex tubes and a rigid sphere. *33rd AIAA Aerospace Sciences Meeting*, paper 95-0105.
9. Kim, I., Elghobashi, S. & Sirignano, W. A., 1995, A modified equation for the motion of a spherical particle, presented at the *48th Annual Meeting of the Division of Fluid Dynamics of American Physical Society*, Irvine, California.
10. Masoudi, M., & Sirignano, W. A., 1995, Vortex-droplet interaction influencing convective droplet heat transfer, presented at the *48th Annual Meeting of the Division of Fluid Dynamics of American Physical Society*, Irvine, California.
11. Kim, I., Elghobashi S. & Sirignano, W. A. 1995 Unsteady flow interactions between an advected cylindrical vortex tube and a spherical particle. *J. Fluid Mech.* **288**, 123-155.
12. Kim, I., Elghobashi S. & Sirignano, W. A. 1996 Unsteady flow interactions between a pair of advected vortex tubes and a rigid sphere. submitted to *Int. J. Multiphase flow*.
13. Kim, I., Elghobashi S. & Sirignano, W. A. 1996 The motion of a spherical particle in unsteady flows at moderate Reynolds numbers. *34th AIAA Aerospace Sciences Meeting*, Paper 96-0081.
14. Masoudi, M. & Sirignano, W.A. 1996 The influence of an advecting vortex on the heat transfer to a liquid droplet. *34th AIAA Aerospace Sciences Meeting*, Paper 96-0087.
15. Duvvur, A., Chiang C. H. & Sirignano, W. A. 1996 Oscillatory fuel droplet vaporization: driving mechanism for combustion instability. *J. Propulsion and Power*, to appear March 1996.

16. Silverman I. & Sirignano, W. A. 1994 Multi-droplet interaction effects in dense sprays. *Int. J. Multiphase flow* **20**, No. 1, 99-116.
17. Kim, I., Elghobashi S. & Sirignano, W. A. 1996 On the equation of motion of a spherical particle. to be submitted to *J. Fluid Mech.*
18. Masoudi, M. & Sirignano, W.A. 1996 The influence of an advecting vortex on the heat transfer to a liquid droplet. to be submitted to *Int. J. Heat Mass Transfer*.

VI PRESENTATIONS

1. Sirignano, W. A., "Fluid dynamics of sprays (invited Freeman Scholar paper)," presented at the ASME Winter Annual Meeting, Anaheim, CA, Nov. 1992.
2. Sirignano, W. A., "Liquid propellant droplet vaporization, Driving mechanism for rocket combustion instability," presented at the *First International Symposium on Liquid Rocket Combustion Instability*, 1993.
3. Kim, I., "Three-dimensional flow interactions between a cylindrical vortex tube and a sphere," presented at the 46th Annual Meeting of the Division of Fluid Dynamics, American Physical Society, Albuquerque, New Mexico, November 21-23, 1993.
4. Kim, I., "A modified equation for the motion of a spherical particle," presented at the 48th Annual Meeting of the Division of Fluid Dynamics, American Physical Society, Irvine, California, November 1995.
5. Masoudi, M., "Vortex-droplet interaction influencing convective droplet heat transfer," presented at the 48th Annual Meeting of the Division of Fluid Dynamics, American Physical Society, Irvine, California, November 1995.
6. Kim, I., "The motion of a spherical particle in unsteady flows at moderate Reynolds numbers," presented at the 34th AIAA Aerospace Sciences Meeting, Reno, Nevada, January 1996.
7. Masoudi, M., "The influence of an advecting vortex on the heat transfer to a liquid droplet," presented at the 34th AIAA Aerospace Sciences Meeting, Reno, Nevada, January 1996.

ADDENDUM TO SECTIONS 2 and 3

UNSTEADY FLOW INTERACTIONS BETWEEN A PAIR OF ADVECTED VORTEX TUBES AND A RIGID SPHERE

by

Inchul Kim, Said Elghobashi, and William A. Sirignano

Department of Mechanical and Aerospace Engineering

University of California, Irvine

Irvine, CA 92717

Abstract

An idealized representation of the interaction of spherical particles with turbulent eddies of comparable length scale is considered by means of a three-dimensional, unsteady finite-difference Navier-Stokes solution of the interaction between a fixed rigid sphere and a pair of advecting vortex tubes. First, a doubly symmetric interaction with vortices of opposite rotation is considered. The resulting time-dependent drag differs from the drag in axisymmetric flows; however, the lift and torque on the sphere remain zero. Next, an interaction with two vortices of like rotation is studied. Here, non-zero lift and torque, as well as drag deviation from the axisymmetric case occur and would result in a deflection in the trajectory of a nonfixed sphere. The flow in this case behaves like that of a single vortex. Finally, a linear array of like-rotating vortices, interacting with a freely moving sphere, is considered. The two-dimensional deflection depends strongly upon the sphere/fluid density ratio and initial sphere Reynolds number. Lift and moment coefficients are shown to be linearly proportional to the maximum induced velocity due to the vortices. Moment coefficients are an order of magnitude less than lift coefficients.

Key Words: unsteady flow over a sphere, sphere-vortex interaction

Contents

1	Introduction	2
2	Problem statement and formulation	4
2.1	Flow description	4
2.2	Governing equations and boundary conditions	6
2.3	Numerical solution	7
3	Results and discussion	8
3.1	Interactions of a sphere and a pair of vortex tubes with top-positive and bottom-negative circulations	8
3.2	Interactions of a sphere and a pair of vortex tubes with top-negative and bottom-positive circulations	11
3.3	Interactions of a pair of vortex tubes of like rotation and a sphere	12
3.3.1	Flow structure	13
3.3.2	Lift, moment, and drag coefficients and effect of tube circulation . .	15
3.3.3	Effects of the size and the offset distance of the vortex tubes	18
3.3.4	Effects of Reynolds number	20
3.4	Interactions of an array of vortex tubes of like rotation and a moving sphere	22
4	Conclusions	26
5	References	29

1 Introduction

The interactions between vortical structures and spherical particles or droplets is of primary practical interest in many particle-laden flows. These interactions modify the trajectories of individual particles and cause dispersion in a spray or cloud. Also, they can modify heat and mass transfer rates for the particles. There has been long-term interest in the effects of turbulent eddies which contain most the energy and whose sizes are orders of magnitude larger than the particle diameters.

However, a need exists to study the interactions of a particle with vortical structures that are smaller than, comparable in size to, or only a few times larger than the sphere. These small structures have the potential to produce the largest modifications to the boundary layer and near wake of the sphere.

In this paper, an idealized representation of those interactions is made by considering the viscous, incompressible, unsteady, three-dimensional flow associated with a pair of initially cylindrical vortex tubes advecting past the sphere. This study builds upon the previous study of Kim, Elghobashi & Sirignano (1995), hereafter identified as KES. In that paper, the authors examined the unsteady, three-dimensional interactions between a single advected cylindrical vortex tube and a fixed spherical particle whose diameter is of the same order of magnitude as the initial diameter of the vortex. That study served as a first step towards better understanding the two-way interactions between small-scale turbulence and the particle. Here we extend this work, with the same goal, to study the interactions between a pair of advected vortex tubes and a stationary spherical particle.

In the earlier study (KES) the particle Reynolds number based on the freestream velocity and the particle diameter was in the range $20 \leq Re \leq 100$. The initial size of the cylindrical vortex tube was in the range $0.25 \leq \sigma \leq 4$, where σ is the radius of the vortex tube normalized by that of the particle. We found that the maximum positive lift coefficient and the rms lift coefficient of the sphere are *linearly* proportional to the

circulation of the vortex tube at small values of σ . However, at large values of σ , they are linearly proportional to the maximum induced velocity due to the vortex tube but *independent* of σ .

In the present paper, both like-rotating and opposite-rotating vortical pairs are considered. In the opposite-rotating case, only a symmetric configuration (see figure 1) is examined. Asymmetric configurations with opposite rotations are left for future studies. More attention is given to like-rotating pairs because they have the greatest effect on lift and torque. We expect, therefore, that deflections in the trajectories and dispersion of sprays and clouds will be greater in this case of like rotation. The case of a "train" of vortices advecting past the sphere at prescribed intervals is also examined.

Our specific objectives are to study:

1. the detailed flow field behavior during interaction of a pair of vortex tubes with each other and with the sphere,
2. the relationship between the lift coefficient of the sphere and the maximum induced velocity due to the two vortex tubes,
3. the modification of the drag force caused by the interactions,
4. the effects of Reynolds number, vortex size, and initial offset distance of the vortex, and
5. the sphere deflection caused by the interaction with the vortices.

The detailed study of the interactions between the particle and the unsteady velocity field provides fundamental information about the flow behavior that can be used in developing mathematical models for particle-laden flows. The next section provides a mathematical description of the flow considered, the governing equations, and the numerical solution procedure. Section 3 discusses the results including the numerical accuracy

issues, the effects of varying the parameters listed above, and the trajectories of a moving spherical particle interacting with an array of vortex tubes of like rotation as an extension of the results of KES and the present study. Section 4 provides a summary and concluding remarks.

2 Problem statement and formulation

2.1 Flow description

Consider the time-dependent, three-dimensional, incompressible, viscous flow interactions between a pair of symmetric, initially cylindrical vortex tubes and a solid sphere. The vortex tubes are moving with the laminar free stream, and a sphere is suddenly placed and held fixed in space as shown in figure 1. The initial offset distance, d'_{off} , denotes the shortest distance between the initial vortical axis and the y-z plane which is parallel to the free stream. All the variables are nondimensionalized using the sphere radius a'_o as the characteristic length and U'_∞ as the characteristic velocity, where the superscript $'$ denotes dimensional quantity. The two vortex tubes, having equal diameters of the order of the sphere diameter, are initially located ten sphere-radii upstream from the center of the sphere. The effects of the vortex tubes on the sphere are negligible at this initial distance because the magnitude of the initial velocity field induced by the vortex tubes is less than 2 percent of the free stream velocity. Far upstream, the flow is uniform with constant velocity $U'_\infty \mathbf{k}$ parallel to the y-z plane. There is one symmetry plane, the x-z plane, as seen in figure 1. A second symmetry plane (y-z) exists only when the two vortices have opposite rotations. Our general formulation does not take advantage of this second symmetry.

Note that, later in section 3.4, the fixed sphere results will be employed in a moving sphere trajectory analysis.

Two coordinate systems are used in our formulation following KES: the Cartesian coordinates (x, y, z) and the nonorthogonal generalized coordinates (ξ, η, ζ). The origin of the former coincides with the sphere center. ξ is the radial, η is the angular, and ζ is the azimuthal coordinates. The nonorthogonal generalized coordinate system can be easily adapted to three-dimensional arbitrary geometries. In the present study, a spherical domain is used, and the grid reduces to an orthogonal, spherical grid. The grids are denser near the surface of the spherical particle, and the grid density in the radial direction is controlled by the stretching function developed by Vinokur (1983). Due to symmetry, the physical domain is reduced to a half spherical space. The domain of the flow is bounded by $1 \leq \xi \leq N_1$, $1 \leq \eta \leq N_2$, $1 \leq \zeta \leq N_3$, where $\xi = 1$ and N_1 correspond, respectively, to the sphere surface and the farfield boundary surrounding the sphere; $\eta = 1$ and N_2 denote, respectively, the positive z -axis (downstream) and the negative z -axis (upstream); $\zeta = 1$ and N_3 refer, respectively, to the x - z plane in the positive x -direction and the x - z plane in the negative x -direction. Uniform spacing ($\delta\xi = \delta\eta = \delta\zeta = 1$) is used, for convenience, for the generalized coordinates.

The initial vortex tubes have a small core region with a radius σ (normalized by the sphere radius). This core is defined such that the initial velocity induced by the vortex tube approaches zero as the distance from the center of the vortex tube goes to zero, and at distances much greater than σ , the induced velocity approaches that of a point vortex. We use the vortex tube construction of Spalart (1982), which has the following stream function:

$$\psi_v(x, z, t = 0) = -\frac{\Gamma_j}{2\pi} \ln[(x - x_j)^2 + (z - z_j)^2 + \sigma^2],$$

where Γ_j is the nondimensional circulation around the vortex tube at radius σ and at the initial time. Γ_j is positive when the vortex tube rotates counterclockwise, and x_j and z_j denote the location of the center of the vortex tube. The circulation around a circular path far away from the center of the vortex is given by $\Gamma_{jt} = 2\Gamma_j$. Each vortex tube can be viewed as an evolution from the point vortex due to the cylindrical viscous diffusion.

The stream function for a pair of vortex tubes is given by

$$\psi_v(x, z, t = 0) = - \sum_{j=1}^2 \frac{\Gamma_j}{2\pi} \ln[(x - x_j)^2 + (z - z_j)^2 + \sigma^2] \quad (1)$$

2.2 Governing equations and boundary conditions

The continuity and momentum equations and the initial and boundary conditions are nondimensionalized using the sphere radius a'_o as the characteristic length and U'_∞ as the characteristic velocity.

$$\nabla \cdot V = 0 \quad (2a)$$

$$\frac{\partial V}{\partial t} + \nabla \cdot V V = -\nabla p + \frac{2}{Re} \nabla^2 V \quad (2b)$$

The governing equations (2a) and (2b) are cast in terms of the generalized coordinates (ξ, η, ζ) to treat a three-dimensional body of arbitrary shape. The numerical integration is performed using a cubic computational mesh with equal spacing ($\delta\xi = \delta\eta = \delta\zeta = 1$).

The velocities on the sphere surface are zero due to the no-slip condition, and the pressure on the sphere is obtained from the momentum equation. The detailed equations describing the boundary and initial conditions are given in KES and thus will not be repeated here. The only difference from KES is that the initial pressure is estimated as zero over the whole computational domain. This estimation is corrected by the pressure correction equation and iteration procedure (see section 2.3 for details).

The only nondimensional groupings appearing in the equations and initial and boundary constraints are the sphere Reynolds number, vortex tube radius, offset distance, and vortex circulation (or vortex Reynolds number).

The equations evaluating the drag, lift, and moment coefficients are given in KES and thus will not be repeated here. The lift force is assumed positive when it is directed

toward the positive x-axis. Due to symmetry, only the y-component of the moment is non-zero and is assumed positive in the counter-clockwise direction.

2.3 Numerical solution

A three-dimensional, implicit, finite-difference algorithm has been developed to solve simultaneously the set of the discretized partial differential equations. The method is based on an Alternating-Direction-Predictor-Corrector (ADPC) scheme to solve the time-dependent Navier-Stokes equations. ADPC is a slight variation of Alternating-Direction-Implicit (ADI) method and implemented easily when embedded in a large iteration scheme (Patnaik 1986, Patnaik *et al.* 1986). The control volume formulation is used to develop the finite-difference equations from the governing equations with respect to the generalized coordinates (ξ, η, ζ) . One of the advantages of the control volume formulation is that mass and momentum are conserved over a single control volume, and hence the whole domain regardless of the grid fineness. An important part of solving the Navier-Stokes equations in primitive variables is the calculation of the pressure field. In the present work, a pressure correction equation is employed to satisfy indirectly the continuity equation (Anderson *et al.* 1984). The pressure correction equation is of the Poisson type and is solved by the Successive-Over-Relaxation (SOR) method.

The overall solution procedure is based on a cyclic series of guess-and-correct operations. The velocity components are first calculated from the momentum equations using the ADPC method, where the pressure field at the previous time step is employed. This estimate improves as the overall iteration continues. The pressure correction is calculated from the pressure correction equation using the SOR method, and new estimates for pressure and velocities are obtained. This process continues until the solution converges at each time step.

3 Results and discussion

In subsections (3.1) and (3.2), we discuss the three-dimensional interactions of a sphere and a pair of vortex tubes of opposite rotation. In subsection (3.3), we examine the three-dimensional interactions of a sphere and a pair of vortex tubes of like rotation. In subsection (3.4), we investigate the trajectories of a moving sphere interacting with an array of vortex tubes of like rotation.

Testing the accuracy of our numerical solution has been performed and discussed earlier in KES. The $51 \times 51 \times 51$ grid is used in the following calculations. The run for the interaction between a single vortex tube and a sphere at Reynolds number 100 with the $51 \times 51 \times 51$ grid required 4.95 mega words, a dimensionless time step of $\Delta t = 0.002$, and a total time of 4 cpu hours on Cray C-90 for the final time of $t_f = 24.5$. Each time step takes about 1.18 cpu seconds.

3.1 Interactions of a sphere and a pair of vortex tubes with top-positive and bottom-negative circulations

We consider the interactions of a pair of vortex tubes advected by the free stream and a sphere suddenly placed in the flow and held fixed in space. The two cylindrical vortex tubes are initially of the same size and rotating opposite to each other with top-positive and bottom-negative circulations as shown in figure 1. The y-z plane is half way between the two tubes so that the offset distance of one vortex tube is the negative of the offset distance of the other. The center of the each vortex tube is located at 10 sphere-radii upstream from x-y plane containing the center of the sphere. The base case calculation is that of $Re = 100$, $d_{off} = \pm 1.5$, and $\sigma = 1$.

Initially, each vortex tube has its maximum induced velocity v_{max} located at the edge of the core. Because the velocity and vorticity fields induced by one vortex tube influence

those by the other, the total maximum induced velocity, $v_{max,t}$, due to the two vortex tubes depends on their size and separation distance and is in the range $0 \leq v_{max,t} \leq 2v_{max}$. The total maximum induced velocity $v_{max,t}$ equals zero when $|d_{off}| = 0$, $2v_{max}$ when $|d_{off}| = \sigma$, and v_{max} when $|d_{off}| \gg 1$. For example, $v_{max,t}$ is 0.738 for $v_{max} = 0.4$, $d_{off} = \pm 1.5$, and $\sigma = 1$. The base case calculation is that of $Re = 100$, $d_{off} = \pm 1.5$, and $\sigma = 1$. Note that the lift and torque on the sphere are zero due to the flow symmetry in upper and lower regions of the sphere

In order to describe the flow structure, we first consider the pseudo-streamlines and vorticity contours in the x-z symmetry plane, defined as the *principal plane*, where the strongest interactions occur between the vortical structures and the sphere. The line connecting the front and rear stagnation points in the standard axisymmetric flow over a single sphere, which is the $x = 0$ line in the principal plane, will be used as a reference line. We refer to the region above that line as the ‘upper’ region and that below the line as the ‘lower’ region.

The pseudo-streamlines are obtained from the pseudo-stream function which is defined by assuming that the velocity field in the principal plane does not change in the direction normal to that plane and by using the two-dimensional stream function definition. The sphere surface in the principal plane is used as a reference streamline ($\psi_{ps} = 0$). We note that a real stream function ψ cannot be defined and calculated from the velocity in the principal plane due to the existence of a divergence associated with the third component of velocity. Nevertheless, for descriptive purposes only, it is convenient to use the two-dimensional stream function definition to present descriptions of the flow pattern.

Figures 2(a)-(f) display the pseudo-streamlines (left column) and the contour lines of y-component vorticity (right column) in the principal plane at $t = 0, 3, 6, 9, 12$, and 15 for $Re = 100$, $d_{off} = \pm 1.5$, $\sigma = 1$ with $v_{max,t} = 0.738$ ($v_{max} = 0.4$). The contour values of the pseudo-streamlines are $0, \pm 0.02, \pm 0.1, \pm 0.3$. The contour values of the vorticity are $\pm 0.4, \pm 0.8, \pm 1.4, \pm 2$, with the highest magnitude at the sphere surface.

Comparing the vorticity contours in figures 2(a)-(f) with those of the single vortex tube in figure 5 of KES, we see that the two vortex tubes move downstream faster than the single vortex. This additional acceleration occurs because the velocity magnitude at the center of each vortex tube equals that of the base flow plus that induced by the other vortex tube.

The distance between the top pseudo-streamline and the bottom pseudo-streamline in figures 2(a)-(c) is narrower on the segment connecting the vortex tube centers than any other place along the stagnation pseudo-streamline. This indicates that the velocity near the middle of the segment between the vortex tube centers is higher than any other place along the stagnation pseudo-streamline. The induced velocity due to the vortex tubes is added to the base flow near the stagnation pseudo-streamline.

Figure 3 shows the drag coefficients of the sphere as a function of time for the same parameters as above. The drag coefficients are obtained with four different total maximum induced velocities due to the vortex tubes, $v_{maxt} = 0.185, 0.369, 0.554$, and 0.738 ($v_{max} = 0.1, 0.2, 0.3$, and 0.4). The temporal behavior of the drag coefficients is different from that of the case of the pair of vortex tubes of like rotation as will be shown in section 3.3. The time-averaged value of the deviation of the drag coefficient from that of the axisymmetric flow past a sphere for all values of v_{maxt} is not negligible and increases linearly with v_{maxt} . The time-averaged drag coefficient $C_{D,ave}$ may be expressed by

$$C_{D,ave} = C_{D,axi} + \beta v_{maxt}, \quad (3)$$

where the constant $\beta = 0.27$, and $C_{D,axi}$ is the time averaged value of the drag coefficient in the case of axisymmetric flow ($v_{maxt} = 0$). The drag coefficients reach their maximum at about $t = 9$ (see figure 3). The maximum drag coefficient $C_{D,max}$ can be expressed approximately by equation (3) but with $\beta = 1.05$, and $C_{D,axi}$ here is the local value of the axisymmetric drag coefficient at the time of $C_{D,max}$. Because the top and bottom vortex tubes have positive and negative circulations, respectively, the induced velocity due to the

vortex tubes adds its magnitude to the base flow along the stagnation pseudo-streamline. This increased velocity causes the pressure at the stagnation point and the shear stresses in the upper and lower left regions to be higher than those of the axisymmetric flow past a sphere. As a consequence, the drag is increased.

3.2 Interactions of a sphere and a pair of vortex tubes with top-negative and bottom-positive circulations

We consider the same initial flow geometry and parameters as those in section 3.1 but for a pair of vortex tubes with top-negative and bottom-positive circulations.

Figures 4(a)-(f) display the pseudo-streamlines (left column) and the contour lines of y -component vorticity (right column) in the principal plane at $t = 0, 3, 6, 9, 12$, and 15 for $Re = 100$, $d_{off} = \pm 1.5$, $\sigma = 1$ with $v_{max,t} = 0.738$ ($v_{max} = 0.4$). The contour values of the pseudo-streamlines and the vorticity are the same as those in the previous section.

The vorticity contours in figures 4(a)-(f) show that the two vortex tubes move downstream slower than the single vortex tube in figure 5 of KES. This relative deceleration occurs because the velocity magnitude at the center of each vortex tube equals that of the base flow minus that induced by the other vortex tube.

The distance between the top pseudo-streamline and the bottom pseudo-streamline in figures 4(a)-(c) is broader near the segment connecting the vortex tube centers than any other place along the stagnation streamline. This indicates that the velocity near the middle of the segment between the vortex tube centers is lower than those upstream or downstream of the vortex tubes along the stagnation streamline. The induced velocity due to the vortex tubes is subtracted from the base flow near the stagnation pseudo-streamline.

Figure 5 shows the drag coefficients of the sphere as a function of time for the same parameters as used in section 3.3.1. The drag coefficients are obtained for four different

total maximum induced velocities due to the vortex tubes, $v_{max,t} = 0.185, 0.369, 0.554$, and 0.738 ($v_{max} = 0.1, 0.2, 0.3$, and 0.4). The temporal behavior of the drag coefficients is different from that of the case of the pair of vortex tubes of like rotation as will be shown in section 3.3. The time-averaged value of the deviation of the drag coefficient from that of the axisymmetric flow past a sphere for all values of $v_{max,t}$ is not negligible and decreases linearly as $v_{max,t}$ increases. The time-averaged drag coefficient $C_{D,ave}$ may be expressed by equation (3) but with the proportionality constant $\beta = -0.28$, and $C_{D,axi}$ is the time-averaged value of the drag coefficient in the case of axisymmetric flow ($v_{max,t} = 0$). The drag coefficients reach their minimum at about $t = 11$ (see figure 5). The minimum drag coefficient $C_{D,min}$ can be expressed approximately by equation (3) but with $\beta = -0.95$, and $C_{D,axi}$ here is the local value of the axisymmetric drag coefficient at the time of $C_{D,min}$. Because the top and bottom vortex tubes have negative and positive circulations, respectively, the induced velocity due to the vortex tubes is subtracted from the base flow velocity along the stagnation streamline. This causes the pressure at the stagnation point and the shear stresses in the upper and lower left regions to be lower than those of the axisymmetric flow past a sphere. Thus, the drag is reduced.

3.3 Interactions of a pair of vortex tubes of like rotation and a sphere

We consider the same initial flow geometry and parameters as those in section 3.1 but for a pair of vortex tubes of like rotation. The base case calculation is that of $Re = 100$, $d_{off} = \pm 1.5$, and $\sigma = 1$.

Initially each vortex tube has its maximum induced velocity v_{max} located at the edge of the core. Because the velocity and vorticity fields induced by one vortex tube influence those by the other, the total maximum induced velocity, $v_{max,t}$, due to the two vortex tubes depends on their size and separation distance and is in the range $v_{max} \leq v_{max,t} \leq 2v_{max}$.

$v_{max,t}$ equals $2v_{max}$ when $|d_{off}| = 0$ and equals v_{max} when $|d_{off}| \gg 1$. For example, $v_{max,t} = 0.59$ for $v_{max} = 0.4$, $d_{off} = \pm 1.5$, and $\sigma = 1$.

In subsections 3.3.1 and 3.3.2, we investigate the base case. In subsections 3.3.3 and 3.3.4, we discuss the effects of the size and the offset distance of the vortex tubes and Reynolds number, respectively.

3.3.1 Flow structure

Figures 6(a)-(f) display the pseudo-streamlines (left column) and the contour lines of y -component vorticity (right column) in the principal plane at $t = 1, 6, 10, 15, 21$, and 30 for $Re = 100$, $d_{off} = \pm 1.5$, $\sigma = 1$, and $v_{max,t} = 0.59$ ($v_{max} = 0.4$). The contour values of the pseudo-streamlines are $0, \pm 0.02, \pm 0.1, \pm 0.3$. The contour values of the vorticity are $\pm 0.4, \pm 0.8, \pm 1.4, \pm 2$, with the highest magnitude at the sphere surface. The solid and dotted lines in the figures represent respectively positive and negative values.

The pseudo-streamlines shown in figures 6(a)-(f) resemble closely those for the interaction between a single vortex tube and a sphere which was described in KES. Since the description of the flow structure with the aid of the streamlines is given in KES, it will not be repeated here, and only the vorticity contours will be described here.

The vorticity contours in figures 6(a) and 6(b) show that the vortex tubes not only are advected downstream but also rotate about each other. The contour lines of vorticity in the figures also show that viscous diffusion takes place. It is well known that two co-rotating point vortices located a distance apart in an inviscid flow rotate with constant angular velocity about the point located at the center of the segment connecting them while the separation distance held fixed. On the other hand, when two co-rotating vortex tubes are located a distance apart in an inviscid flow and the separation distance is small enough, they interweave as well as rotate about each other (Zabusky, Hughes & Roberts (1979); Overman and Zabusky (1982); Rangel & Sirignano (1989)).

Figures 6(c) and 6(d) show that the vortex tubes contact the boundary layer of the sphere and go around the bottom of the sphere. The reason for the passage of the vortex tubes around the bottom of the sphere rather than around the top is as follows. When the vortex tubes rotating counter-clockwise come close to the sphere boundary layer, they augment the magnitude of the vorticity in the lower boundary layer and reduce that of the vorticity in the upper boundary layer. Consequently, the vorticity in the lower boundary layer induces a velocity in the downward direction at the location of the vortex tubes with higher magnitude than that induced by the vorticity in the upper boundary layer. This downward induced velocity advects the vortex tubes below the sphere (KES).

Figure 6(e) shows that the pairing vortex tubes merge into one vortex due to the interweaving and the viscosity. Figure 6(f) shows that the vorticity contours around the sphere approach that of the axisymmetric flow as the tubes are advected far downstream.

A three-dimensional view of the pair of vortex tubes is examined by considering the y-component of vorticity vector. Figures 7(a) and 7(b) show the views of a three-dimensional contour surface of $\omega_y = 0.2$ at $t = 6$ and $t = 21$, respectively, for the flow depicted in figure 6. The figures show a view looking down with an acute angle toward the y-z plane. The ellipse in the figures is the boundary of the spherical computational domain viewed at an angle. It appears as a circle when viewed normal to the principal plane. The sphere is at the center of the domain in figures 7(a) and 7(b). Figure 7(a) shows that the two vortex tubes rotate about each other. Figure 7(b) demonstrates that the pair of vortex tubes merge after some time.

The resemblance of the streamline pattern between the case of a pair of vortex tubes and the case of a single vortex tube indicates that the force and moment on the sphere due to a pair of vortex tubes may be close in value to those due to a single vortex tube. In the next subsections, we discuss the lift, moment, and drag coefficients for the pair of vortex tubes and compare them with those for a single vortex tube.

3.3.2 Lift, moment, and drag coefficients and effect of tube circulation

Figure 8 shows the lift coefficients of the sphere as a function of time for $Re = 100$, $d_{off} = \pm 1.5$, and $\sigma = 1$. The lift coefficients are computed for four different total maximum induced velocities $v_{max,t}$ due to the pair of vortex tubes, with magnitudes equal to 0.148, 0.295, 0.443, and 0.590 ($v_{max} = 0.1, 0.2, 0.3$, and 0.4) normalized by free stream velocity. Due to the sudden placement of the sphere into the stream, it takes a short time ($0 < t < 0.8$) for the initial flow perturbations to vanish.

When the pair of vortex tubes approach the sphere ($0 \leq t < 9$), they produce upwash resulting in a positive lift force on the sphere. The maximum positive lift coefficient $C_{L,max1}$ occurs at about $t = 6.8$. On the other hand, when the vortex tubes pass the sphere, they produce downwash and higher fluid velocity near the bottom of the sphere than the top due to the shear flow imposed by the vortex tubes resulting in a negative lift force. The magnitude of the negative lift is greater than the positive lift. The maximum negative lift coefficient $C_{L,max2}$ occurs at about $t = 12.2$. $C_{L,max1}$ and $C_{L,max2}$ are *linearly* proportional to the total maximum induced velocity. The maximum positive lift coefficient $C_{L,max1}$ is expressed by

$$C_{L,max1} = c v_{max,t}, \quad (4)$$

where the proportionality constant $c = 0.88$. The maximum negative lift coefficient $C_{L,max2}$ is also expressed by equation (4) but with $c = -1.62$. After the lift coefficient reaches its maximum negative value, it decays quickly towards zero because the vortex tube vorticity is diffused in the sphere wake. The time averaged lift coefficient (averaged over a time span between $t = 0.8$ and the maximum time 24.5) for all values of $v_{max,t}$ is negative and small ($O(10^{-2})$). As mentioned earlier, the behavior of $C_L(t)$ during the period $0 < t < 0.8$ is influenced by the initial flow perturbation, and thus its value during this initial period is excluded from the averaging process. The root mean square $C_{L,rms}$ of the lift coefficient as a function of time is also linearly proportional to $v_{max,t}$ with $c = 0.7$.

The lift coefficient of the sphere interacting with a single vortex tube as a function of time is also shown as a reference (marked with an asterisk) in figure 8 for $Re = 100$, $d_{off} = 0$, and $\sigma = 1$ with $v_{max,t} = v_{max} = 0.148$. Figure 8 shows that the lift coefficient of the sphere interacting with a pair of like-rotation vortex tubes as a function of time is approximately the same as that of the sphere interacting with a single vortex tube for the parameters given above if the same total maximum induced velocity is used in both cases. The dependency of this phenomenon on the parameters (d_{off} , σ , and Re) will be discussed in the following subsections.

Figure 9 shows the temporal development of the moment coefficients for the sphere under the same conditions as figure 8.

When the vortex tubes pass the sphere, the front stagnation point on the sphere is shifted above the plane $x = 0$ due to the downwash. This causes higher shear stress in the lower left region compared to the upper left region resulting in a positive (counter-clockwise) torque on the sphere. The upward shift of the front stagnation point also causes the shear stress to be higher in the top and upper right regions than in the bottom and lower right regions resulting in a negative torque on the sphere. However, the effect of this negative torque is diminished by the shear flow induced by the vortex tubes across the sphere which produces high shear stress at the bottom of the sphere. As a consequence, a net high positive torque acts on the sphere. The maximum positive moment coefficient $C_{M,max}$ occurs at $t = 11.5$. $C_{M,max}$ is approximately linearly proportional to $v_{max,t}$ with $c = 0.11$.

When the vortex tubes approach the sphere or are relatively far away from the sphere, the effect of the shear flow induced by the vortex tubes across the sphere is small, resulting in a net weak torque on the sphere.

The time averaged moment coefficient for all values of $v_{max,t}$ is positive and small $O(10^{-3})$. The rms moment coefficient $C_{M,rms}$ is approximately linearly proportional to $v_{max,t}$ with $c = 0.043$. We note that the torque depends only the distribution of the shear

stresses ($\tau_{r\theta}$ and $\tau_{r\phi}$) and is relatively small compared to the lift force.

The moment coefficient of the sphere interacting with a single vortex tube as a function of time is also shown as a reference (marked with an asterisk) in figure 9 for $Re = 100$, $d_{off} = 0$, and $\sigma = 1$ with $v_{maxt} = v_{max} = 0.148$. The pattern of the moment coefficient of the sphere interacting with a pair of vortex tubes as a function of time is similar to that of the sphere interacting with a single vortex tube for the parameters given above, but the maximum moment coefficient of the former is lower than that of the latter. This shows that the moment coefficient is more sensitive to the offset distance than the lift coefficient. This will be discussed in the next section in detail.

Figure 10 shows the drag coefficients of the sphere as a function of time for the same conditions as figure 8. The drag coefficients are computed for four different values of v_{mant} as in figure 8, in addition to $v_{maxt} = 0$ which corresponds to the axisymmetric flow without the vortex tubes.

As discussed earlier, the sudden placement of the sphere in the flow results in initially large values of shear stress and pressure on the sphere, and hence a large drag as shown in figure 10. When the vortex tubes approach the sphere, the pressure at the front stagnation point is lower than that of the axisymmetric flow past a sphere due to the low pressure at the center of the vortex tube. Also, the maximum shear stresses in the upper and lower regions of the sphere are lower than those of the axisymmetric flow. This causes the drag on the sphere to be lower than that of the axisymmetric flow without the vortex tube. As the vortex tubes move around the bottom of the sphere, the front stagnation point is shifted above the plane $x = 0$ due to the downwash. Consequently, high pressure and high shear stress act in the upper and lower left regions, respectively. This increases the drag during the period $9 < t \leq 13.4$. For $t > 13.4$, the drag approaches that of the axisymmetric flow as the vortex tube moves further downstream. The time averaged value of the deviation of the drag coefficient from that of the axisymmetric flow past a sphere for all values of v_{max} is nearly zero ($O(10^{-4})$).

The pattern of the drag coefficient of the sphere interacting with a pair of vortex tubes as a function of time is similar to that of the sphere interacting with a single vortex tube for the parameters given above (compared with figure 11 in KES), but the largest deviation of the former from the case of the axisymmetric flow occurs earlier than that of the latter. The reason is that due to the rotation about each other, one of the vortex tubes in the former approaches the sphere faster than the vortex tube in the latter.

3.3.3 Effects of the size and the offset distance of the vortex tubes

The effects of the size of the vortex tubes on the flow field are studied by performing computations similar to those in the previous section for $Re = 100$, $d_{off} = \pm 1.5$, and five different sizes of the vortex tubes, $\sigma = 0.25, 0.5, 2, 3$, and 4 in addition to the base case $\sigma = 1$.

Table 1 shows $C_{L,max1}$, $C_{L,max2}$, $C_{L,rms}$, $C_{M,max}$, and $C_{M,rms}$ as a function of the vortex tube size which covers six different initial radii of the vortex tube, $\sigma = 4, 3, 2, 1, 0.5$, and 0.25 , for $v_{maxt} = 0.1$. Another computation with different v_{maxt} showed that all the lift and moment coefficients are linearly proportional to v_{maxt} at each σ . When $\sigma \geq 2$, $C_{L,max1}$ and $C_{L,rms}$ become *independent* of σ , but the magnitudes of $C_{L,max2}$, $C_{M,max}$, and $C_{M,rms}$ for $\sigma = 4$ are smaller than those for $\sigma = 2$ and 3 . When σ approaches zero, all the coefficients tend to be proportional to (σv_{maxt}) or (σv_{max}) which is proportional to the *circulation* of the vortex tube. For example, $C_{L,rms}$ is expressed by

$$\begin{aligned} C_{L,rms} &= c_1 v_{maxt}, \quad 2 \leq \sigma \leq 4 \\ &= c_2 v_{maxt} \sigma^n, \quad 0.25 \leq \sigma < 2, \quad 0.75 \geq n \geq 0.3, \end{aligned} \quad (5)$$

where the constant $c_1 = 1$ and $c_2 = 0.7$, and n depends on σ and should approach unity as σ reaches zero. For $C_{L,max1}$, $c_1 = 1.1$ and $c_2 = 0.88$. $C_{L,max2}$, $C_{M,max}$, and $C_{M,rms}$ for $\sigma \leq 3$ are also expressed by equation (5) with $c_1 = -2$ and $c_2 = -1.65$, $c_1 = 0.13$ and $c_2 = 0.11$, and $c_1 = 0.053$ and $c_2 = 0.04$, respectively. The time averaged value of the

deviation of the drag coefficient from that of the axisymmetric flow past a sphere for all values of σ is nearly zero ($O(10^{-4})$).

Comparing the results in table 1 (based on v_{maxt}) with those of the sphere interacting with a single vortex tube (KES, table 4 (based on v_{max})), it is found that the magnitudes of the lift coefficients in table 1 are within 2% to 20% of those in KES, with the largest deviation occurring at $\sigma = 0.25$.

Note that $C_{L,max2}$, $C_{M,max}$, and $C_{M,rms}$ for $\sigma = 4$ are, respectively, smaller than those for $\sigma = 2$ and 3 due to the shear flow effect explained in KES.

Now, the effects of the offset distance on the flow field are investigated by varying d_{off} for $Re = 100$ and $\sigma = 4$. The computation was performed for $d_{off} = 0, \pm 1, \pm 2, \pm 3$, and ± 4 in addition to the base case $d_{off} = \pm 1.5$. Note that the case of $d_{off} = 0$ corresponds to the interaction between a *single* vortex tube and a sphere.

It is found that $C_{L,max1}$, $C_{L,max2}$, $C_{L,rms}$, $C_{M,max}$, and $C_{M,rms}$ for each d_{off} are linearly proportional to v_{maxt} as in the case of $d_{off} = \pm 1.5$. The triangular symbols in figure 11 show $C_{L,rms}$ as a function of $|d_{off}|$ for $Re = 100$ and $\sigma = 4$ while the maximum induced velocity (or the circulation) of each vortex tube is kept as a constant, $v_{max} = 0.2$. The triangular symbols show that $C_{L,rms}$ decays rapidly as $|d_{off}| > 0$. On the other hand, the circular symbols in figure 11 show $C_{L,rms}$ as a function of $|d_{off}|$ for $Re = 100$ and $\sigma = 4$ while the total maximum induced velocity due to the two vortex tubes is kept as a constant, $v_{maxt} = 0.2$. The circular symbols show that the magnitudes of the rms lift coefficients for $d_{off} = \pm 1, \pm 1.5, \pm 2, \pm 3$, and ± 4 are close to that for $d_{off} = 0$. The behavior of $C_{L,max1}$ and $C_{L,max2}$ as a function of $|d_{off}|$ is similar to that of $C_{L,rms}$.

Examination of the effect of the offset distance for $\sigma = 1$ and 2 shows that the lift coefficient of the sphere interacting with a pair of vortex tubes as a function of time is nearly identical to that of the sphere interacting with a single vortex tube if the separation distance between the tube centers is less than $2\sqrt{\sigma}$ vortex tube diameter for $Re = 100$ and v_{maxt} instead of v_{max} is used in the former.

The triangular symbols and the circular symbols in figure 12 show $C_{M,rms}$ as a function of $|d_{off}|$ for the same parameters as used for $C_{L,rms}$. Figure 12 shows that the magnitude of the rms moment coefficient decays more rapidly than that of the rms lift coefficient as d_{off} increases. The behavior of $C_{M,max}$ as a function of d_{off} is similar to that of $C_{M,rms}$. The moment coefficient of the sphere interacting with a pair of vortex tubes as a function of time is nearly identical to that of the sphere interacting with a single vortex tube if the separation distance between the tube centers is less than $\sqrt{\sigma}$ vortex tube diameter for $Re = 100$ and v_{maxt} instead of v_{max} is used in the former.

3.3.4 Effects of Reynolds number

Computations like those in section 3.3.2 are made for four different Reynolds numbers in the range of $20 \leq Re \leq 80$, $d_{off} = \pm 1.5$, and $1 \leq \sigma \leq 4$ in addition to the base case $Re = 100$.

A result like that shown in section 3.3.3 for $Re = 100$ is obtained. $C_{L,max1}$ and $C_{L,rms}$ are linearly proportional only to v_{maxt} and independent of σ when $\sigma \geq 2$ at fixed Reynolds number as in the case of $Re = 100$. $C_{L,max1}$ dependence on Reynolds number may be expressed by

$$C_{L,max1} = A v_{maxt} Re^P, \quad (6)$$

where $A = 8.9$ and $P = -0.45$ for $2 \leq \sigma \leq 4$. $C_{L,rms}$ may be also expressed by equation (6) with $A = 8.1$ and $P = -0.45$ for $2 \leq \sigma \leq 4$. $C_{M,max}$ and $C_{M,rms}$ may be also represented by equation (6) with $A = 5.5$ and $P = -0.83$ for the former, and $A = 3.1$ and $P = -0.88$ for the latter for $2 \leq \sigma \leq 3$.

Now, the effect of the offset distance for $20 \leq Re \leq 80$ in addition to the base case $Re = 100$ is discussed.

The triangular symbols in figure 13 show $C_{L,rms}$ as a function of $|d_{off}|$ for $Re = 20$ and $\sigma = 4$ while the maximum induced velocity (or the circulation) of each vortex tube is

kept as a constant, $v_{max} = 0.2$. The triangular symbols show that $C_{L,rms}$ decays rapidly as $|d_{off}| > 0$. On the other hand, the circular symbols show $C_{L,rms}$ as a function of $|d_{off}|$ for $Re = 20$ and $\sigma = 4$ while the total maximum induced velocity due to the two vortex tubes is kept as a constant, $v_{maxt} = 0.2$. The circular symbols show that the magnitudes of the rms lift coefficients for $d_{off} = \pm 2$ and ± 4 are close to that for $d_{off} = 0$. The behavior of $C_{L,max1}$ and $C_{L,max2}$ as a function of $|d_{off}|$ resembles that of $C_{L,rms}$.

The results for the range of σ values indicate that the lift coefficient of the sphere interacting with a pair of like-rotation vortex tubes as a function of time is nearly identical to that of the sphere interacting with a single vortex tube if the separation distance between the tube centers is less than $2\sqrt{\sigma}$ vortex tube diameter for $Re = 20$ and v_{maxt} instead of v_{max} is used in the former case. The same result as above was obtained at different Reynolds numbers, $Re = 40, 60$, and 80 .

The triangular symbols and the circular symbols in figure 14 show $C_{M,rms}$ as a function of $|d_{off}|$ for the same parameters as used for $C_{L,rms}$. The figure shows the magnitude of the rms moment coefficient decays more rapidly than that of the rms lift coefficient as d_{off} increases. The behavior of $C_{M,max}$ as a function of d_{off} resembles that of $C_{M,rms}$. It is found that the moment coefficient of the sphere interacting with a pair of vortex tubes as a function of time is nearly identical to that of the sphere interacting with a single vortex tube if the separation distance between the tube centers is less than $\sqrt{\sigma}$ vortex tube diameter for $Re = 20$ and v_{maxt} instead of v_{max} is used in the former case. The same result as above was obtained at different Reynolds numbers, $Re = 40, 60$, and 80 .

In summary, the comparison of the results from this section with those from the previous section shows that the range of the offset distance for which the lift and moment coefficients of the sphere interacting with a pair of vortex tubes are nearly identical to those of the sphere interacting with a single vortex tube is independent of Reynolds number for $20 \leq Re \leq 100$.

3.4 Interactions of an array of vortex tubes of like rotation and a moving sphere

Our results for the cases of a fixed spherical particle interacting with a single advecting vortex and with an advecting pair of vortices can now be used to calculate the trajectory of a moving spherical particle interacting with an array of like-rotating vortex tubes. Opposite-rotating vortices are less interesting since they produce no lift or deflection. Studying these interactions can improve our understanding of the behavior of a particle (or droplet) interacting with eddies of comparable length scale in a turbulent flow. For this study, the array will be a linear arrangement of single vortices. Since a single vortex and a pair of like-rotating vortices produce comparable effects on the sphere, this choice should not be critical.

Figure 15 shows the initial flow geometry where a spherical particle is injected into an array of infinite number of counter-clockwise rotating vortices which are located on the negative z-axis with center-to-center nondimensional distance of 24. Since the life time of a vortex tube is short ($2\pi\sigma/v_{max}$) compared to the travel time (or life time) of the particle (or droplet), it is assumed that the next vortex with the same strength as the first vortex is generated when the sphere passes the first vortex. The deflection of the moving sphere will cause the offset distance to vary from one collision with a vortex tube to the next. Therefore, d_{off} is a time-dependent quantity.

We assume that the particle is constrained to move only in the x-z plane. The aim is to calculate the trajectory in the two-dimensional plane from the already-known time evolution of $C_D(t)$ and $C_L(t)$ as given by KES. The particle trajectory as a function of time is computed by solving the following system of two ordinary differential equations which are the nondimensional form of the Newton's equation of motion in the z and x directions.

$$\frac{dU_z}{dt} = \frac{3}{8\rho_r} (-C_D(t) \cos\theta - C_L(t) \sin\theta) (U_z^2 + U_x^2) \quad (7a)$$

$$\frac{dU_x}{dt} = \frac{3}{8\rho_r} (-C_D(t) \sin\theta + C_L(t) \cos\theta) (U_z^2 + U_x^2), \quad (7b)$$

where U_z and U_x are, respectively, the sphere velocities in z and x direction, $\tan\theta = U_x/(-U_z)$, and ρ_r is the ratio of the particle density to the fluid density. Initially, $\theta = 0$. The term $(U_z^2 + U_x^2)$ arises since the velocities are normalized by the initial particle velocity while the drag and lift coefficients are normalized by the instantaneous particle velocity. The gravity force is neglected in this formulation.

Our numerical results (KES) for the time-dependent lift coefficient of a spherical particle interacting with a single vortex tube depends on the offset distance d_{off} , the vortex core size σ , and Reynolds number Re and can be summarized as:

$$C_L(t) = A [C_L(t)]_b \exp\left(\frac{B d_{off}}{\sqrt{\sigma}}\right) f(Re, v_{max}) \quad \text{for } C\sqrt{\sigma} \leq d_{off} \leq D\sqrt{\sigma}, \quad (8)$$

where the following combinations of values apply:

A	B	C	D
1.15	0.3	$-\infty$	-0.7
1	0.1	-0.7	0
1	0	0	1
$e^{0.1}$	-0.1	1	1.7
$1.15 e^{0.3}$	0.3	1.7	∞

Also, $[C_L(t)]_b$ is the lift coefficient for the base case where $Re = 100$ and $d_{off} = 0$ with $v_{max} = v_{max,b}$, $f(Re, v_{max}) = (100/Re)^m v_{max}/v_{max,b}$, and the exponent m is given by

m	σ	t
0.375	1	$0 \leq t \leq 9$
0.45	1	$9 < t \leq 24$
0.44	$2 \leq \sigma \leq 4$	$0 \leq t \leq 9$
0.51	$2 \leq \sigma \leq 4$	$9 < t \leq 24$

The time-averaged drag coefficient of the sphere in the flow with a vortex tube differs by 0.01% to 5% (depending on the offset distance) from the time-averaged drag coefficient of the axisymmetric flow for $Re = 100$ and $v_{max} = 0.2$. (Refer to equation (19) in KES.) Therefore, the time-dependent drag coefficient in equations (7a) and (7b) is approximated by the time-dependent drag coefficient obtained from the axisymmetric flow generated by a spherical particle injected into a quiescent fluid. The spherical particle in this flow experiences the drag force and thus is retarded. This axisymmetric drag coefficient was computed as a function of time and instantaneous Reynolds number by using the code which has been developed for the time-dependent axisymmetric flow. The torque on the sphere is neglected since the magnitude of the moment coefficient is small and less than 8% of the lift coefficient magnitude (table 4 of KES).

Figure 16 shows two trajectories of the sphere during the dimensionless time period between 0 and 24 for initial particle Reynolds numbers 50 and 100 with density ratio 200 (which is the ratio, for example, of n-octane density to that of air under 10 atmospheres of pressure). The initial vortex size is three times the sphere radius, and the initial offset distance of the sphere is zero. The initial maximum induced velocity of the vortex tube is 0.2 normalized by the initial sphere velocity. The sphere initially moves upward due to the vortex upwash and then moves downward due to the vortex downwash. The maximum positive deflection for the case of $Re_o = 50$ is higher than that of $Re_o = 100$.

Figure 17 shows two trajectories of the sphere which are traced from the initial injection beyond the time period of figure 16 until particle Reynolds number reaches unity for

initial particle Reynolds numbers 50 and 100 with the same initial parameters as in figure 16. Since the final Reynolds number is small, these trajectories are approximately those corresponding to the whole particle motion until it stops relative to the fluid. A counter-clockwise rotating vortex tube produces not only upwash downstream of itself and downwash upstream of itself but it also causes a shear flow across the sphere when it passes the sphere. The combined effect of the downwash and the shear flow causes the magnitude of the maximum negative lift to be greater than the maximum positive lift magnitude. Therefore, the average lift coefficient averaged over the time span 24 (the interaction time with one vortex tube) is one order of magnitude less than the rms lift coefficient and negative due to the shear flow effect. This small negative value of the average lift coefficient becomes important when the sphere interacts with an array of many vortices. Thus, the sphere travels upward only for the short initial time period and then moves downward for the most of the time until it stops. The final deflection ratios defined by the ratio of the final position x_f to z_f of the sphere are 1/36 for the case of $Re_o = 100$ and 1/34 for the case of $Re_o = 50$. However, the final deflection for the case of $Re_o = 100$ is higher than that of $Re_o = 50$, because the sphere for the case of $Re_o = 100$ possesses higher initial momentum and it travels farther than that of $Re_o = 50$.

Figure 18 shows four trajectories of the sphere during the dimensionless time period between 0 and 24 for the density ratio 25, 50, 100, and 200 with Reynolds number 100 and the same parameters for σ , d_{off} , and v_{max} as in figure 16. A sphere with lower density ratio initially deflects more than a sphere with higher density ratio as shown in figure 19. Four trajectories of the sphere which are traced from the initial injection until particle Reynolds number reaches unity for the density ratio 25, 50, 100, and 200 with the same initial parameters as in figure 18. However, the final transverse displacement increases with density ratio because the sphere with higher density ratio possesses higher initial momentum and it travels farther than the sphere with lower density ratio.

The larger v_{max} causes the larger sphere deflection; however, the sphere deflection is

not linearly proportional to v_{max} due to the nonlinearity of the equations (7a) and (7b).

The results of figures 16 and 18 indicate that the sphere would experience slightly lower drag than that of a sphere subjected to an axisymmetric flow when it passes the first vortex tube. This lower drag is caused by the upward motion of the sphere due to the upwash of the approaching vortex tube, and thus the center of the vortex tube is located below the front stagnation point of the sphere. This causes lower dynamic pressure ahead of the front stagnation point. However, the sphere would experience higher drag eventually when it passes more than one vortex tube and travels downward. Due to the downward motion, the vortex tubes are located above the front stagnation point of the sphere, causing higher dynamic pressure ahead of the front stagnation point.

The original computations in KES and in section 3.3 were made for a nondimensional time duration of 24 and 24.5, respectively. However, the trajectory calculations presented in figures 17 and 19 use the basic information from those original computations to yield trajectory predictions for much longer periods.

4 Conclusions

In order to improve the understanding of the physics of interaction between a particle and eddies of comparable length scale in a carrier flow, the unsteady, three-dimensional, incompressible, viscous flow interactions between a pair of vortex tubes advected by a uniform free stream and a spherical particle suddenly placed and held fixed in space were investigated numerically for a range of particle Reynolds number $20 \leq Re \leq 100$.

When the top and bottom vortex tubes have positive and negative circulations, respectively, the magnitude of the induced velocity due to the vortex tubes is added to the base flow velocity along the stagnation streamline. This causes the pressure at the stagnation point and the shear stresses in the upper and lower left regions to be higher than those of the axisymmetric flow past a sphere, thus increasing the drag. On the other

hand, when the top and bottom vortex tubes have negative and positive circulations, respectively, the induced velocity due to the vortex tubes is subtracted from the base flow velocity along the stagnation streamline. This causes the pressure at the stagnation point and the shear stresses in the upper and lower left regions to be lower than those of the axisymmetric flow past a sphere, thus reducing the drag. The lift and moment are zero for this symmetric configuration.

The interactions between a sphere and like-rotating a pair of cylindrical vortex tubes initially located ten radii upstream from the center of the sphere were investigated. The lift and moment coefficients of the sphere interacting with a pair of vortex tubes as a function of time are nearly identical, respectively, to those of the sphere interacting with a single vortex tube if the separation distance between the tube centers is less than $2\sqrt{\sigma}$ vortex tube diameter for the lift coefficient and less than $\sqrt{\sigma}$ vortex tube diameter for the moment coefficient; here, v_{maxt} instead of v_{max} is used in the case of a pair of vortex tubes, where v_{max} is the maximum induced velocity due to one vortex without presence of the other and v_{maxt} is the total maximum induced velocity due to the pair of vortices. In particular, lift and moment coefficients are linearly proportional to the maximum induced velocity. The moment coefficient is negligible compared to the lift coefficient.

The two-dimensional trajectories of a spherical particle interacting with an array of vortices whose sizes are comparable to the sphere size have been examined. The time-dependent drag and lift forces (KES) for the case of a spherical particle interacting with a single vortex were used to calculate the two-dimensional trajectory of a moving spherical particle interacting with an array of vortex tubes of like rotation. The present results show that the shear flow across the sphere induced by a vortex tube is responsible for the net deflection of a sphere interacting with an array of vortex tubes. Thus, the sphere eventually deflects in the direction of increasing relative velocity. The deflection ratio (ratio of sphere final location in z and x directions) of the sphere increases with decreasing initial Reynolds number and with decreasing density ratio. However, the total deflection

increases with increasing the initial Reynolds number and the density ratio because higher momentum causes the sphere to travel farther.

A turbulent flow possesses a wide spectrum of eddy sizes. In order to enhance the understanding of particle motion in a turbulent flow, we are currently investigating the motion of a *freely moving* particle interacting with a large vortex tube whose size is of the order of an integral length scale, i.e. at the other end of the spectrum relative to the present case. Preliminary results of the large vortex study show that the lift force on the particle is much smaller than that due to the small vortices (in the present paper) with the same maximum induced velocity (Kim, Elghobashi & Sirignano (1996)). Our direct solution of the three-dimensional Navier-Stokes equations over a freely moving particle confirms that due mainly to the drag force, the particle travels in a curved trajectory that depends on the direction of vortex rotation and the Stokes number of the particle. This indicates that the mechanism of particle dispersion due to the interaction with small vortices is quite different from that due to the interaction with a large vortex.

Acknowledgement

This work has been supported by the Air Force Office of Scientific Research under grant No. F49620-93-1-0028 with Dr. Julian Tishkoff acting as the technical monitor. We would like to thank Mr. Lyle Wiedeman for his assistance in using a three-dimensional graphic package Application Visualization System (AVS). The support of the San Diego Supercomputer Center and the San Diego Supercomputer Center under a block grant of the Office of Academic Computing of UCI are gratefully appreciated.

5 References

- Anderson, D. A., Tannehill, J. C. & Pletcher, R. H. 1984 *Computational Fluid Mechanics and Heat Transfer*. Hemisphere Publishing.
- Clift, R., Grace, J. R. & Weber, M. E. 1978 *Bubbles, Drops, and Particles*. Academic Press, New York.
- Kim, I., Elghobashi S. & Sirignano, W. A. 1995 Unsteady flow interactions between an advected cylindrical vortex tube and a spherical particle. *J. Fluid Mech.* **288**, 123-155.
- Kim, I., Elghobashi S. & Sirignano, W. A. 1996 The motion of a spherical particle in unsteady flows at moderate Reynolds Numbers *34th AIAA Aerospace Sciences Meeting Preprint* 96-0081.
- Overman, E. A. & Zabusky, N. J. 1982 Evolution and merger of isolated vortex structures. *Phys. Fluids* **25**, 1297-1305.
- Patnaik, G. 1986 A numerical solution of droplet vaporization with convection. Ph.D. Dissertation, Carnegie-Mellon University.
- Patnaik, G., Sirignano, W. A., Dwyer, H. A. & Sanders, B. R. 1986 A numerical technique for the solution of a vaporizing fuel droplet. *Prog. Astro. Aero.* **105**, 253-266.
- Rangel, R. & Sirignano, W. A. 1989 The dynamics of vortex pairing and merging. *27th AIAA Aerospace Sciences Meeting Preprint* 89-0128.
- Spalart, P. R. 1982 Numerical simulation of separated flows. Ph. D. Thesis, Stanford University.
- Taneda, S. 1956 Experimental investigation of the wake behind a sphere at low Reynolds number. *J. Phys. Soc. Japan* **11** 1104-1108.

Vinokur, M 1983 On one-dimensional stretching functions for finite-difference calculations.
J. Comput. Phys. **50**, 215-234.

Zabusky, N. J., Hughes M. & Roberts K. V. 1979 Contour dynamics for the Euler equations in two dimensions. *J. Comp. Phys.* **30**, 96-106.

σ	$C_{L,max1}$	$C_{L,max2}$	$C_{L,rms}$	$C_{M,max}$	$C_{M,rms}$
4	0.111	-0.186	0.103	0.011	0.0051
3	0.111	-0.196	0.102	0.013	0.0053
2	0.108	-0.197	0.094	0.013	0.0053
1	0.088	-0.162	0.070	0.011	0.0043
0.5	0.058	-0.116	0.046	0.0065	0.0023
0.25	0.034	-0.070	0.027	0.0034	0.0012

Table 1. Maximum positive and negative lift coefficients, rms lift coefficient, maximum moment coefficient, and rms moment coefficient as a function of the size of vortex tube for $Re = 100$ and $d_{off} = 1.5$ with $v_{maxt} = 0.1$.

Figure Captions

Figure 1. Flow geometry and coordinates

Figure 2. Pseudo-streamlines (left column) and contour lines of y-component vorticity (right column) in the principal plane at (a) $t = 0$, (b) 3, (c) 6, (d) 9, (e) 12, and (f) 15 for $Re = 100$, $d_{off} = \pm 1.5$, $\sigma = 1$, and $v_{maxt} = 0.738$ with top-positive and bottom-negative circulations.

Figure 3. Drag coefficients of the sphere as a function of time and v_{maxt} for $Re = 100$, $d_{off} = \pm 1.5$, and $\sigma = 1$.
with top-positive and bottom-negative circulations.

Figure 4. Pseudo-streamlines (left column) and contour lines of y-component vorticity (right column) in the principal plane at (a) $t = 0$, (b) 3, (c) 6, (d) 9, (e) 12, and (f) 15 for $Re = 100$, $d_{off} = \pm 1.5$, $\sigma = 1$, and $v_{maxt} = 0.738$ with top-negative and bottom-positive circulations.

Figure 5. Drag coefficients of the sphere as a function of time and v_{maxt} for $Re = 100$, $d_{off} = \pm 1.5$, and $\sigma = 1$.
with top-negative and bottom-positive circulations.

Figure 6. Pseudo-streamlines (left column) and contour lines of y-component vorticity (right column) in the principal plane at (a) $t = 1$, (b) 6, (c) 10, (d) 15, (e) 21, and (f) 30 for $Re = 100$, $d_{off} = \pm 1.5$, $\sigma = 1$, and $v_{maxt} = 0.59$.

Figure 7. A view of three-dimensional contour surfaces of $\omega_y = 0.2$ at (a) $t = 6$ and (b) $t = 21$ for the flow depicted in figure 2

Figure 8. Lift coefficients of the sphere as a function of time and v_{maxt} for $Re = 100$, $d_{off} = \pm 1.5$, and $\sigma = 1$.

Figure 9. Moment coefficients of the sphere under the same conditions as figure 7.

Figure 10. Drag coefficients of the sphere under the same conditions as figure 7.

Figure 11. Rms lift coefficients of the sphere as a function of $|d_{off}|$
for $Re = 100$ and $\sigma = 4$.

Figure 12. Rms moment coefficients of the sphere as a function of $|d_{off}|$
for $Re = 100$ and $\sigma = 4$.

Figure 13. Rms lift coefficients of the sphere as a function of $|d_{off}|$
for $Re = 20$ and $\sigma = 4$.

Figure 14. Rms moment coefficients of the sphere as a function of $|d_{off}|$
for $Re = 20$ and $\sigma = 4$.

Figure 15. Initial flow geometry for a sphere injected into an array of
infinite number of vortex tubes.

Figure 16 Two trajectories of the sphere during the time period between 0 and 24
for initial Reynolds numbers 50 and 100 with density ratio 200.

Figure 17 Two trajectories of the sphere traced from the initial injection until
Reynolds number reaches unity for initial Reynolds numbers 50 and 100 with
with density ratio 200.

Figure 18 Four trajectories of the sphere during the time period between 0 and 24
for the density ratio 25, 50, 100, and 200 with initial Reynolds number 100.

Figure 19 Four trajectories of the sphere traced from the initial injection until
Reynolds number reaches unity for the density ratios 25, 50, 100, and 200
with initial Reynolds number 100.

Fig. 1

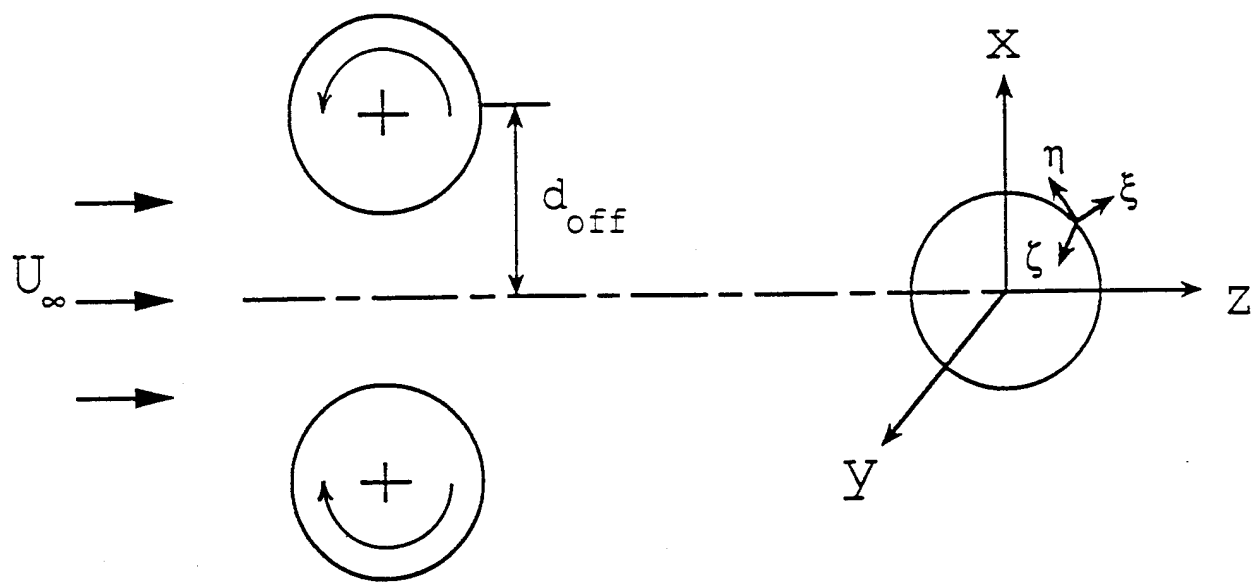
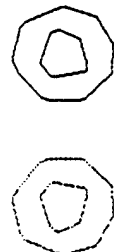
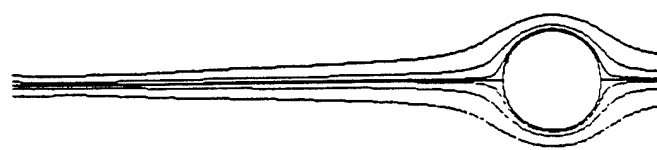
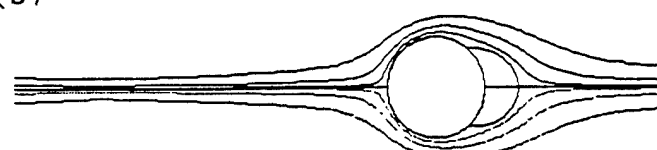


Fig. 2

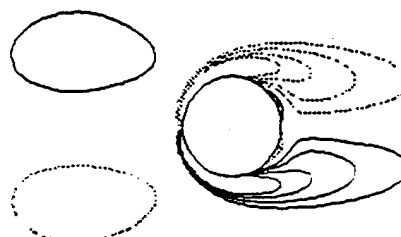
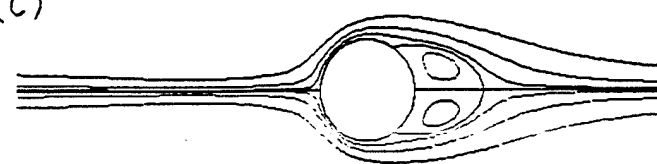
(a)



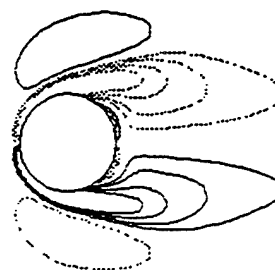
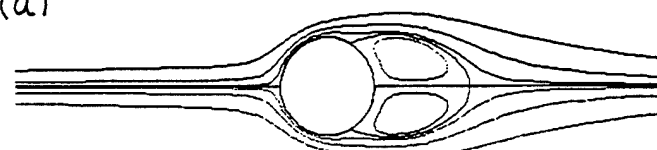
(b)



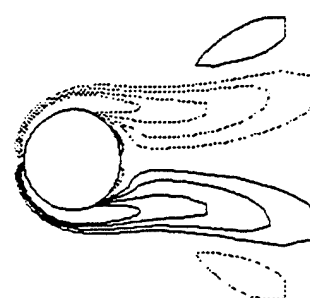
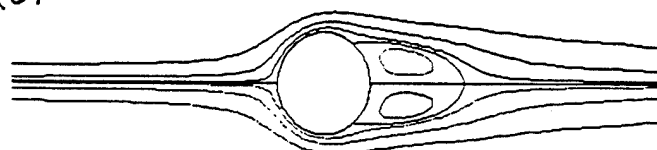
(c)



(d)



(e)



(f)

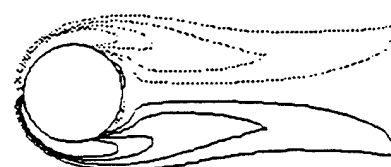
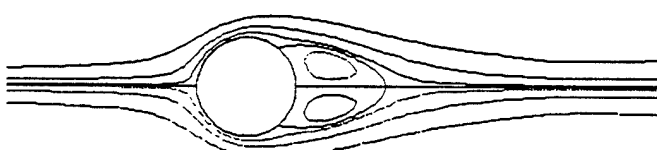


Fig. 3

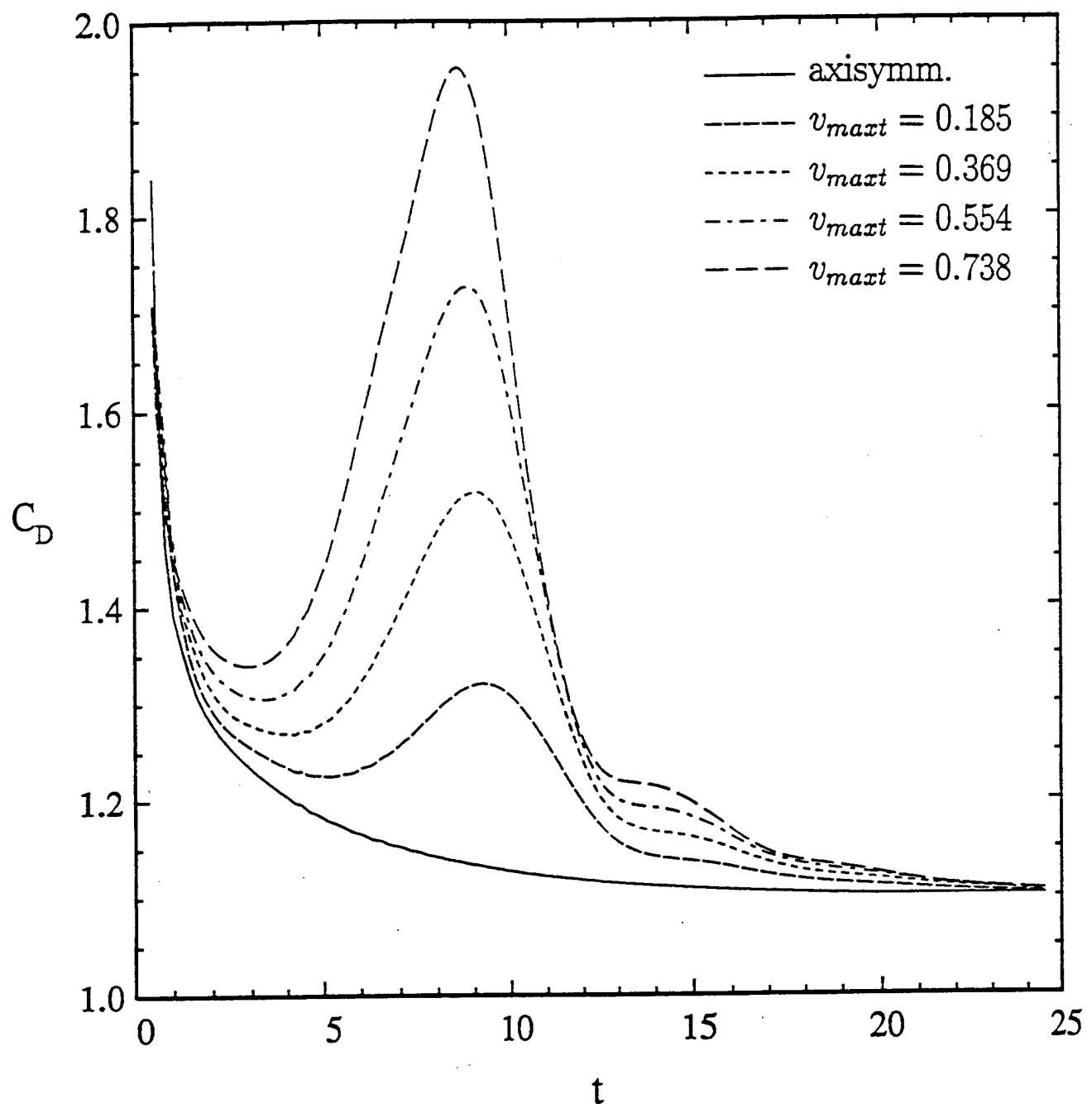
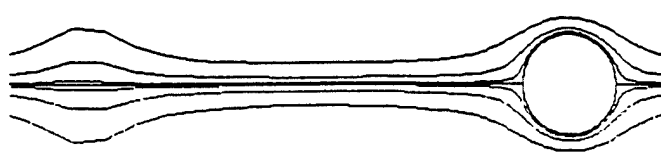
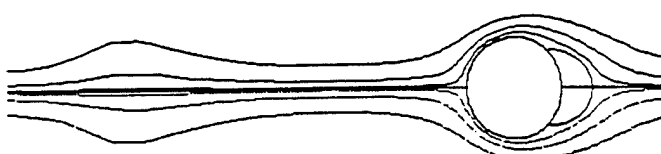


Fig. 4

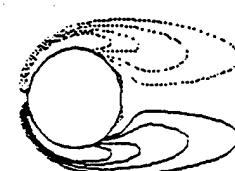
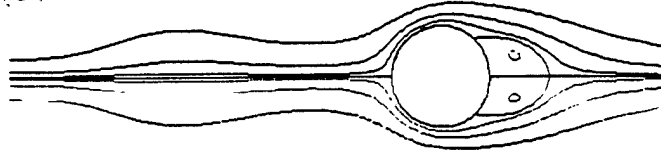
(a)



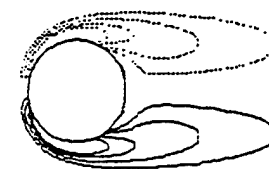
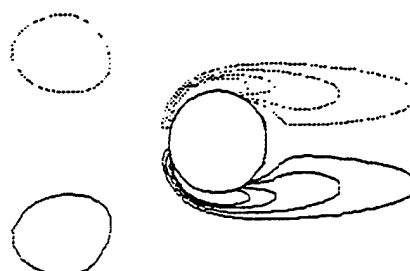
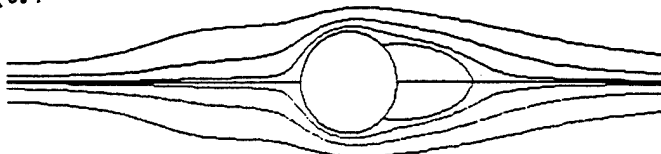
(b)



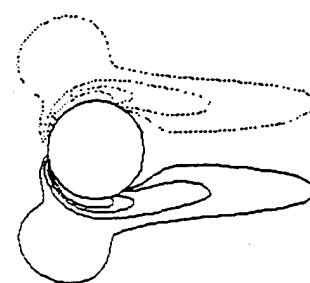
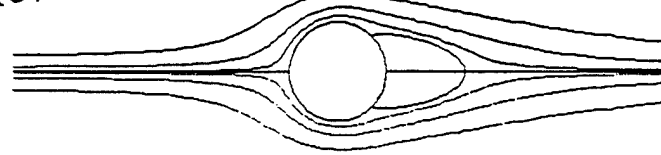
(c)



(d)



(e)



(f)

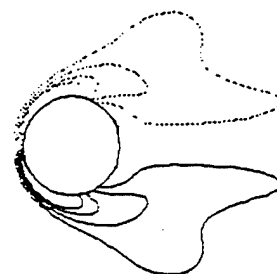
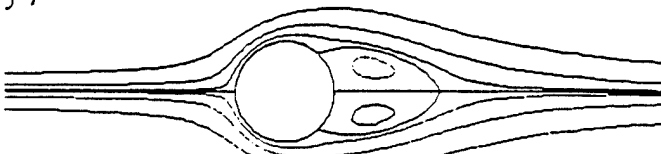


Fig. 5

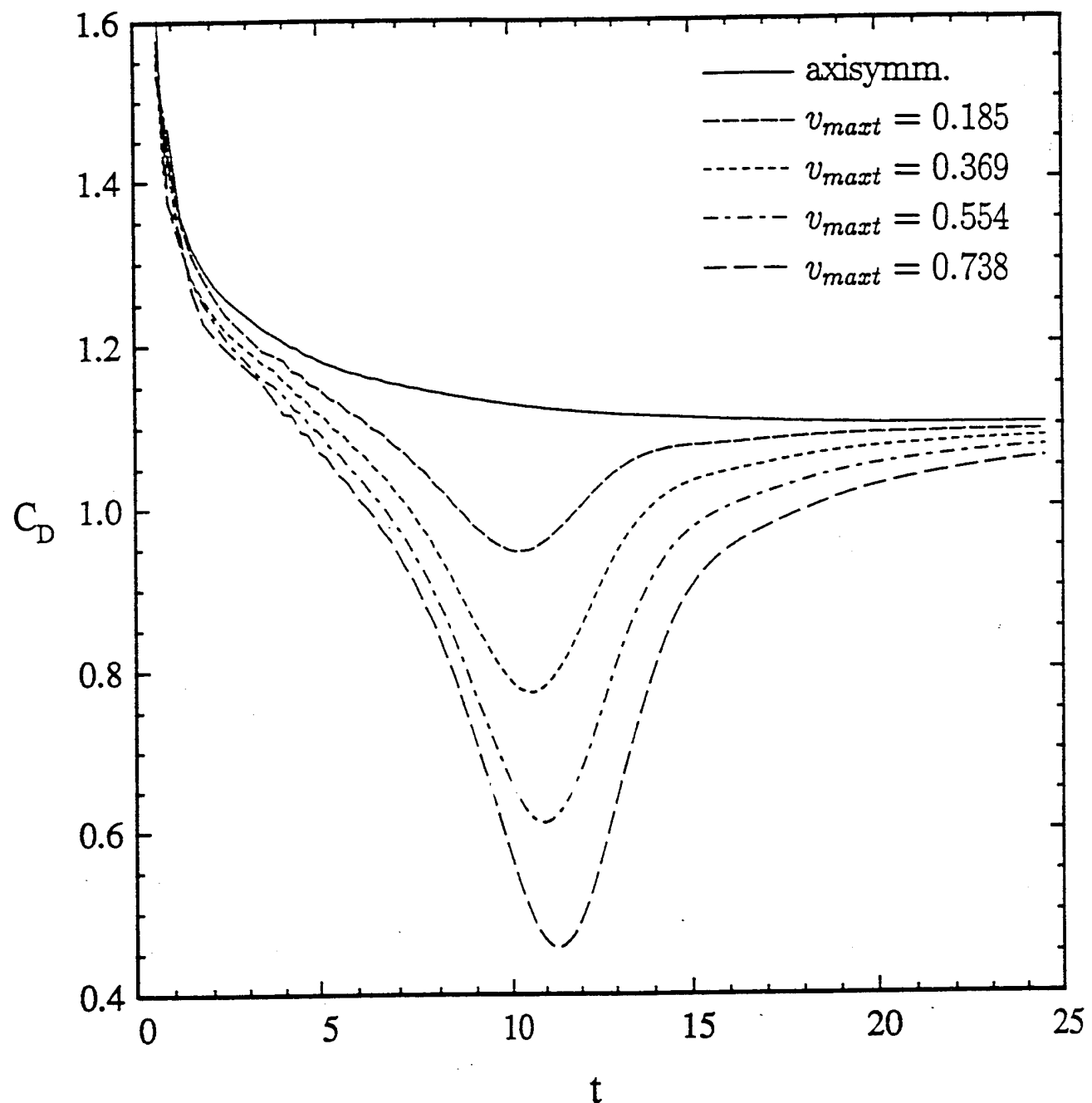


Fig 6

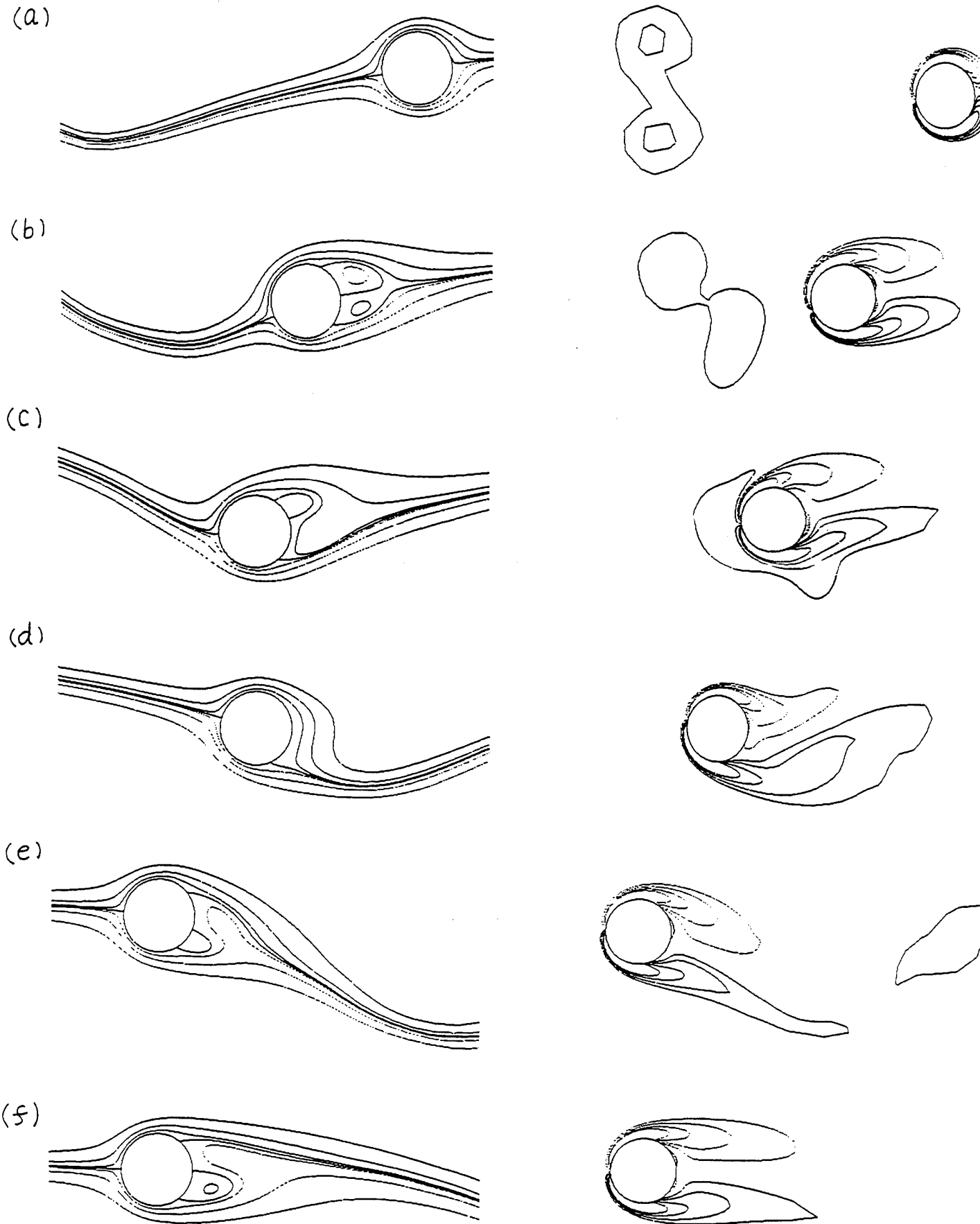


Fig. 7(a)

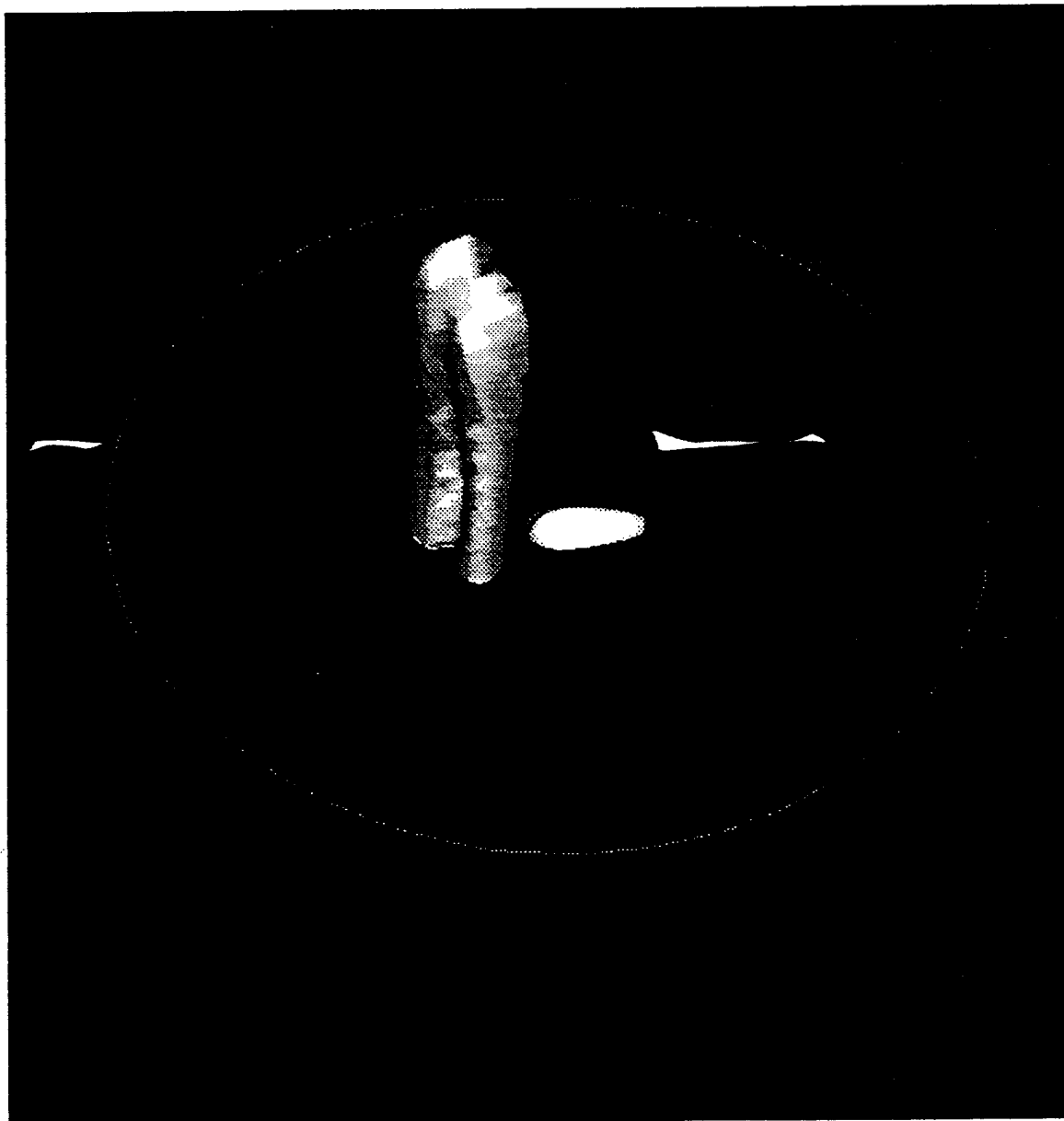


Fig. 7(b)

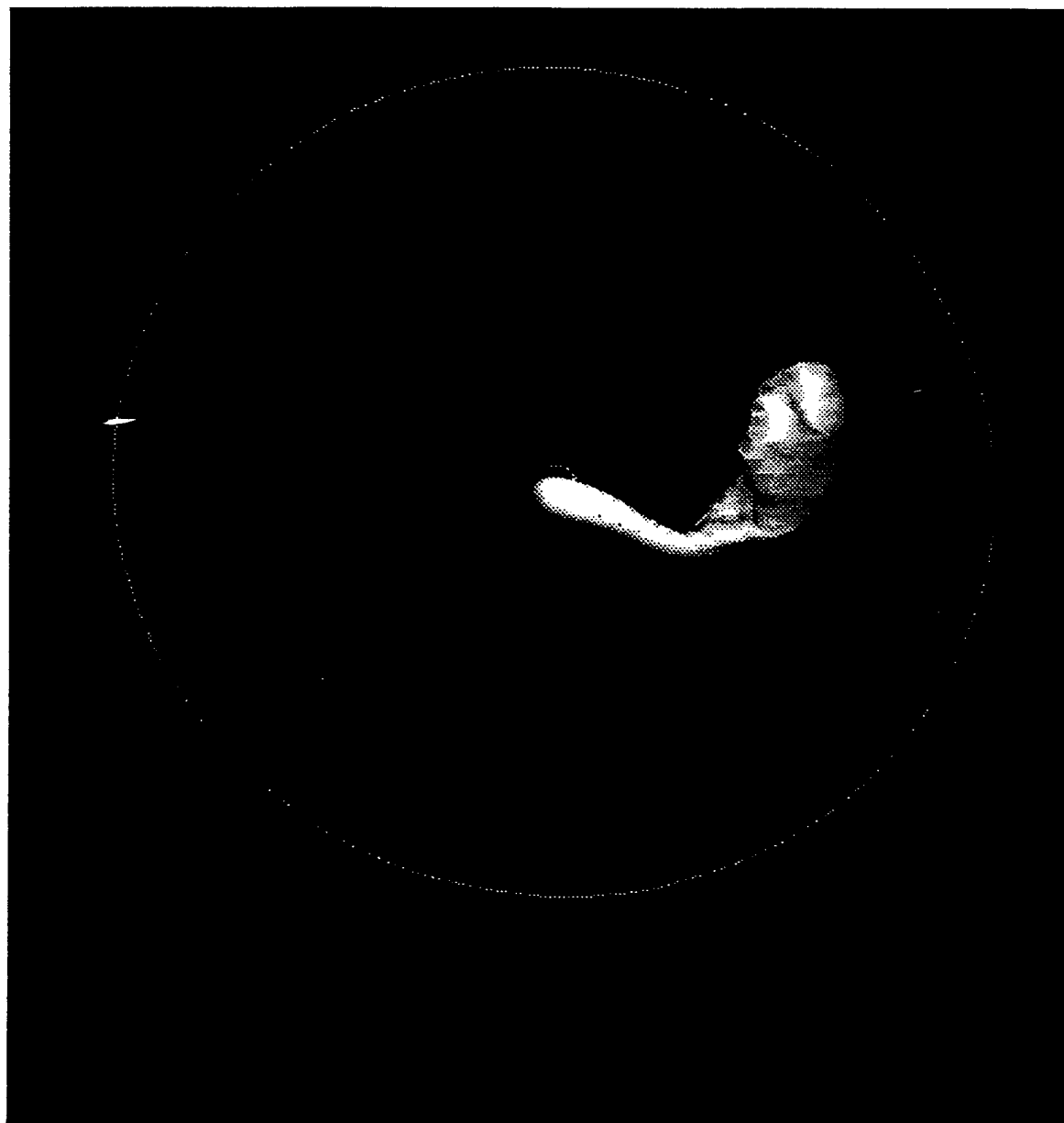


Fig. 8

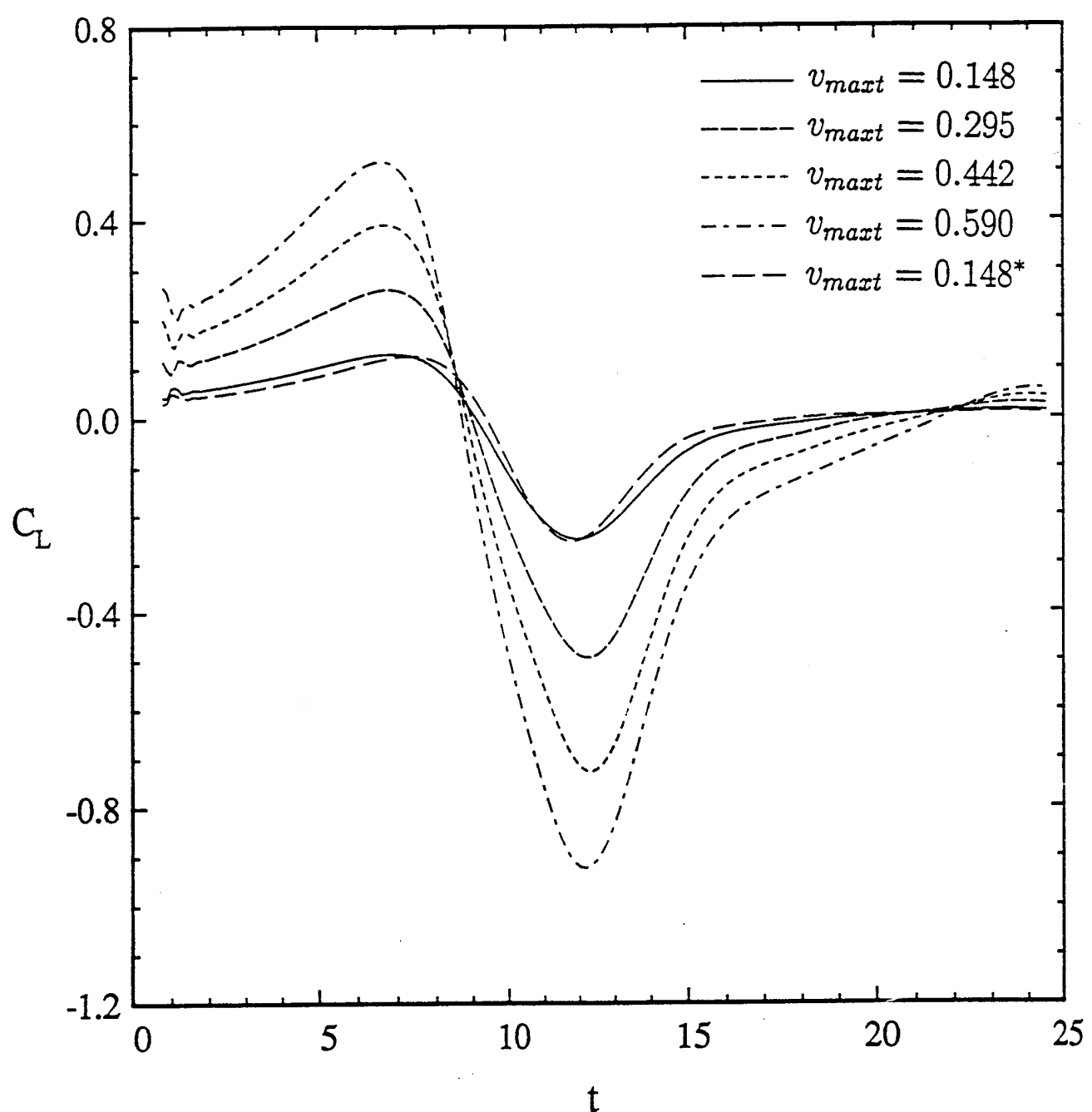


Fig. 9

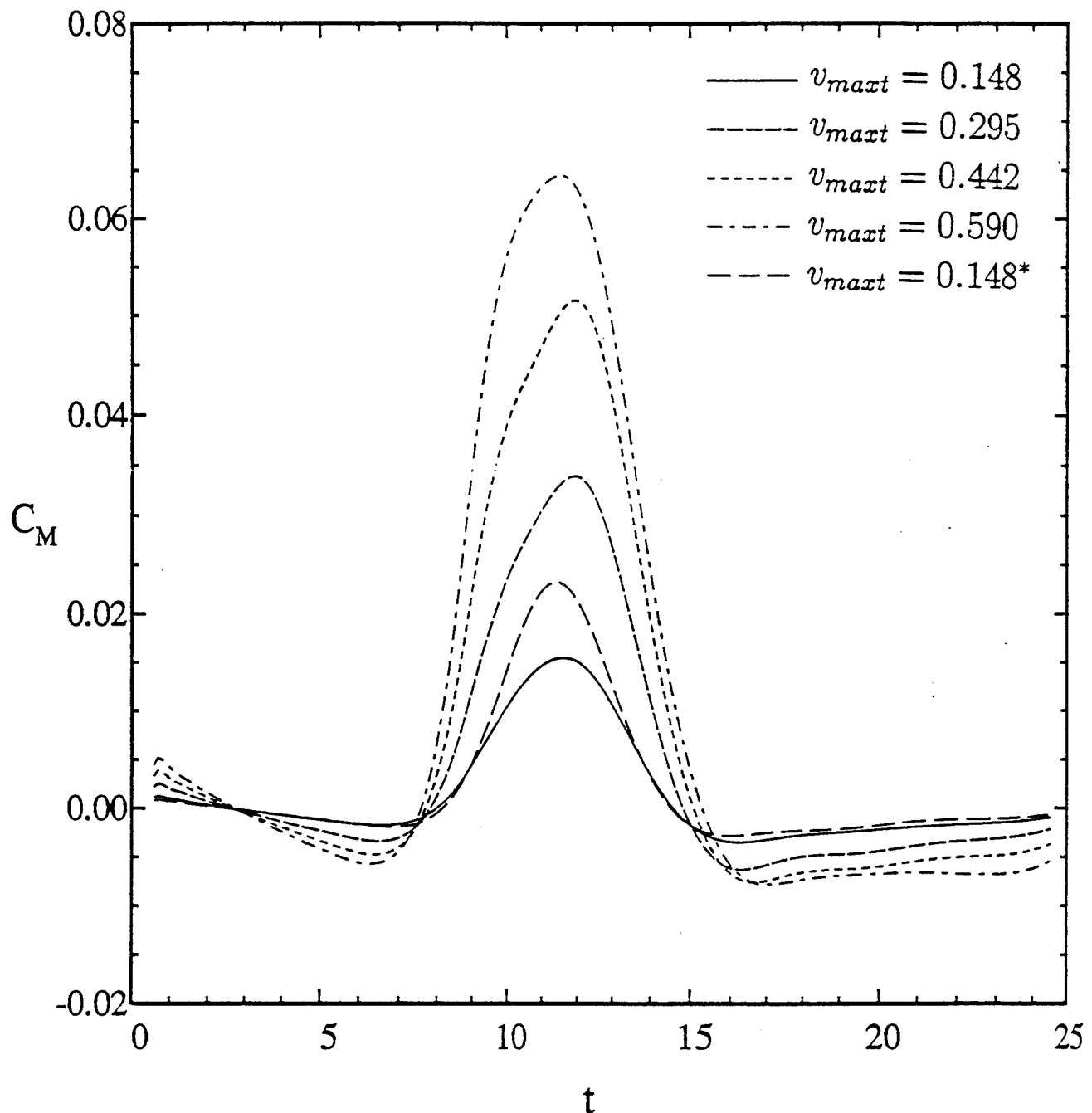


Fig. 10

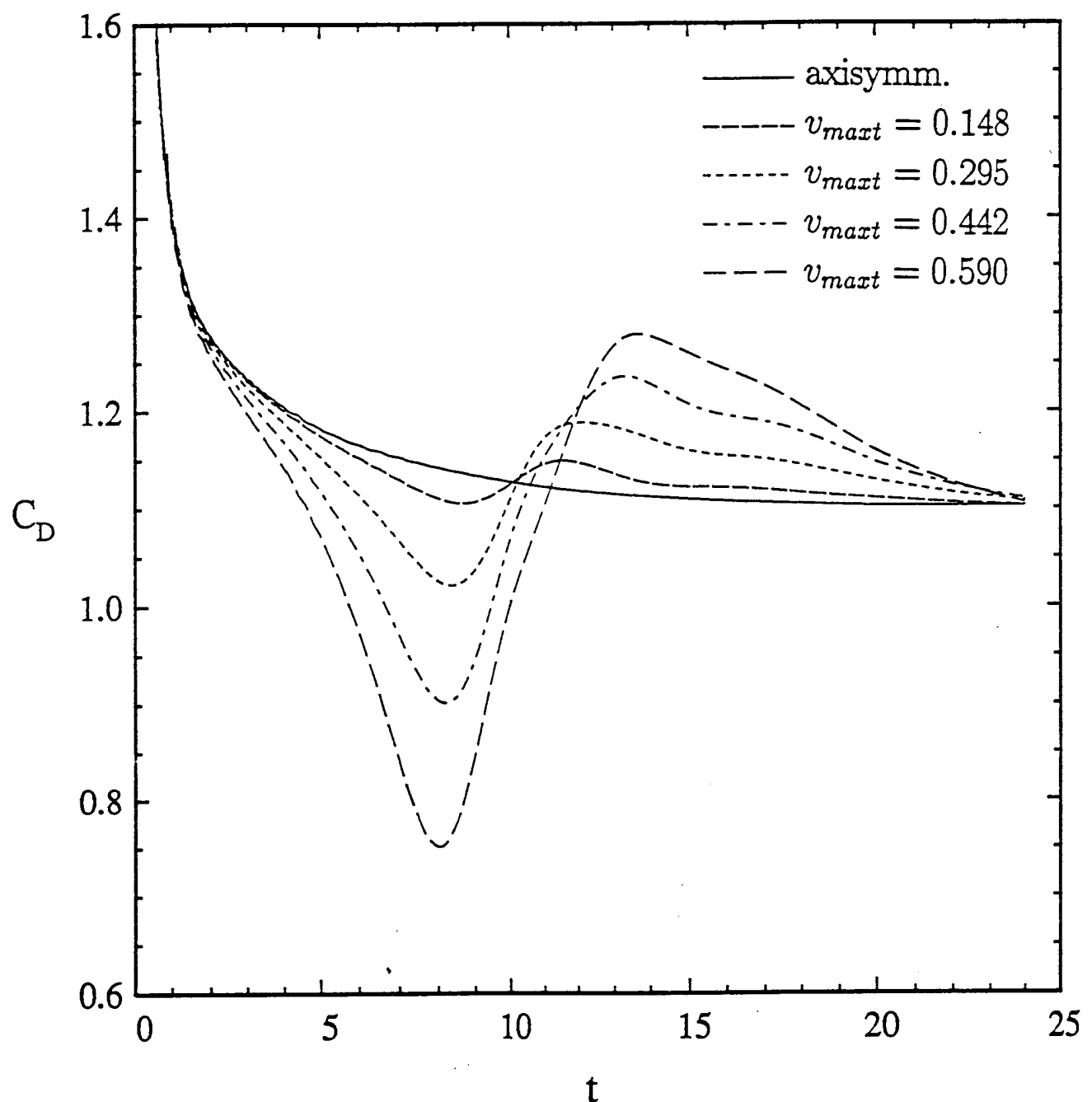


Fig. 11

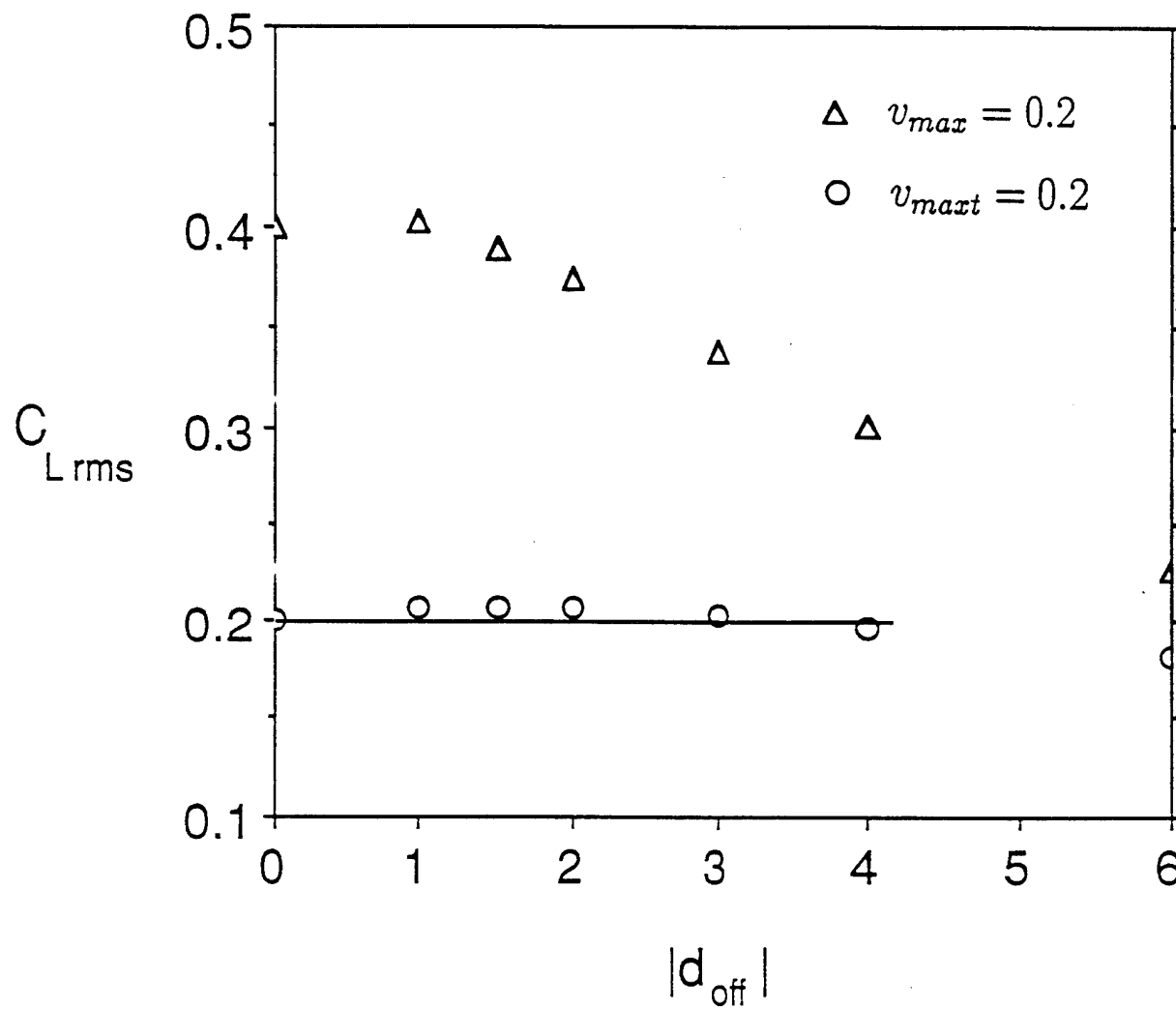


Fig. 12

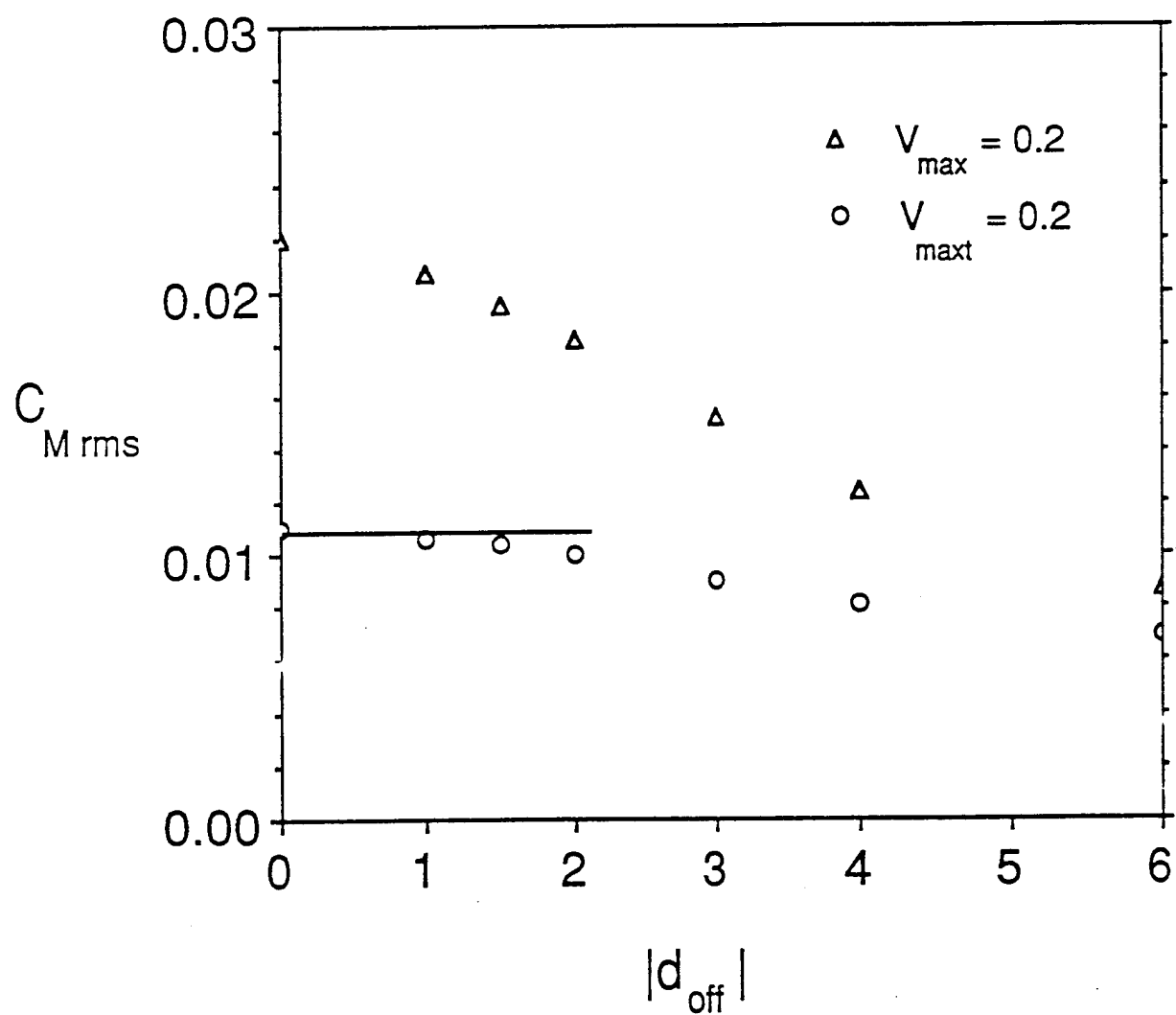


Fig. 13

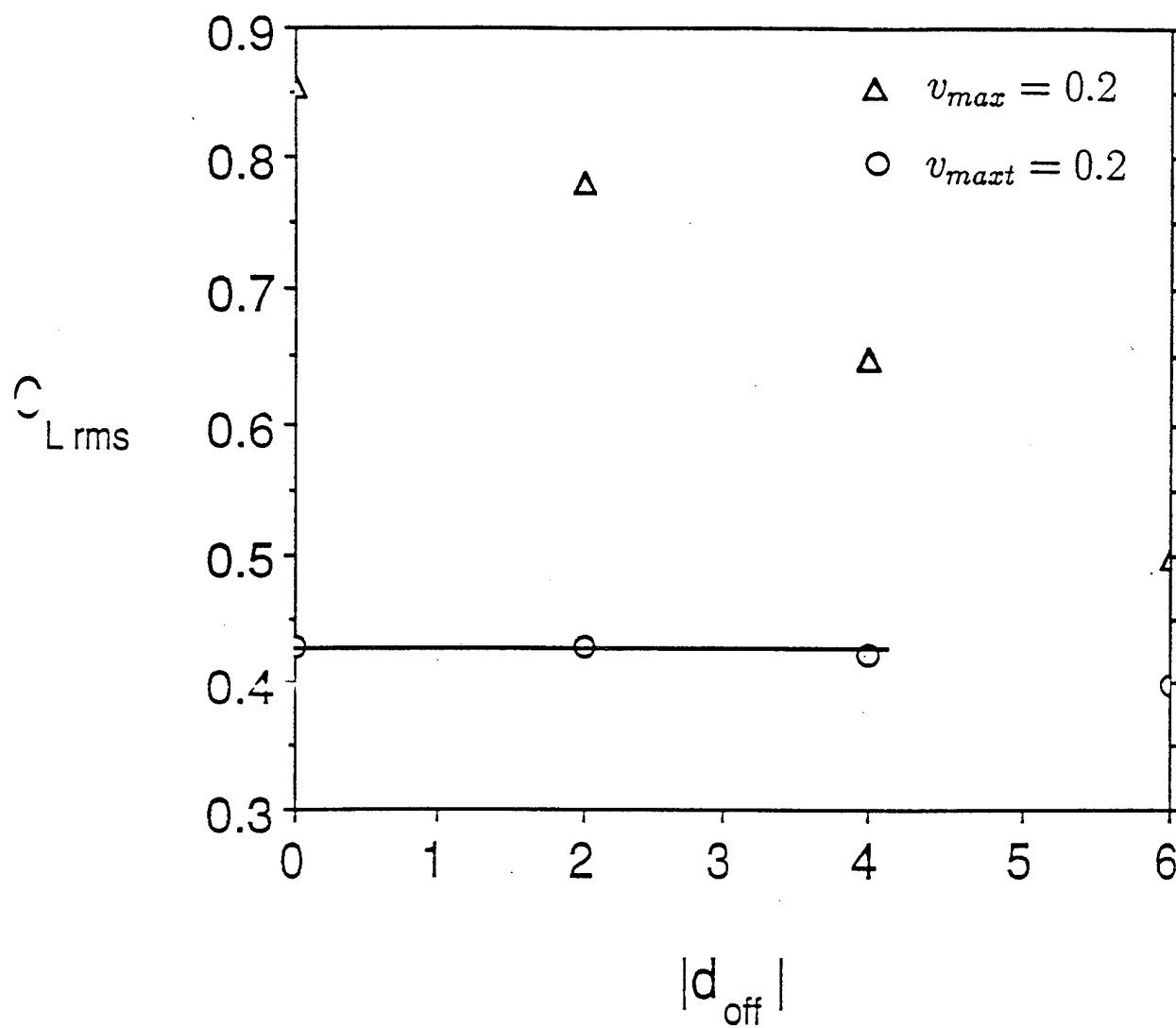


Fig. 14

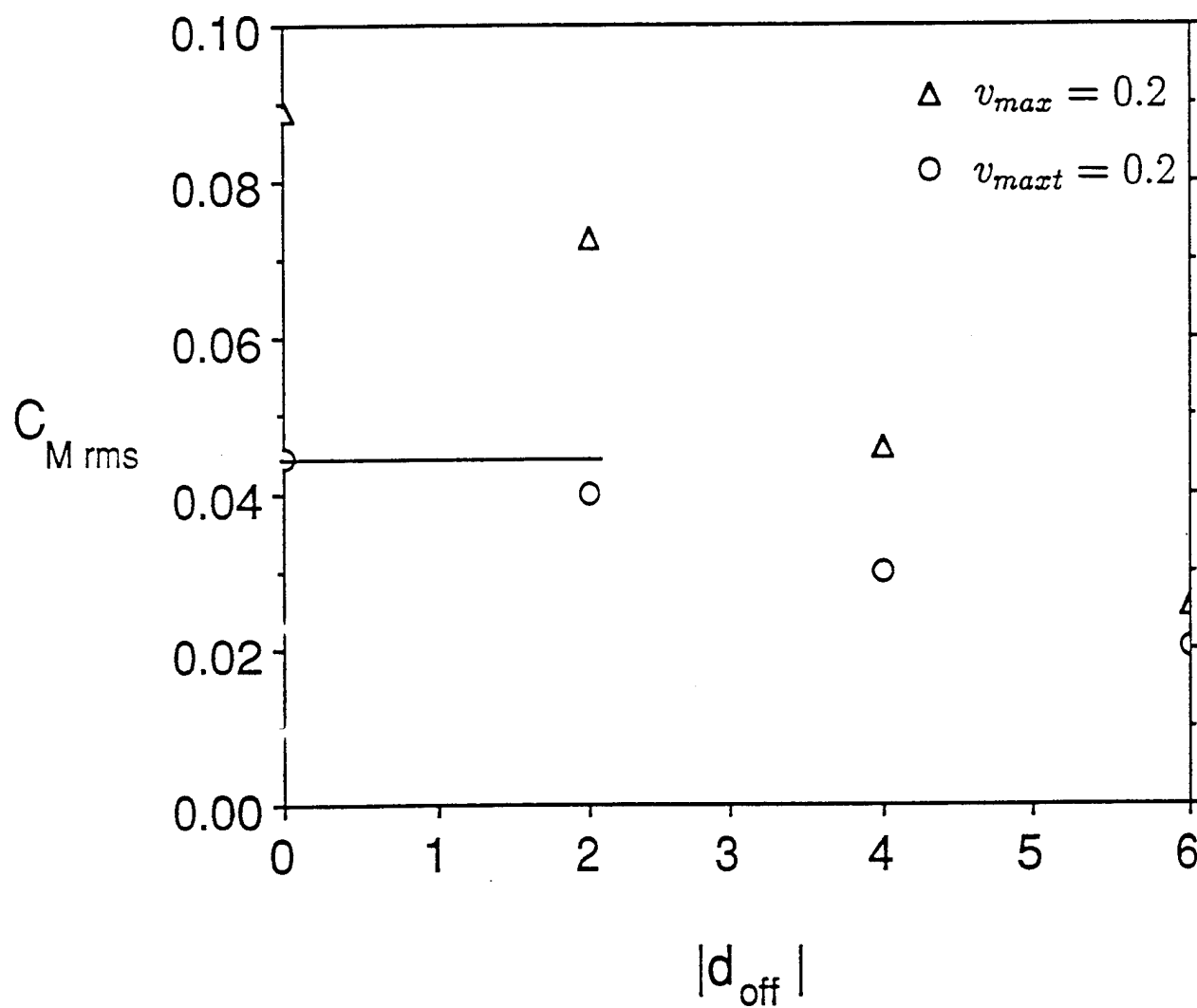


Fig 15

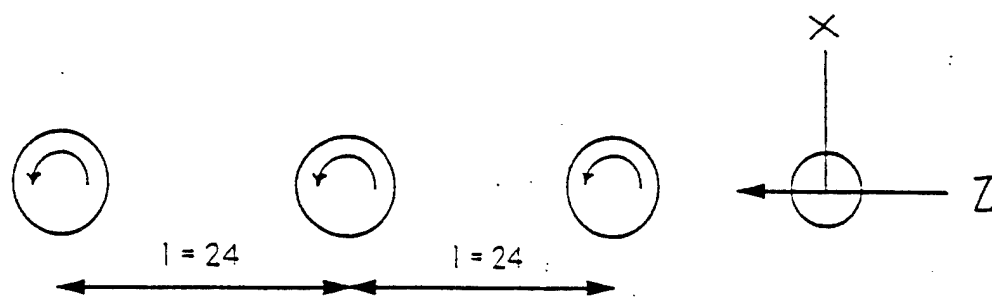


Fig 16

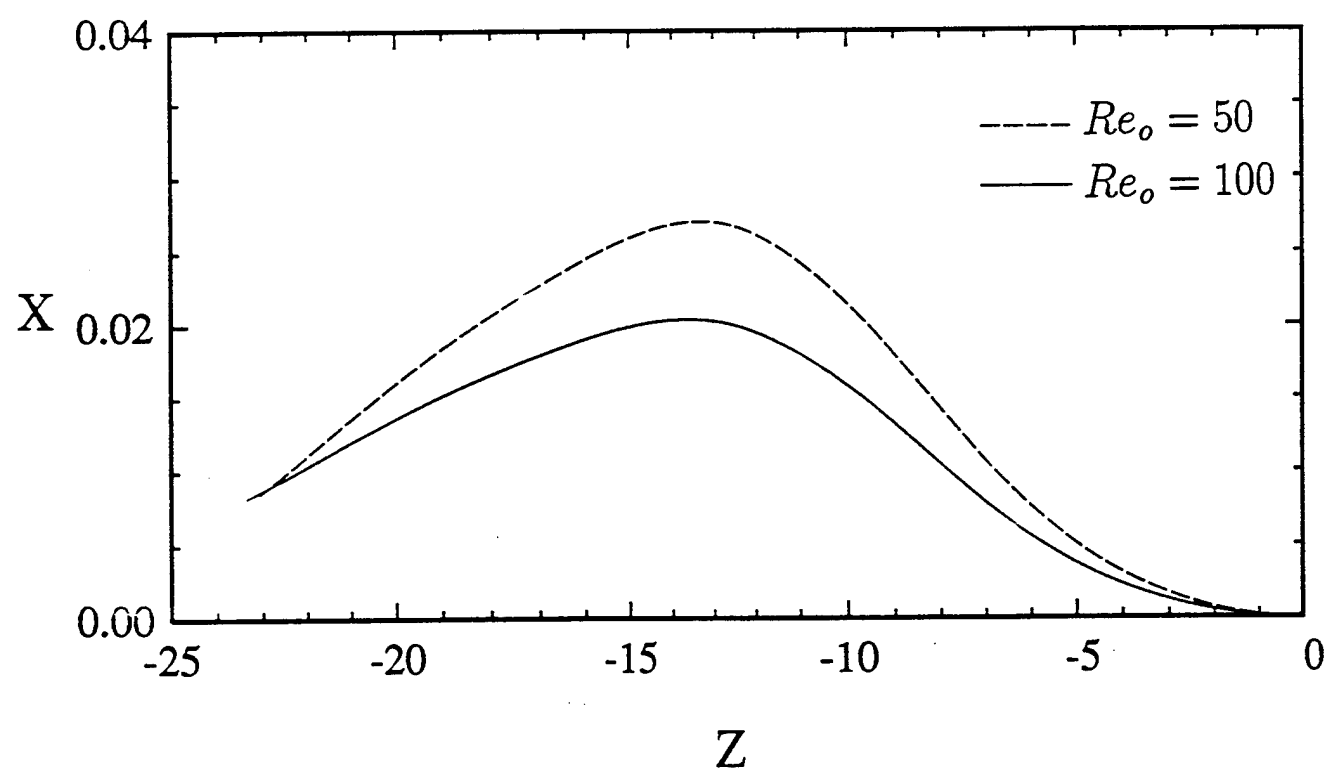


Fig 17.

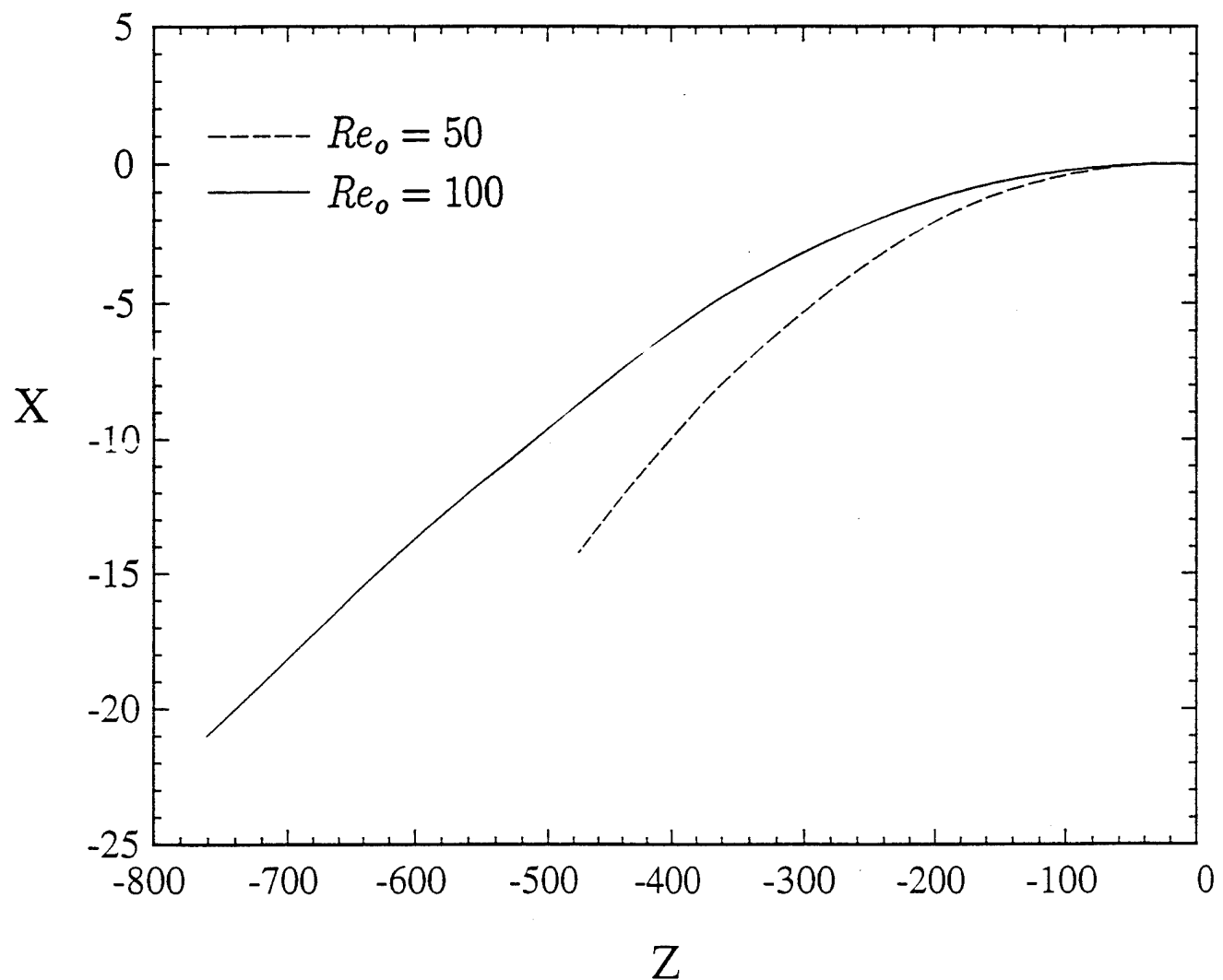


Fig 18

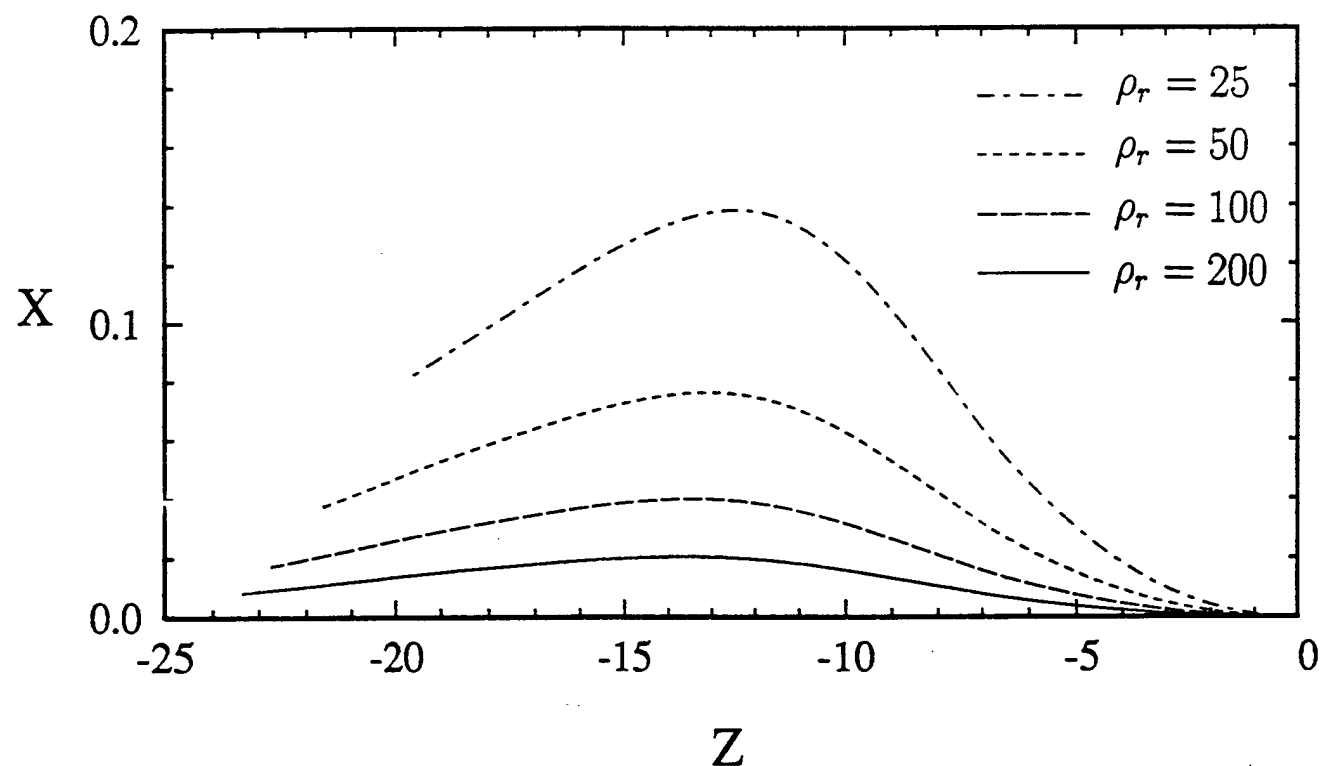
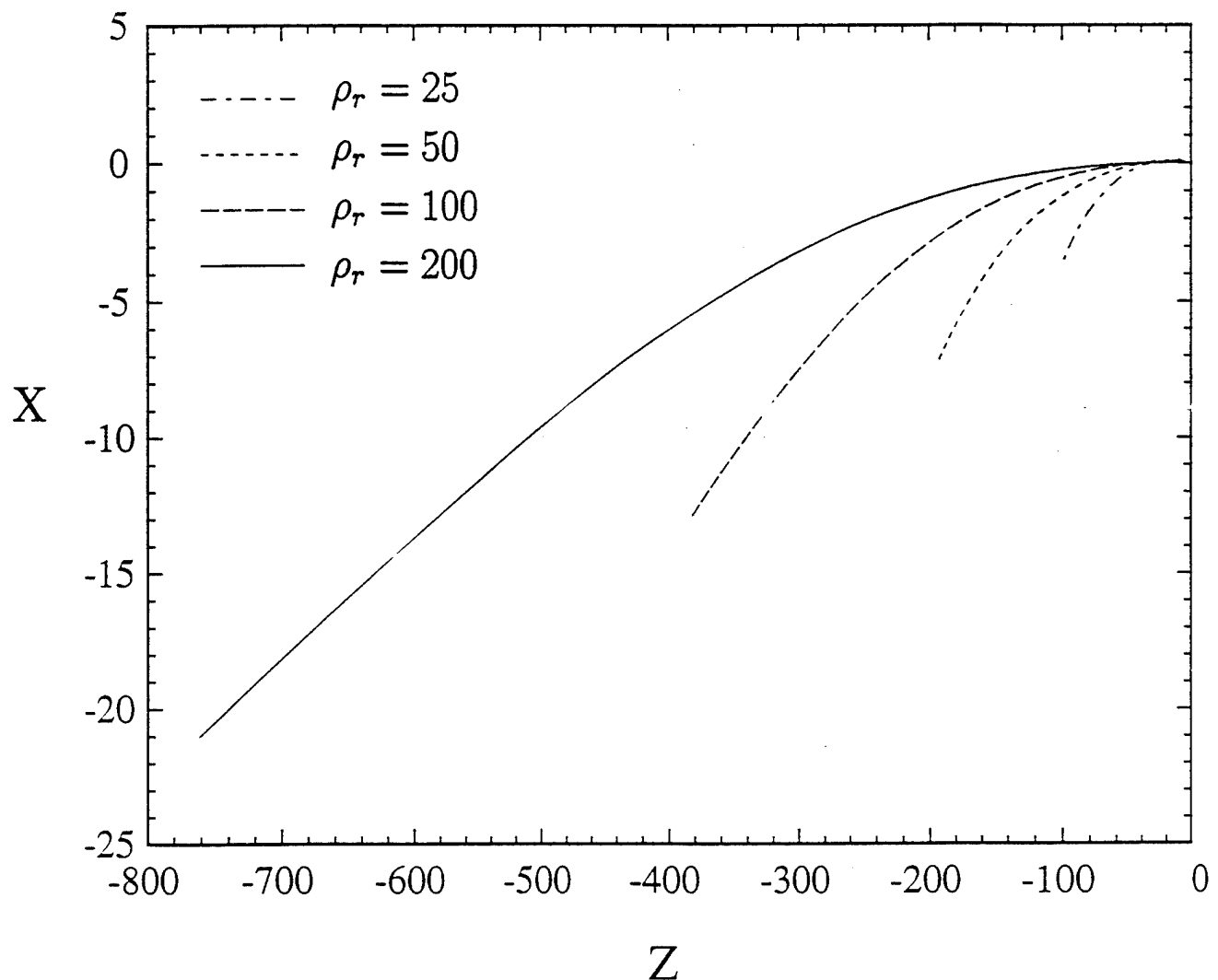


Fig 19





ADDENDUM TO SECTIONS 4 and 5

AIAA-96-0081

**The Motion of A Spherical Particle
in Unsteady Flows at Moderate
Reynolds Numbers**

I. Kim, S. Elghobashi, and W. A. Sirignano
University of California
Irvine, CA

**34th Aerospace Sciences
Meeting & Exhibit**

January 15-18, 1996 / Reno, NV

The Motion of A Spherical Particle in Unsteady Flows at Moderate Reynolds Numbers *

I. Kim[†], S. Elghobashi[‡] and W. A. Sirignano[§]

Department of Mechanical and Aerospace Engineering
University of California, Irvine

Abstract

The equations governing the motion of a spherical particle proposed by previous workers are examined and compared with the results of the numerical solution of the full Navier-Stokes equations for unsteady, axisymmetric flow around a *freely moving* sphere initially injected into an oscillating flow and for unsteady, three-dimensional flow around a *freely moving* sphere interacting with a large vortex tube. As a result, we propose a modified equation of the particle motion and demonstrate its superiority to the previously proposed equations for both rectilinear and two-dimensional motion over a wide range of Reynolds number and of density ratio.

Nomenclature

a	sphere radius
C_D	drag coefficient
C_L	lift coefficient
C_M	moment coefficient
\mathbf{g}	gravity vector
m_f	mass of the fluid displaced by the sphere
m_p	mass of the spherical particle
N_1, N_2, N_3	numbers of grids in ξ, η, ζ directions
Re	Reynolds number based on sphere diameter
\mathbf{u}	velocity vector of the fluid
\mathbf{v}	velocity vector of the sphere
u'_{max}	initial maximum induced velocity due to the vortex tube normalized by v_o
v_o	initial injection velocity of the sphere
t'	dimensionless time normalized by a/v_o
t^*	dimensionless time normalized by ω
X, Σ	inertial cylindrical coordinates
x, σ	noninertial cylindrical coordinates
X, Y, Z	inertial Cartesian coordinates
X'_o, Y'_o	initial particle position

*Copyright ©1996 by the authors. Published by the American Institute of Aeronautics and Astronautics, Inc. with permission.

[†]Research Associate, Member AIAA.

[‡]Professor of Mechanical and Aerospace Engineering,
member AIAA.

[§]Professor of Mechanical and Aerospace Engineering,
Fellow AIAA.

x, y, z normalized by the particle radius
noninertial Cartesian coordinates

Greek symbols

ρ_f	fluid density
ρ_p	particle density
μ_f	fluid viscosity
ν_f	fluid kinematic viscosity
ξ, η, ζ	nonorthogonal generalized coordinates
σ_o	initial radius of vortex core
w'	dimensionless frequency normalized by a/v_o

Superscript

' nondimensional quantity

Subscript

f	carrier fluid
o	initial quantity
p	spherical particle

1. Introduction

Accurate prediction of particle (or droplet) dispersion is important in many turbulent two-phase flows such as spray combustion and atmospheric dispersion of pollutants. Since a general analytical solution of the Navier-Stokes equations for a flow around a sphere is not possible, only a numerical solution of these equations can provide accurate information about the flow field. The forces on the particle can then be computed by integrating the normal and shear stresses around the particle, and then Newton's law is applied to obtain the acceleration of the particle. However, since these equations are unsteady and three-dimensional, they require excessive computing time. It is not possible to use this method to predict the simultaneous motion of many particles in a typical two-phase flow with the present and foreseeable computing capabilities.

The simplest method to describe the forces on a particle would be using the steady drag from the standard drag curve plus the net gravitational force on the particle according to

$$m_p \frac{dv}{dt} = \frac{1}{2} C_{D, std} \pi a^2 \rho_f |u - v| (u - v) + (m_p - m_f) g \quad (1)$$

where C_{Dstd} is the drag coefficient from the (steady) standard drag curve, \mathbf{u} is the carrier fluid velocity, \mathbf{v} is the sphere velocity, a is the sphere radius, and m_f is the mass of the fluid displaced by the sphere. Many application-oriented studies of dilute particle dispersion are based on Equation (1). In the case of unsteady flow, this relationship is an approximation that can be valid only if the response time of the particle is much larger than that of the flow.

Several equations accounting for the unsteadiness of the particle motion have been developed wherein a superposition of the steady drag and the unsteady (history) drag is used to obtain the forces on the particle. The available particle equations are reviewed next.

Basset¹, Boussinesq², and Oseen³ studied the unsteady rectilinear motion of a sphere in a stagnant incompressible, viscous fluid. They solved the Navier-Stokes equations for a *creeping* flow by neglecting the advective acceleration terms and derived the following expression for the acceleration of the sphere:

$$m_p \frac{dv}{dt} = -6\pi a \mu_f v - \frac{1}{2} m_f \frac{dv}{dt} + (m_p - m_f)g - 6a^2 \sqrt{\pi \mu_f \rho_f} \int_0^t \frac{dv/d\tau}{\sqrt{t-\tau}} d\tau \quad (2)$$

Maxey and Riley⁴ re-derived from first principles the following equation for the motion of a sphere in a *nonuniform creeping* flow:

$$m_p \frac{dv}{dt} = 6\pi a \mu_f (\mathbf{u} - \mathbf{v}) + \frac{1}{2} m_f \frac{d(\mathbf{u} - \mathbf{v})}{dt} + m_f \frac{Du}{dt} + 6a^2 \sqrt{\pi \mu_f \rho_f} \int_0^t \frac{d(\mathbf{u} - \mathbf{v})/d\tau}{\sqrt{t-\tau}} d\tau + (m_p - m_f)g, \quad (3)$$

where the Faxen forces are not shown here.

Based on the above two expressions (2) and (3), one may write an equation for the motion of a sphere for finite Reynolds number:

$$m_p \frac{dv}{dt} = \frac{1}{2} C_{Dstd} \pi a^2 \rho_f |\mathbf{u} - \mathbf{v}| (\mathbf{u} - \mathbf{v}) + \frac{1}{2} m_f \frac{d(\mathbf{u} - \mathbf{v})}{dt} + m_f \frac{Du}{dt} + (m_p - m_f)g + 6a^2 \sqrt{\pi \mu_f \rho_f} \int_0^t \frac{d(\mathbf{u} - \mathbf{v})/d\tau}{\sqrt{t-\tau}} d\tau, \quad (4)$$

where the first term is an empirical modification.

Odar and Hamilton⁵ and Odar⁶ experimentally examined the force on a guided sphere rectilinearly oscillating in an otherwise stagnant fluid for $0 \leq Re \leq 62$. They proposed an equation for the motion of a sphere in a flow of finite Reynolds number based on their experimental study as:

$$m_s \frac{dv}{dt} = -\frac{1}{2} C_{Dstd} \pi a^2 \rho_f |v| v - C_a \frac{1}{2} m_f \frac{dv}{dt} - C_h 6a^2 \sqrt{\pi \mu_f \rho_f} \int_0^t \frac{dv/d\tau}{\sqrt{t-\tau}} d\tau, \quad (5)$$

with C_a and C_h obtained experimentally and given by

$$\begin{aligned} C_a &= 2.1 - 0.132 M_{A1}^2 / (1 + 0.12 M_{A1}^2) \\ C_h &= 0.48 + 0.52 M_{A1}^3 / (1 + M_{A1})^3, \end{aligned}$$

where M_{A1} is the dimensionless acceleration defined by

$$M_{A1} = \frac{2a}{|\mathbf{u} - \mathbf{v}|^2} \left| \frac{d|\mathbf{u} - \mathbf{v}|}{dt} \right|.$$

Mei *et. al.*⁷ studied an unsteady flow over a *stationary* sphere with *small* fluctuations in the freestream velocity at finite Reynolds number ($0.1 \leq Re \leq 40$) using a finite difference method and found that the Basset-force term in the equation of particle motion should have a kernel which must decay much faster than $1/\sqrt{t-\tau}$ at large time. Mei and Adrian⁸ and Mei⁹ considered the same problem as Mei *et. al.*⁷ but for $St \ll Re \ll 1$ using a matched asymptotic expansion, where St is Strouhal number based on the angular frequency of the freestream and the sphere radius. They proposed a modified expression for the Basset-force term on the basis of the analytical result at small Reynolds number for low frequency, the numerical result at finite Reynolds number for low frequency, and the unsteady Stokes' result for high frequency. Their proposed equation is:

$$\begin{aligned} m_p \frac{dv}{dt} = & \frac{1}{2} C_{Dstd} \pi a^2 \rho_f |\mathbf{u} - \mathbf{v}| (\mathbf{u} - \mathbf{v}) + \\ & \frac{1}{2} m_f \left(\frac{Du}{Dt} - \frac{dv}{dt} \right) + m_f \frac{Du}{Dt} + \\ & 6\pi \mu_f a \int_{-\infty}^t K(t-\tau, \tau) \frac{d(\mathbf{u} - \mathbf{v})}{d\tau} d\tau + \\ & (m_p - m_f)g, \end{aligned} \quad (6a)$$

with the broad-frequency-range approximation for the integral kernel given by

$$K(t-\tau, \tau) = \left\{ \left[\frac{\pi(t-\tau)\nu_f}{a^2} \right]^{0.25} + \left[\frac{\pi |u(\tau) - v(\tau)|^3}{2 a \nu_f f_H^3(Re_t)} (t-\tau)^2 \right]^{0.5} \right\}^{-2} \quad (6b)$$

where $f_H(Re_t) = 0.75 + 0.105 Re_t(\tau)$; $Re_t = |u(\tau) - v(\tau)|/2a/\nu_f$.

Maxey¹⁰ included the effect of the initial velocity difference between the sphere and the carrier fluid in the particle motion equation of Maxey and Riley.⁴ The additional term is: $6a^2 \sqrt{\pi \mu_f \rho_f} (u(0) - v(0))/\sqrt{t}$.

In Section 2, the numerical solutions from the above equations will be compared with those from the full Navier-Stokes equations for unsteady, axisymmetric flow around a *freely moving* sphere initially injected into an oscillating fluid, and a new equation for arbitrary rectilinear particle motion is proposed. In Section

3, the numerical solutions from the above equations will be compared with those from the full Navier-Stokes equations for unsteady, *three-dimensional flow* around a *freely moving* sphere interacting with a large vortex tube, and a new equation for arbitrary two- and three-dimensional particle motion will be proposed. Section 4 provides a summary of the work. The gravity force is neglected in the computation in the following sections.

2. Unsteady, axisymmetric flow around a sphere injected into an oscillating fluid

2.1 Flow description

Consider an unsteady, axisymmetric, incompressible, laminar flow generated by a spherical particle injected into a constant property Newtonian fluid oscillating with time in the same direction as that of the particle motion as shown in Figure 1. The net gravity force acting on the particle is neglected. The origin of a non-rotating noninertial reference frame is chosen at the center of the particle.

Three coordinate systems are used in our formulation: the inertial (fixed in space) cylindrical coordinates (X, Σ) , the noninertial cylindrical coordinates (x, σ) , and the generalized coordinates (ξ, η) . The origin of the coordinates (x, σ) coincides with the sphere center. The coordinate ξ gives the radial and η gives the angular direction with respect to the sphere and are used for the numerical solution of the Navier-Stokes equations. The generalized coordinate system can be easily adapted to two-dimensional or axisymmetric arbitrary geometries.

The base flow in the far field oscillates with time in X-direction and is expressed as

$$\begin{aligned} u_x(t) &= \alpha_1 |v| \sin \omega t \\ u_\sigma(t) &= 0, \end{aligned}$$

where α_1 is a constant controlling the amplitude and ω is the angular frequency. The associated far pressure field can be obtained from the Navier-Stokes equations and is given as

$$p_b(x, t) = -\rho \alpha_1 \left(\frac{d|v|}{dt} \sin \omega t + |v| \omega \cos \omega t \right) X + p_{ref},$$

where p_{ref} is the reference pressure at $X = 0$. X is related to x as $X = x + X_p$, where X_p is the distance travelled by the particle and measured from the origin of the inertial coordinates (X, Σ) .

2.2 Governing equations and boundary conditions

The continuity and momentum equations to be solved are:

$$\nabla \cdot \mathbf{V} = 0 \quad (7)$$

$$\rho_f \left(\frac{d\mathbf{v}}{dt} + \frac{\partial \mathbf{V}}{\partial t} + \nabla \cdot \mathbf{V} \mathbf{V} \right) = -\nabla p + \mu \nabla^2 \mathbf{V}. \quad (8)$$

The governing equations (7) and (8) are nondimensionalized using the sphere radius a as the characteristic length and the initial injection velocity of the sphere v_o as the characteristic velocity. The nondimensionalized equations are cast in terms of the generalized coordinates (ξ, η) to treat an axisymmetric body of arbitrary shape. The numerical integration is performed using a cubic computational mesh with equal spacing ($\delta\xi = \delta\eta = 1$). In the present study, a spherical domain is used, and the grid reduces to an orthogonal, spherical grid. The grids are denser near the surface of the spherical particle, and the grid density in the radial direction is controlled by the stretching function developed by Vinokur.¹¹ The domain of the flow is bounded by $1 \leq \xi \leq N_1$, $1 \leq \eta \leq N_2$, where $\xi = 1$ and N_1 correspond, respectively, to the sphere surface and the farfield boundary surrounding the sphere; $\eta = 1$ and N_2 denote, respectively, the positive x-axis (downstream) and the negative x-axis (upstream).

The velocities on the sphere surface are zero due to the no-slip condition, and the pressure on the sphere is obtained from the momentum equation. The boundary conditions are

$$\frac{\partial p}{\partial n} = \mu \frac{\partial^2 V_n}{\partial n^2} - \rho_f \frac{dv_n}{dt}, \quad V_x = V_\sigma = 0 \text{ at } \xi = 1 \quad (9a)$$

$$p = p_b, \quad V_z = u_z - v, \quad V_\sigma = 0 \text{ at } \xi = N_1, \quad N_1 \leq \eta \leq N_2 \quad (9b)$$

$$p = p_b, \quad \frac{\partial V_x}{\partial x} = \frac{\partial V_\sigma}{\partial x} = 0 \text{ at } \xi = N_1, \quad 1 \leq \eta < N_{2m} \quad (9c)$$

$$\frac{\partial p}{\partial \eta} = \frac{\partial V_x}{\partial \eta} = 0, \quad V_\sigma = 0 \text{ at } \eta = 1 \text{ and } N_2 \quad (9d)$$

where V_x and V_σ are the fluid velocities with respect to the sphere in the x and σ directions, respectively, V_n is the fluid velocity with respect to the sphere in the direction normal to the sphere surface, and v_n is the sphere velocity in the direction normal to the sphere surface. n denotes the direction normal to the sphere surface, $\partial/\partial n = \sqrt{\xi_x^2 + \xi_\sigma^2} \partial/\partial \xi$, and $\eta = N_{2m}$ denotes the mid-plane between $\eta = 1$ and N_2 .

In order to start the numerical solution of equations (7) and (8), we provide initial velocity by superposing the initial velocities of the base flow and the sphere, and the no-slip condition on the sphere surface:

$$p_o = p_b, \quad V_{xo} = -v_o, \quad V_{\sigma o} = 0, \quad \text{except at } \xi = 1 \quad (10a)$$

$$p_o = p_b, \quad V_{xo} = V_{\sigma o} = 0 \quad \text{at } \xi = 1, \quad (10b)$$

2.3 Numerical solution

The three-dimensional algorithm to be used in predicting the unsteady, three-dimensional flow around a sphere interacting with a large vortex (Section 3) has been described in References 12 and 13. Here, an axisymmetric, implicit, finite-difference algorithm has been developed to solve simultaneously the set of the discretized partial differential equations. The method is based on an Alternating-Direction-Predictor-Corrector (ADPC) scheme to solve the time-dependent Navier-Stokes equations. ADPC is a slight variation of Alternating-Direction-Implicit (ADI) method and implemented easily when embedded in a large iteration scheme. The control volume formulation is used to develop the finite-difference equations from the governing equations with respect to the generalized coordinates (ξ, η) . An important part of solving the Navier-Stokes equations in primitive variables is the calculation of the pressure field. In the present work, a pressure correction equation is employed to satisfy indirectly the continuity equation. The pressure correction equation is of the Poisson type and is solved by the Successive-Over-Relaxation (SOR) method.

The overall solution procedure is based on a cyclic series of guess-and-correct operations. The velocity components are first calculated from the momentum equations using the ADPC method, where the pressure field at the previous time step is employed. This estimate improves as the overall iteration continues. The pressure correction is calculated from the pressure correction equation using the SOR method, and new estimates for pressure and velocities are obtained. This process continues until the solution converges at each time step.

We now test the accuracy of the solution procedure by predicting the axisymmetric flow over a solid sphere.

Here we examine the flow generated by an impulsively started solid sphere in a quiescent fluid at two Reynolds numbers: 20 and 100. The time-dependent solution converges asymptotically to a steady-state which is in good agreement with the available experimental data and correlations as shown in Table 1. Table 1 lists the drag coefficient as a function of the computational grid density at Reynolds numbers 20 and 100 respectively, and compares them with the correlations of Clift *et al.*¹⁴ Table 1 also shows the separation angle measured from the front stagnation point as a function of grid density at Reynolds number 20 and 100, in comparison with the data of Taneda¹⁵ and also with the correlations of Clift *et al.*¹⁴ The calculations were performed for four different grids, $(N_1 \times N_2) = (21 \times 21)$, (31×31) , (41×41) , and (51×51) in a computational domain with an outer boundary located at 21 sphere radii from the sphere center. The 51×51 grid is used in the following calculations.

We tested the solution procedure by varying the far-

field boundary condition and by changing the location of the outer boundary. In the first test, the far-field outflow boundary condition was changed from $\partial\phi/\partial x = 0$ ($\phi = V_x$ and V_θ) to $\partial\phi/\partial r = 0$. There was almost no difference in the drag coefficient and the near wake size (the separation angle and length of the recirculation eddy) at Reynolds numbers 20 and 100. Our calculation shows that separation does not occur at Reynolds number 20. In the second test, the location of the outer boundary in downstream was changed from 21 to 41 sphere radii. There was virtually no change in the drag coefficient and the near wake size at both Reynolds numbers.

2.4 Comparison of the solution of the previous equations with that of the Navier-Stokes equations

We now compare the numerical solutions from the equations introduced in Section 1 with those from the full Navier-Stokes equations for unsteady, axisymmetric flow around a *freely moving* sphere initially injected into a still fluid (the case of $\omega = 0$ in Section 2.1).

Figure 2 shows the drag coefficients of the sphere as a function of time ($0 \leq t' \leq 200$) with initial particle Reynolds number $Re_{t,0} = 150$ and the sphere/fluid density ratio $\rho_r = 5$. At $t' = 200$, the particle Reynolds number reduces to 4. The Basset history term in Equations (4) and (5) causes too low a value for the drag coefficient compared with the Navier-Stokes solution. The drag coefficient from Equation (6a) proposed by Mei and Adrian (1992) is the closest to that from the Navier-Stokes equations, but with increasing discrepancy as t' increases.

Figure 3 shows the drag coefficients of the sphere as a function of time ($0 \leq t' \leq 400$) with the same particle Reynolds number as in Figure 2 but with the density ratio $\rho_r = 200$. At $t' = 400$, the particle Reynolds number becomes 84. The Basset history term in Equations (4) and (5) still results in lower values for the drag coefficient. Now, the solution of Equation (6a) gives a good approximation to that of the Navier-Stokes equations. However, it is noted that the solution of Equation (1) also gives a good approximation and is very close to that of the Navier-Stokes equations. Thus, it is seen that for high density ratio (ρ_r) the deviation from the Navier-Stokes solution is reduced.

2.5 New improved equation for particle motion

We now investigate the restrictions imposed on the derivation of Equation (6a) proposed by Mei and Adrian⁸ and propose an improved equation for the particle motion.

Two restrictions were imposed on the derivation of Equation (6a). First, the integral kernel was developed under the assumption of small amplitude oscillation of the free stream. Secondly, the effect of the drag due

to the initial relative velocity between the particle and the carrier fluid was neglected.

As seen in the previous section, Equation (6a) produces a better solution for the drag of a sphere with higher density ratio than for the case with low density ratio; in other words, Equation (6a) produces a better solution for the drag of a sphere with lower deceleration than with higher deceleration.

The above analysis indicates the need for the sphere motion equation to account for the initial velocity difference and to have an integral kernel weighted by the acceleration magnitude. The weighting function contains the time derivative of the relative velocity M_{A1} and the ratio ϕ_r of M_{A2} to M_{A1} . M_{A1} was defined before in Equation (5) and M_{A2} and ϕ_r are defined by

$$M_{A2}(t) = \frac{(2a)^2}{|\mathbf{u} - \mathbf{v}|^3} \left| \frac{d^2|\mathbf{u} - \mathbf{v}|}{dt^2} \right|; \quad \phi_r(t) = \frac{M_{A2}}{M_{A1}}$$

These dimensionless groups can be introduced through dimensional analysis to obtain the forces on the particle of unsteady motion.

Now, we propose the following equation for particle motion.

$$\begin{aligned} m_p \frac{dv}{dt} &= \frac{1}{2} C_{Dstd} \pi a^2 \rho_f |\mathbf{u} - \mathbf{v}| (\mathbf{u} - \mathbf{v}) + \\ &\quad \frac{1}{2} m_f \left(\frac{Du}{Dt} - \frac{dv}{dt} \right) + m_f \frac{Du}{Dt} + \\ &\quad 6\pi\mu_f a \int_0^t K(t-\tau, \tau) \frac{d(\mathbf{u} - \mathbf{v})}{d\tau} d\tau + \\ &\quad 6\pi\mu_f a K_1(t) [\mathbf{u}(0) - \mathbf{v}(0)] + \\ &\quad (m_p - m_f)g \end{aligned} \quad (11a)$$

with the integral kernel $K(t - \tau, \tau)$ given by

$$K(t - \tau, \tau) = \left\{ \left[\frac{\pi(t - \tau)\nu_f}{a^2} \right]^{0.5/c_1} + G(\tau) \left[\frac{\pi}{2} \frac{|\mathbf{u}(\tau) - \mathbf{v}(\tau)|^3}{a\nu_f f_H^3(Re_t)} (t - \tau)^2 \right]^{1/c_1} \right\}^{-c_1} \quad (11b)$$

$$G(\tau) = \frac{1}{1 + \beta \sqrt{M_{A1}(\tau)}} \quad (11c)$$

$$\beta = \frac{c_2}{1 + \phi_r \phi_r^{c_4} / [c_3(\phi_r + \phi_r^{c_4})]} \quad (11d)$$

$$f_H = 0.75 + c_5 Re_t(\tau), \quad (11e)$$

and with the function $K_1(t)$ given by

$$K_1(t) = \left\{ \left[\frac{\pi t \nu_f}{a^2} \right]^{0.5/c_1} + G_1 \left[\frac{\pi}{2} \frac{|\mathbf{u}(0) - \mathbf{v}(0)|^3}{a\nu_f f_H^3(Re_{to})} t^2 \right]^{1/c_1} \right\}^{-c_1} \quad (11f)$$

$$G_1 = \frac{1}{1 + c_6 Re_{to}^{-0.25} (\rho_r + 0.5)^{-0.5}}, \quad (11g)$$

where $Re_t = |\mathbf{u}(\tau) - \mathbf{v}(\tau)|2a/\nu_f$ and $Re_{to} = |\mathbf{u}(0) - \mathbf{v}(0)|2a/\nu_f$.

The six constants c_i ($i = 1, \dots, 6$) in the above equations are determined by comparing the solutions from Equation (11a) with those from the Navier-Stokes equations and given for $0 \leq \omega' < \infty$ by

$$c_1 = 2.5, \quad c_5 = 0.126, \quad c_6 = 15,$$

$$c_2 = 45.5, \quad c_3 = 0.03, \quad c_4 = 0.1. \quad (11h)$$

For low frequencies $\omega' < 0.3$, the following values of c_2 , c_3 , and c_4 provide slightly better results than those of Equation (11h). The values of c_1 , c_5 , and c_6 are kept fixed as in (11h).

$$c_2 = 13.9, \quad c_3 = 0.12, \quad c_4 = 0.5. \quad (11i)$$

When $G(\tau)$ equals unity, the present integral kernel (Equation (11b)) is similar to Equation (6b) by Mei and Adrian,⁸ but the values of c_1 and c_5 in the present integral kernel are different from those used in Equation (6b). The values 2 and 0.105 in Equation (6b) corresponding to c_1 and c_5 were determined respectively by an interpolation and a curve fitting (Mei and Adrian⁸).

Equation (11c) shows that as M_{A1} is reduced, $G(\tau)$ approaches unity, and the present kernel (Equation (11b)) becomes similar in form to the kernel of Equation (6b). On the other hand, as M_{A1} becomes large, $G(\tau)$ approaches zero, and the present kernel becomes of the same form as that of Basset¹ (Equation (4)). The β in the expression of $G(\tau)$ is not a constant but a function of ϕ_r , the ratio of M_{A2} to M_{A1} . This function behaves as follows. $\beta \approx c_2(1 - \phi_r/c_3)$ for $\phi_r \ll 1$, and $\beta \approx c_2 c_3 / \phi_r^{c_4}$ for $\phi_r \gg 1$. Also, it can be shown that $G(\tau^*) \approx \omega'^{-0.4}$ as $\omega' \gg 1$ when τ is normalized by ω ($\tau^* = \tau\omega$).

G_1 (Equation (11g)) is obtained from $G(\tau = 0)$ (Equation (11c)) as follows. From the equation of particle motion Equation (11a), it can be shown that $dv/dt \approx kt^{-0.5}$ as $t \rightarrow 0$, where $k = (4.5/a) \sqrt{\nu_f/\pi} (\rho_r + 0.5)^{-1} (\mathbf{u}(0) - \mathbf{v}(0))$. Employing this form of dv/dt , the expressions of M_{A1} , M_{A2} , and ϕ_r as $t \rightarrow 0$ can be also derived. For example, ϕ_r is expressed by $\phi_r \approx at^{-1}/(\mathbf{u}(0) - \mathbf{v}(0))$. Finally, $G(\tau \rightarrow 0)$ is obtained as

$$G(\tau \rightarrow 0) \approx \frac{1}{1 + \alpha \tau^{c_4-0.25} Re_{to}^{-0.25} (\rho_r + 0.5)^{-0.5}}$$

where $\alpha = c_2 c_3 (9/\sqrt{\pi})^{0.5} (|\mathbf{u}(0) - \mathbf{v}(0)|/a)^{c_4-0.25}$. This equation shows that $G(0) = 0$ when $c_4 < 0.25$ but $G(0) = 1$ when $c_4 > 0.25$. However, the drag coefficient from the numerical computation of Equation (11a) with $G_1 = G(0) = 0$ or $G_1 = G(0) = 1$ is too high or low for some initial period compared with that from the Navier-Stokes equations. The drag coefficient from the numerical computation of Equation (11a) with $G_1 = G(\tau=0, c_4=0.25)$ is also too low for some initial period compared with that from the Navier-Stokes equations.

Therefore, G_1 was introduced as Equation (11g) by following the form of $G(\tau \rightarrow 0)$, and the coefficient c_6 in the expression of G_1 is determined by numerical optimization.

Figure 4 shows the drag coefficients of the sphere as a function of time for the same conditions as in Figure 2, but here the drag coefficients were computed from the new proposed equation (11a) and the previous equations including an initial velocity difference term. We note that the initial velocity difference terms are different among the equations because the integral kernels are different among the equations. The initial velocity difference term added to the BBO equation (Equation (4)) is the term given by Maxey¹⁰ and shown in Section 1. The initial velocity difference term added to Equation (6a) by Mei and Adrian⁸ is the term given by setting $G_1 = 1$ with $c_1 = 2$ and $c_5 = 0.105$ in Equations (11f) and (11e). It is shown in Figure 4 that the present equation of sphere motion gives the best solution.

Comparing Figures 2 and 4, we see that the initial velocity difference term with $t^{-0.5}$ improves Equation (4). However, the appropriate decay of this term is t^{-2} for finite initial particle Reynolds number (see Equation (11f)). However, it is interesting to note that the initial velocity difference term decays as $t^{-0.5}$ when $Re_{t_0} \rightarrow 0$ (see Equations (11g) and (11f)).

Figure 5 shows the drag coefficients of the sphere as a function of time ($0 \leq t' \leq 50$) for the same conditions as in Figure 4 except that $Re_{t_0} = 38$. At $t' = 50$, the particle Reynolds number becomes 2.18. It is shown that the new equation (11a) of sphere motion gives the best solution for low initial particle Reynolds number as well.

Figures 6 and 7 show the drag coefficients of the sphere as a function of time ($0 \leq t' \leq 200$) with $Re_{t_0} = 150$ and the density ratio $\rho_r = 5$. The base flows in Figures 6 and 7 oscillate with $\omega' = 0.4$ and $\alpha_1 = 0.02$, and $\omega' = 0.8$ and $\alpha_1 = 0.01$, respectively. Both figures show that Equation (6a) with an initial velocity difference term produces higher drag coefficients (except for some initial period) than do the Navier-Stokes equations. Again, the new equation (11a) produces very good agreement with the Navier-Stokes equations.

Figures 8 shows the drag coefficients of the sphere as a function of time ($0 \leq t' \leq 200$) with $Re_{t_0} = 150$ and the density ratio $\rho_r = 200$. The base flow oscillates with $\omega' = 0.1$ and $\alpha_1 = 0.18$. This figure shows that Equation (11a) produces slightly better drag coefficient than does Equation (6a) with an initial velocity difference term compared with the drag coefficient from the Navier-Stokes equations. The better performance of Equation (6a) for the case of higher density ratio is due to small dimensionless acceleration M_{A1} in the case of higher density ratio as shown in Figure 9, which shows M_{A1} as a function of time for the cases of $\rho_r = 5$ (with $\omega' = 0.1$ and $\alpha_1 = 0.06$) and $\rho_r = 200$

(Figure 8). When M_{A1} becomes small, the function $G(\tau)$ in Equation (11b) approaches unity, and thus the integral kernel of Equation (11a) approaches that of Equation (6a).

Figure 10 shows the drag coefficients of the sphere as a function of time ($0 \leq t' \leq 200$) for the same conditions as in Figure 8 except that the drag coefficients are obtained from different equations. Neglecting the history term and the other terms in Equation (11a) causes a phase-lag to the drag coefficient.

3. Unsteady, three-dimensional flow around a sphere interacting with a large vortex

3.1 Flow description

We consider the time-dependent, three-dimensional, incompressible, flow around a small spherical solid particle injected into a counter-clockwise rotating large vortex which is located at the origin of the coordinates (X, Y, Z) fixed in space as shown in Figure 11. The net gravity force acting on the particle is neglected. The origin of a nonrotating noninertial reference frame (x, y, z) is chosen at the center of the particle.

The initial velocity field induced by the vortex tube is analytically computed by considering the evolution of a point vortex and is given by

$$U_\phi = \frac{\Gamma}{2\pi R} [1 - \exp(-\frac{R^2}{4\nu_f(t + t_o)})] \quad (12a)$$

$$t_o = \frac{\sigma_o^2}{4\nu_f(1.12)^2}, \quad (12b)$$

where $R = \sqrt{X^2 + Y^2}$, $\phi = \arctan Y/X$, and t_o is a parameter defined by initial size of the vortex core (σ_o) and the fluid kinematic viscosity (ν_f).

The initial maximum induced velocity u_{maxo} due to the vortex tube occurs on the edge of the vortex core $R = \sigma_o$ at $t = 0$ and can be obtained from Equation (12a). The pressure field due to the vortex tube is also analytically computed by integrating the radial component of the momentum equation which is $\rho U_\phi^2/R = \partial p/\partial r$.

It is assumed that the vortex is so large that the flow field induced by the vortex is not affected by the moving sphere except locally in the region around the sphere. The boundary conditions of the flow field are obtained by superimposing the sphere velocity and the induced velocity due to the vortex tube at the computational outer boundary relative to the sphere, and the pressure field due to the vortex tube is also imposed at the computational outer boundary. Although the flow computation is three-dimensional, the particle path remains in the plane of symmetry ($X - Y$ plane). Therefore, the trajectory computation is made for the case of a freely moving particle in two-dimensions. After computing the forces on the sphere, the deceleration (or acceleration) of the sphere is obtained via Newton's

second law of motion, and then the new location of the sphere is obtained.

The rotation of the sphere due to the torque on the sphere is neglected because the torque is very small as will be shown in Section 3.2.

3.2 Equation for particle motion in vector form

Figure 12 shows the lift and moment coefficients of the sphere as a function of time ($0 \leq t' \leq 600$) computed by solving the Navier-Stokes equations for initial particle Reynolds number $Re_{t_0} = 108.2$ and particle position $(X'_0, Y'_0) = (250, 0)$ with density ratio $\rho_r = \rho_p/\rho_f = 200$. The vortex tube has initial core radius (σ'_0) equal to 200 and the maximum induced velocity due to the vortex (u'_{max}) equal to 2. It is found that the lift and moment coefficients are small ($|C_L| \leq 0.16$ and $|C_M| \leq 0.03$) compared with the drag coefficient, which is shown in Figure 13. The lift and moment coefficients are small because the strain rate of the flow across the sphere is small when the sphere size is much smaller than the vortex tube as in the flow considered here.

Since the lift and moment coefficients are small, we postulate that the force due to the history term is aligned with the direction of the relative velocity vector and propose the following equation for particle motion in vector form.

$$\begin{aligned} m_p \frac{dv}{dt} = & \frac{1}{2} C_{Dstd} \pi a^2 \rho_f |u - v| (u - v) + \\ & \frac{1}{2} m_f \left(\frac{Du}{Dt} - \frac{dv}{dt} \right) + m_f \frac{Du}{Dt} + \\ & 6\pi\mu_f a \frac{(u - v)}{|u - v|} \int_0^t K(t - \tau, \tau) \frac{d|u - v|}{d\tau} d\tau + \\ & 6\pi\mu_f a K_1(t) [u(0) - v(0)] + \\ & (m_p - m_f) g \end{aligned} \quad (13a)$$

with the integral kernel $K(t - \tau, \tau)$ given by

$$K(t - \tau, \tau) = \left\{ \left[\frac{\pi(t - \tau)\nu_f}{a^2} \right]^{0.5/c_1} + G(\tau) \left[\frac{\pi}{2} \frac{|u(\tau) - v(\tau)|^3}{a\nu_f f_H^3(Re_t)} (t - \tau)^2 \right]^{1/c_1} \right\}^{-c_1} \quad (13b)$$

and with the function $K_1(t)$ given by

$$K_1(t) = \left\{ \left[\frac{\pi t \nu_f}{a^2} \right]^{0.5/c_1} + G_1 \left[\frac{\pi}{2} \frac{|u(0) - v(0)|^3}{a\nu_f f_H^3(Re_{t_0})} t^2 \right]^{1/c_1} \right\}^{-c_1} \quad (13c)$$

where $Re_t = |u(\tau) - v(\tau)|2a/\nu_f$; $Re_{t_0} = |u(0) - v(0)|2a/\nu_f$ and $G(\tau)$, f_H , and G_1 are in the same form

as defined in Equations (11c), (11e), and (11g), respectively. For rectilinear motion, Equation (13a) reduces to Equation (11a).

The six constants c_i ($i = 1, 2, \dots, 6$) in the above equations are the same as those in Equations (11h) and (11i).

It should be noted that Equation (13a) does not include terms associated with the lift force in cases of a rotating particle or a particle in a strong shear flow.

Figure 13 shows the drag coefficients of the sphere as a function of time computed by solving the Navier-Stokes equations, Equation (13a), and Equation (1) for the same parameters as used in Figure 12. It is shown that the drag coefficient from Equation (1) is in phase-lag compared with that of the Navier-Stokes equations. Neglecting the history term and the other terms in Equation (1) causes a phase-lag on the drag coefficient.

Figure 14 shows the trajectory of the sphere in the $X - Y$ symmetry plane. The semi-circle in the figure is the initial vortex core. Equation (1) predicts higher Y-location of the sphere than do the Navier-Stokes equations. However, the deviation of the trajectory from Equation (1) is small compared with that from the Navier-Stokes equations because the dimensionless acceleration of the sphere is small ($M_{A1} \leq 0.0195$) due to the high density ratio and the low frequency of the large vortex tube.

4. Conclusion

An improved equation for rectilinear particle motion has been proposed which includes a modified history term and a drag force due to the initial velocity difference between the particle and the carrier flow.

An extension of the equation to a vector form for two- or three-dimensional motion has been also proposed; the first comparison for particle motion in two dimensions is favorable. More computations are underway to examine the equation in detail.

Acknowledgement

This work has been supported by the Air Force Office of Scientific Research under grant No. F49620-93-1-0028 with Dr. Julian Tishkoff acting as the technical monitor. The support of the San Diego Supercomputer Center directly and the San Diego Supercomputer Center under a block grant of the Office of Academic Computing of UCI are gratefully appreciated.

References

1. Basset, A.B. (1888) *A Treatise on Hydrodynamics*, vol 2, p. 285. Dover.
2. Boussinesq, J.V. (1885) Sur la resistance . . . d'une sphère solide. *C.R. des Seances de l'Academie* 100, 935.

3. Oseen, C.W. (1927) *Hydrodynamik*. Leipzig: Akademische Verlagsgesellschaft.
4. Maxey, M.R. and Riley, J.J. (1983) Equation of motion for a small rigid sphere in a nonuniform flow. *Phys. Fluids* **26**, 883-889.
5. Odar, F. and Hamilton W.S. (1964) Forces on a sphere accelerating in a viscous fluid. *J. Fluid Mech.* **18**, 302-314.
6. Odar, F. (1966) Verification of the proposed equation for calculation of the forces on a sphere accelerating in a viscous fluid. *J. Fluid Mech.* **25**, 591-592.
7. Mei, R., Lawrence, C.J. and Adrian, R.J. (1991) Unsteady drag on a sphere at finite Reynolds number with small fluctuations in the free-stream velocity. *J. Fluid Mech.* **233**, 613-631.
8. Mei, R. and Adrian, R.J. (1992) Flow past a sphere with an oscillation in the free-stream and unsteady drag at finite Reynolds number. *J. Fluid Mech.* **237**, 323-341.
9. Mei, R. (1994) Flow due to an oscillating sphere and an expression for unsteady drag on the sphere at finite Reynolds number. *J. Fluid Mech.* **270**, 133-174.
10. Maxey, M.R. (1993) The equation of motion for a small rigid sphere in a nonuniform or unsteady flow. ASME/FED, Gas-Solid Flows, Vol. 166, 57-62.
11. Vinokur, M (1983) On one-dimensional stretching functions for finite-difference calculations. *J. Comput. Phys.* **50**, 215-234.
12. Kim, I., Elghobashi S. & Sirignano, W. A. (1993) Three-dimensional flow over two spheres placed side by side. *J. Fluid Mech.* **246**, 465-488.
13. Kim, I., Elghobashi S. & Sirignano, W. A. (1995) Unsteady flow interactions between an advected cylindrical vortex tube and a spherical particle. *J. Fluid Mech.* **288**, 123-155.
14. Clift, R., Grace, J. R. & Weber, M. E. (1978) *Bubbles, Drops, and Particles*. Academic Press, New York.
15. Taneda, S. (1956) Experimental investigation of the wake behind a sphere at low Reynolds number. *J. Phys. Soc. Japan* **11** 1104-1108.

$N_1 \times N_2 \times N_3$	C_{DP}	C_{DV}	C_D	C_D^*	θ_s	θ_s^*
$Re = 20$						
21×21	1.087	1.789	2.876		166.3	
31×31	1.057	1.759	2.816		172.6	
41×41	1.042	1.733	2.775		180	
51×51	1.038	1.725	2.763	2.74	180	180
$Re = 100$						
21×21	0.558	0.590	1.148		124.1	
31×31	0.533	0.581	1.114		125.6	
41×41	0.524	0.580	1.104		126.2	
51×51	0.521	0.580	1.101	1.09	126.4	126.5

Table 1. Drag coefficient and separation angle as a function of grid density at $Re = 20$ and 100, where * denotes the data from the correlation of Clift *et al* [12] and Taneda [13].

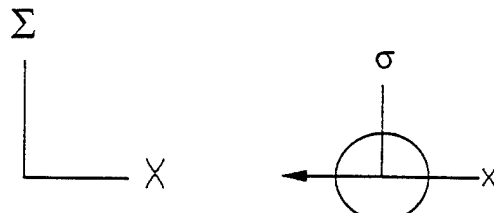


Figure 1. Flow geometry and coordinates

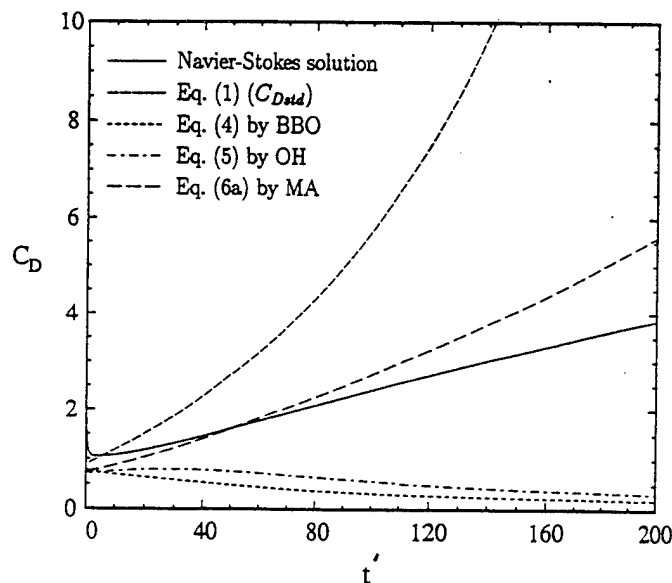


Figure 2. Drag coefficients as a function of time obtained from various equations for $Re_{t0} = 150$ with $\rho_r = 5$.

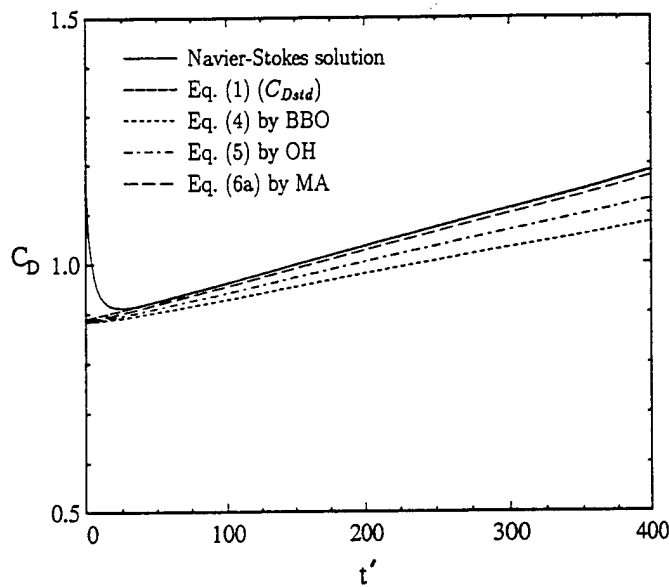


Figure 3. Drag coefficients as a function of time obtained from various equations for $Re_{t_0} = 150$ with $\rho_r = 200$.

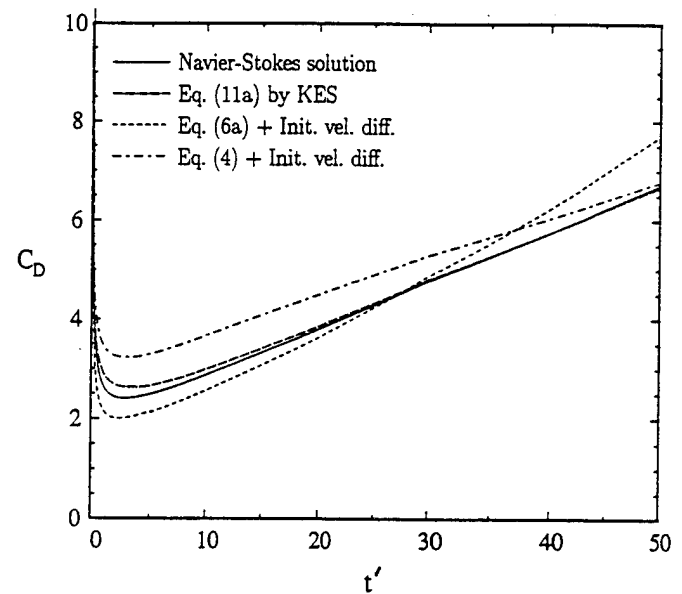


Figure 5. Drag coefficients as a function of time obtained from various equations for $Re_{t_0} = 38$ with $\rho_r = 5$.

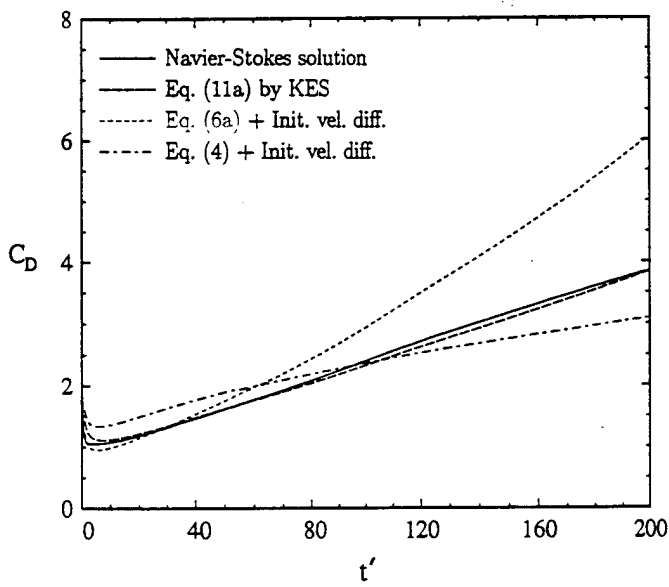


Figure 4. Drag coefficients as a function of time obtained from various equations for $Re_{t_0} = 150$ with $\rho_r = 5$.

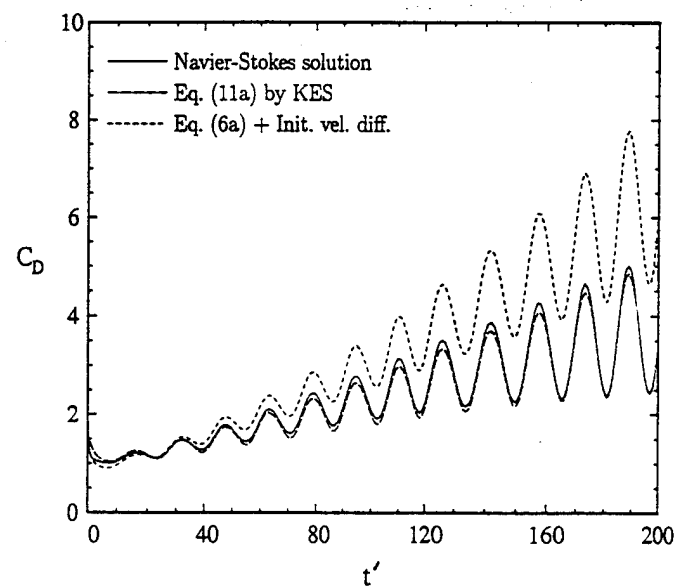


Figure 6. Drag coefficients as a function of time for $Re_{t_0} = 150$ and $\omega' = 0.4$ with $\rho_r = 5$.

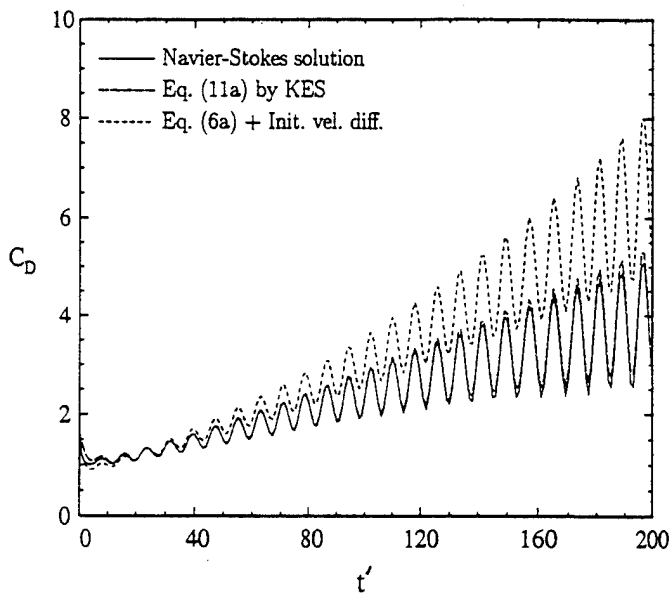


Figure 7. Drag coefficients as a function of time for $Re_{t_0} = 150$ and $\omega' = 0.8$ with $\rho_r = 5$.

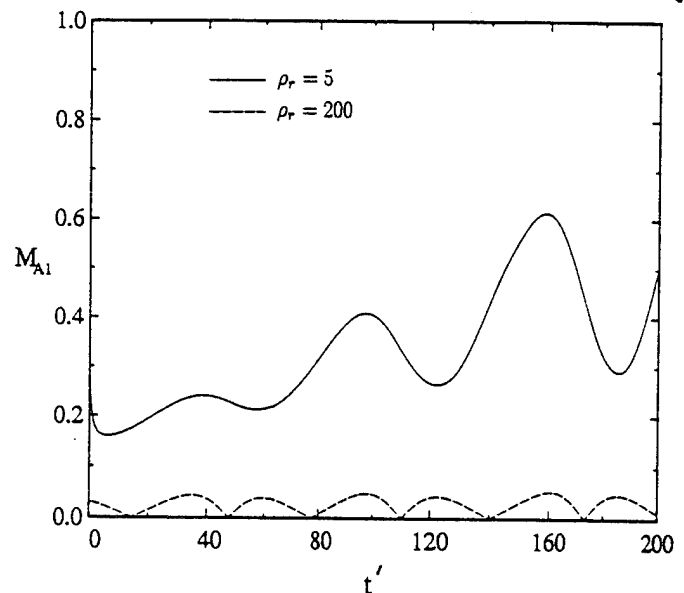


Figure 9. Dimensionless acceleration as a function of time for $Re_{t_0} = 150$ with $\rho_r = 5$ and 200.

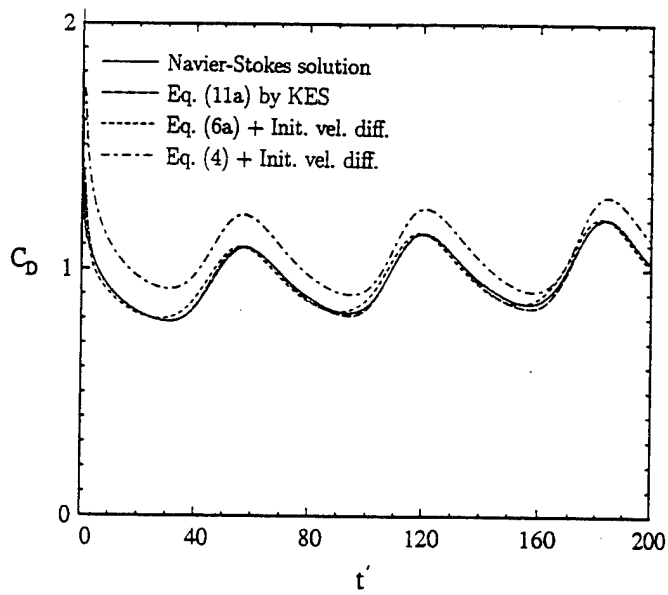


Figure 8. Drag coefficients as a function of time for $Re_{t_0} = 150$ and $\omega' = 0.1$ with $\rho_r = 200$.

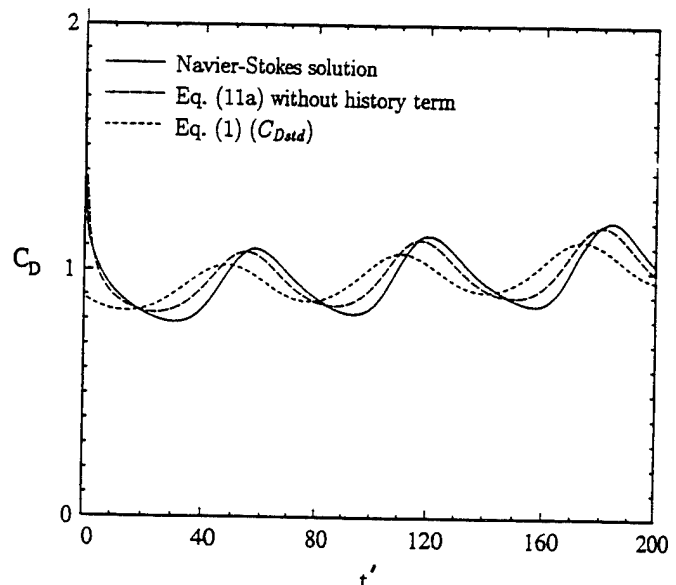


Figure 10. Drag coefficients as a function of time for the same parameters as in Fig. 8 but with different equations.

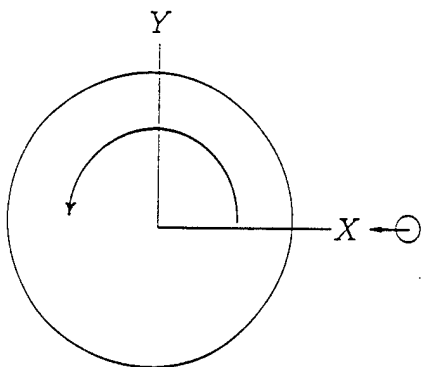


Figure 11. Initial flow geometry for a particle injected into a large vortex tube.

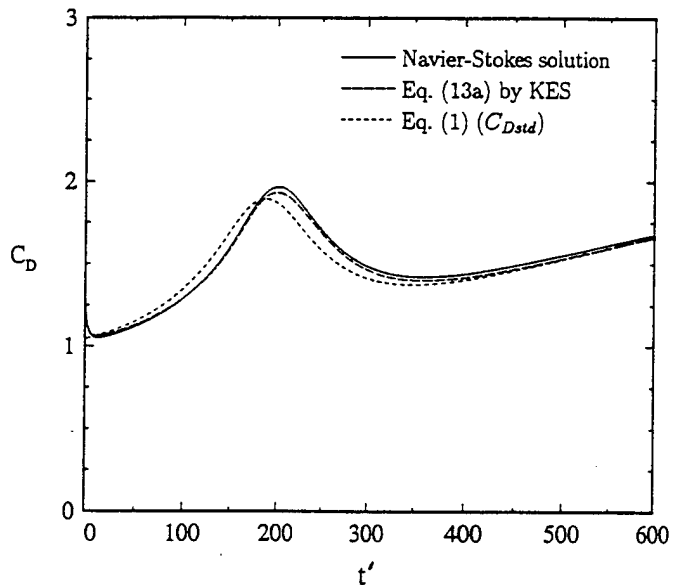


Figure 13. Drag coefficient as a function of time for the same parameters as used in Figure 12.

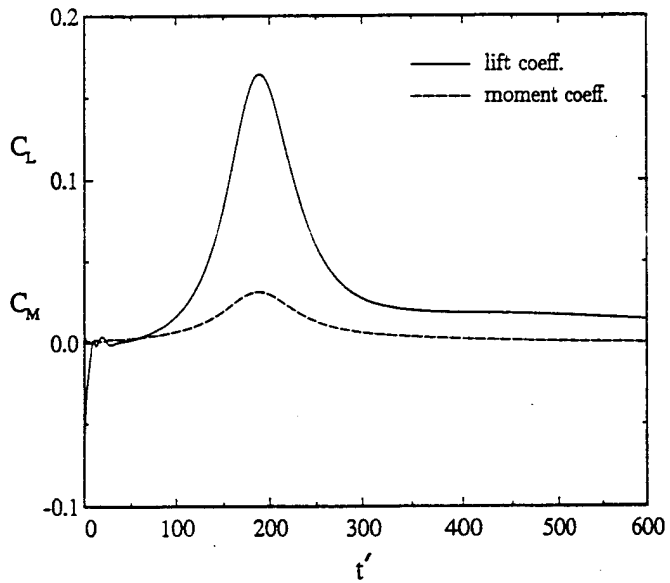


Figure 12. Lift and moment coefficients as a function of time for $Re_{lo} = 108.2$ with $\rho_r = 200$.

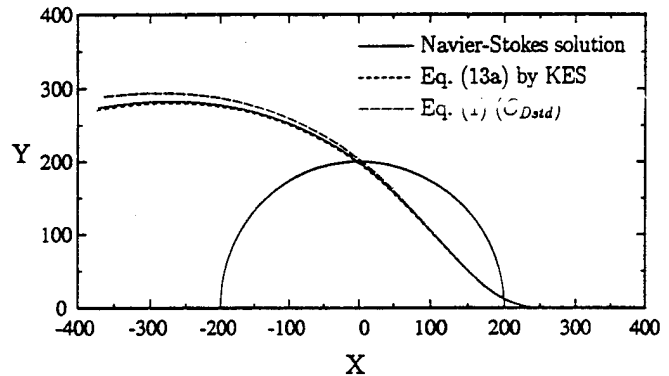


Figure 14. Trajectory of the sphere in the X-Y symmetry plane for the same parameters as used in Figure 12.



ADDENDUM TO SECTION 6

AIAA 96-0087

The Influence of an Advection Vortex on the Heat Transfer to a Liquid Droplet

M. Masoudi and W. A. Sirignano

University of California, Irvine

**34th Aerospace Sciences
Meeting & Exhibit**

January 15-18, 1996 / Reno, NV

The Influence of an Advection Vortex on the Heat Transfer to a Liquid Droplet *

M. Masoudi[†] and W. A. Sirignano[‡]

Department of Mechanical and Aerospace Engineering
University of California, Irvine

Abstract

The three-dimensional interaction of an initially cylindrical vortex tube with a droplet in a uniform stream is investigated through a numerical solution of the Navier-Stokes equations. Particular attention is given to the effect of the vortex on the droplet heat transfer. The transient response of the droplet Nusselt number is sensitive to the geometrical factors that specify the vortex initial position and structure. The time-averaged Nusselt number is approximately the value for the axisymmetric case when the vortex center approaches the droplet along the base flow symmetry axis. Correlation for time-averaged values of Nusselt number is reported. The widely-used correlation for the droplet heat transfer in an axisymmetric flow is corrected to account for the influence of the vortex. Based on our findings, it is speculated that, in a spray combustion system, the vortex-droplet interactions within the Kolmogorov scale can have significant effects on the droplet convective heat transfer.

Nomenclature

a'	dimensional droplet radius, (characteristic length)
d	vortex offset distance from the base flow symmetry axis (normalized by a')
N_1, N_2, N_3	number of grid points in (ξ, η, ζ)
Nu	Nusselt Number
Pc	Peclet number
Pr	Prandtl number
p	pressure
q''	heat flux
r, θ, ϕ	spherical coordinates
Re	base flow Reynolds number (based on droplet diameter)
t	time (normalized by a'/U'_∞)
T	temperature

*Copyright ©1996 by the authors. Published by the American Institute of Aeronautics and Astronautics, Inc. with permission.

[†]Research Assistant, Member AIAA.

[‡]Professor of Mechanical and Aerospace Engineering,
Fellow AIAA.

u, v, w	flow velocities in (x, y, z) directions (normalized by U'_∞)
U'_∞	dimensional free stream velocity, (characteristic velocity)
v_{max}	maximum tangential velocity of vortex tube (normalized by U'_∞)
V	velocity vector
x, y, z	Cartesian coordinates

Greek symbols

(ξ, η, ζ)	computational coordinates
σ	radius of vortex tube (normalized by a')
Γ	vortex tube circulation
ψ	stream function
ν'	kinematic viscosity of the gas-phase
τ	shear stress

<u>Superscript</u>	
'	dimensional quantity

Subscript

o	initial quantity
ax	quantity in the corresponding axisymmetric flow (no vortex)
g	quantity in the gas-phase
l	quantity in the liquid phase
s	droplet surface (gas-liquid interface)
v	vortex quantity

1. Introduction

The fluid dynamics and heat transport for a cold liquid droplet in a hot gaseous axisymmetric environment is a well-understood phenomenon and there exists substantial literature exploring many different aspects of such problems¹. There however is a shortage of literature exploring droplet heating and vaporization when the far-field flow embracing the droplet undergoes temporal and/or spatial variations. Existing literature has focused on variations due to acoustical waves²⁻⁴. Vortical disturbances have not been widely examined.

Such a class of problems appears when the droplet transport properties are subject to velocity and temperature fluctuations in a turbulent flow, such as might occur in a liquid-fueled combustor. In particular, in a spray-droplet system, the droplet size is ~ 100 microns. In the turbulence spectrum for many continuous combustors, this length-scale corresponds to that of the Kolmogorov scale; thus, the droplet transport phenomena can be subject to turbulent effects primarily associated with those of the Kolmogorov scale. Moreover, since turbulence could be represented as a manifestation of vortex dynamics⁵, it is useful to study the effect of an array of vortices on the droplet where the size of the vortices is comparable with that of the droplet. In this work, we have studied the effect of one advecting vortex on a droplet.

2. Flow Description, Governing Equations, and Vortex Characteristics

The solution for the velocity field in this problem has been reported in previous publications^{6,7}. Below, we present a summary of our approach including the governing equations, the boundary and initial conditions, the computational approach, and the reasons necessitating a parameter study.

Consider the three-dimensional, unsteady flow field surrounding and within a cold droplet impulsively injected in a hot gaseous environment with the droplet subsequently subjected to an unsteady interaction with an advecting vortex tube. The problem is non-linear by nature. Fundamental fluid dynamic aspects such as lift, drag, and moment coefficients of the vortex-droplet interaction were reported^{6,7} and thus, here, we concentrate on our recent findings on variations in the droplet heat transfer. Constant properties are assumed in both the gas and the liquid domain and the droplet experiences no vaporization. The deceleration of the droplet due to the drag force is not considered.

Since our goal is to study the flow interaction with a liquid droplet, we solve the governing equations for both the gas and the liquid phase. These are the Navier-Stokes and the thermal energy equations in both phases; the continuity equation is satisfied through pressure correction. The equations and the boundary conditions are non-dimensionalized using the droplet radius a' as the characteristic length, the undisturbed free stream velocity U'_∞ as the characteristic velocity, and the ambient gas temperature T'_g as the characteristic temperature. The governing equations are:

Gas phase

$$\nabla \cdot V_g = 0 \quad (1)$$

$$\frac{DV_g}{Dt} = -\nabla p_g + \frac{2}{Re_g} \nabla^2 V_g, \quad (2)$$

$$\frac{DT_g}{Dt} = \frac{2}{Re_g Pr_g} \nabla^2 T_g, \quad (3)$$

Liquid phase

$$\nabla \cdot V_l = 0 \quad (4)$$

$$\frac{DV_l}{Dt} = -\nabla p_l + \frac{2}{Re_l} \nabla^2 V_l \quad (5)$$

$$\frac{DT_l}{Dt} = \frac{2}{Re_l Pr_l} \nabla^2 T_l \quad (6)$$

These governing equations are transformed to the coordinates (ξ, η, ζ) ; see Fig. 1. ξ is the radial, η is the angular, and ζ is the azimuthal direction. The numerical integration of the equations is performed using a computational cubic mesh with equal spacing ($\delta\xi = \delta\eta = \delta\zeta = 1$).

Gas/Liquid Interface Conditions

The conditions at the interface are based on the principle of continuity of shear stresses (the discontinuity in shear stress across the surface due to surface tension gradient has been shown to be negligible in its impact on droplet heating), zero normal velocity, continuity of tangential velocities, continuity of the heat flux, and continuity of temperature. Since the interface in our flow is always spherical (under the assumption of small Weber number), these conditions are conveniently cast in terms of spherical coordinates (r, θ, ϕ) with its origin at the center of the droplet. The (ξ, η, ζ) coordinates have the same orientation as the spherical coordinates (r, θ, ϕ) but obey an imposed stretching allowing a relatively denser grid concentration near the gas-liquid interface (droplet surface).

$$\begin{aligned} \tau_{l,r\theta,s} &= \tau_{g,r\theta,s} \\ \tau_{l,r\phi,s} &= \tau_{g,r\phi,s} \\ V_{l,\theta,s} &= V_{g,\theta,s} \\ V_{l,\phi,s} &= V_{g,\phi,s} \\ T_{l,s} &= T_{g,s} \\ q''_{l,s} &= q''_{g,s} \end{aligned}$$

Here, $\tau_{r\theta,s}$ and $\tau_{r\phi,s}$ are respectively the shear stresses on a positive r -plane in the positive θ and ϕ direction and q'' is the heat flux from the hot ambient gas into the cold liquid droplet. The interface condition for pressure is obtained from the momentum equation.

Gas-Phase Boundary Conditions

(N_1, N_2, N_3) and (N_{1l}, N_2, N_3) are the number of grid points in the gas and liquid domain, respectively, in (ξ, η, ζ) coordinates. ξ at N_{1l} and N_1 are the droplet surface and the gas far-field, respectively. The imposed far-field pressure, gas velocities in the x, y, z directions and gas temperature are

$$p = 0, u = v = 0, w = 1, T = 1 \quad \text{at } \xi = N_1 \text{ and}$$

$$N_{2mid} \leq \eta \leq N_2 \text{ (upstream)}$$

$$p = 0, \frac{\partial u}{\partial \xi} = \frac{\partial v}{\partial \xi} = \frac{\partial w}{\partial \xi} = \frac{\partial T}{\partial \xi} = 0 \quad \text{at } \xi = N_1 \text{ and}$$

$$1 \leq \eta < N_{2mid} \text{ (downstream)}$$

The imposed initial conditions inside the liquid droplet are a quiescent liquid phase and a uniform temperature $T_{l0} < T_{g0}$.

Symmetry Conditions

Since the cylindrical vortex tube advects with its axis of symmetry parallel to the y -axis, symmetry is maintained such that we solve for half the spherical domain rather than the entire domain, and thus reduce the computational time.

$$\frac{\partial p}{\partial \zeta} = \frac{\partial u}{\partial \zeta} = \frac{\partial w}{\partial \zeta} = \frac{\partial T}{\partial \zeta} = 0; v = 0 \quad \text{at } \zeta = 1, N_3$$

Numerical Solution

A three-dimensional implicit finite-difference algorithm solves the set of discretized partial differential equations. The control volume formulation is used to develop the finite-difference equations. The method of solution employs an Alternating-Direction-Predictor-Corrector (ADPC) scheme to solve the time-dependent equations.

The overall solution procedure is based on a cyclic series of estimate-and-correct operations. At each time-step, we first regard the solution in the gas-phase; the velocity components are first calculated from the momentum equations using the ADPC method, where the pressure field at the previous time step is employed. This estimate improves as the overall iteration continues. The pressure is calculated from the pressure correction equation using the successive overrelaxation method. The new estimates of pressure and velocities are then obtained. These known quantities are used in the energy equation to solve for the gas-phase temperature field.

Next, we use the interface conditions to solve for the liquid-phase boundary values, followed by the sequential, iterative solution of the liquid-phase equations of motion and thermal energy until convergence is achieved for each time step of the calculation.

At each time step, the drag, lift, and moment coefficients and Nusselt number are evaluated. The entire procedure is then repeated for the next time-step. Further details may be found in previous publications of this research group⁶⁻⁸. All the executions were pursued on a Dec-alpha, a Convex 240 and a Convex 3840.

The Vortex Tube Features

The vortex is introduced upstream of the droplet, advects with the superimposed uniform flow, and has a relatively simple configuration—it is an initially cylindrical tube whose axis of symmetry is initially normal to the uniform flow and parallel to the y -axis. The vortex tube has a relatively small central core. Within this core, the initial velocity distribution in the vortex tube is that of solid body rotation reaching an imposed v_{max} at radius σ . v_{max} and σ are specified at time $t = 0$. Outside this inner core, the vortex induces a velocity field of a potential vortex; thus, the velocity induced by the vortex vanishes as $r \rightarrow \infty$. This two-dimensional vortical tube is known as Rankine vortex⁹, and has the following stream function¹⁰:

$$\psi_v(x, z, t = 0) = -\frac{\Gamma_0}{2\pi} \ln[(x - x_0)^2 + (z - z_0)^2 + \sigma_0^2] \quad (7)$$

where Γ_0 is the initial non-dimensional vortex circulation at radius σ_0 . Γ_0 is positive when the vortex tube has counterclockwise rotation, and x_0 and z_0 denote the initial location of the center of the vortex tube. Note the vortex tube circulation at radius σ is $\Gamma = 2\pi\sigma v_{max}$. More fundamental information on the vortex tube such as temporal changes in its tangential velocity and vorticity are given in Ref. [6].

Flow Interaction

The droplet is placed in a uniform flow (here also called the ‘base flow’) and thus gradually develops a standing vortex ring in its aft position. Note that, in the absence of the vortex, the flow remains axisymmetric with respect to the z -axis (Fig. 1). The vortex is introduced 10 droplet radii upstream of the droplet and advects with the superimposed uniform flow; it takes about 10 residence time units for the vortex to arrive at the vicinity of the droplet;

there, we observe vortex stretching in the cross-flow direction and thus a full unsteady and three-dimensional interaction occurs between the vortex and the droplet. The dynamic interaction is the strongest when the vortex is initially introduced ‘on’ the base flow symmetry axis of Fig. 1; here, a ‘head-on’ collision between the droplet and the vortex is observed, resulting in vortex stretching in the cross-flow direction. When the vortex advects ‘off’ the axis, the dynamic interaction between the two is relatively weaker. It takes nearly 25 Residence time units for the vortex to arrive at the droplet, interact with it, and then travel sufficiently far downstream to have insignificant influence. Many details of the interactions have been reported in Ref. [6]. Figs. (2) show how the velocity and thermal boundary layers, both in the gas phase and within the droplet interior, could be affected due to the advection of the vortex near the droplet. Naturally, and as observed, a more pronounced departure from the axisymmetric case is expected in the gas phase.

The Droplet Convective Heat Transfer

The droplet convective heat transfer, represented by its Nusselt number, is computed through $Nu(t) = 2a'h'/k_g'$ (with h' and k_g' being the convective heat transfer coefficient and the gas conductivity) which after a standard simplification and non-dimensionalization yields

$$Nu(t) = \frac{\int_0^\pi \int_0^\pi \frac{\partial T_g(t)}{\partial r}|_s \sin\theta d\theta d\phi}{\pi(1 - \bar{T}_s)}$$

where \bar{T}_s is the droplet temperature at the interface averaged over the surface. Since the cold droplet is injected impulsively in the hot ambient gas, it initially experiences a stronger heat transfer. In the base axisymmetric flow, it takes nearly 5 resident time units for the droplet Nusselt number to reach a steady value. However, when the vortex is superimposed on the base flow, the Nusselt number fluctuates continuously due to the advection of the vortex and can not attain a steady value. It is therefore more convenient to regard overall estimates by considering time-averaged values according to

$$\bar{Nu} = \frac{1}{t_2 - t_1} \int_{t_1}^{t_2} Nu(t) dt \quad (8)$$

It is further advantageous to normalize \bar{Nu} using its corresponding value in an axisymmetric flow \bar{Nu}_{ax} ; we will thus consider \bar{Nu}/\bar{Nu}_{ax} in our results. Also, in the above estimates, $t_1 = 2$ and $t_2 = 25$; i.e. we disregard the data for $t \in (0, 2)$; this is the

time needed for the initial computational fluctuations in the pressure drag to vanish. Since we also estimate the normalizing value \bar{Nu}_{ax} after this initial data exclusion, the final quantity \bar{Nu}/\bar{Nu}_{ax} is barely changed; (sample comparison shows the effect of the initial data exclusion in \bar{Nu}/\bar{Nu}_{ax} is less than .05%).

3. Results

There are four parameters that characterize the quantitative significance of the vortex-droplet interaction: the vortex initial core size (σ_0), its initial maximum tangential velocity (v_{0max}), the offset distance d_0 between the vortex initial position and the base flow symmetry axis (d_0), and the base flow Reynolds number (Re). We place the initial position of the vortex center 10 droplet radii upstream the droplet, either ‘on’ the base flow symmetry axis ($d_0 = 0$) or slightly ‘off’ it ($d_0 = \pm 1, \pm 2, \dots$). A positive or negative d_0 means an offset distance from the z -axis in the x, z symmetry plane in the positive or negative x direction, respectively; this is shown in Fig. 1 with d_0 non-dimensionalized by the droplet radius.

We specify an initial radius (σ_0) for the vortex which defines the vortex core within which vorticity is uniformly distributed; we pick the strength of this vorticity so that the maximum velocity at the core of the vortex (v_{0max}) represents an acceptable fluctuation from the uniform flow. This fluctuation is taken to be less than the free stream velocity. For example, to represent a 20% fluctuation in the base flow, we pick $v_{0max} = .2$. Outside the inner core, the velocity pattern is that of a potential vortex. Thus, the vortex structure and strength are initially fully characterized by the two parameters σ_0 and v_{0max} , non-dimensionalized by the droplet radius and the strength of the uniform stream, respectively. Fig. 1 shows the vortex location upstream of the droplet. Since in the absence of the vortex the base flow remains axisymmetric at all times, a change in the orientation of the vortex circulation only rotates the spatial orientation of the events; so, we arbitrarily pick the counterclockwise orientation for the vortex in all our simulations. A counterclockwise rotation with a positive offset distance is the mirror image of a clockwise rotation with a negative offset distance so that clockwise rotation need not be considered.

In order to investigate the droplet heat transfer influenced by the flow fluctuations due to the passage of the vortex, we pursue a parameter study to determine the role of each of the four above characteristics on the droplet Nusselt number. In the following sections, we report observations and resulted correlation for Nusselt num-

ber affected by these four parameters. The considered ranges are $d_0 = 0, \pm 1, \pm 2, \pm 3, \pm 4, \pm 5$; $\sigma_0 = .25, .5, 1, 2, 3, 4$; $v_{0max} = .1, .2, .3, .4$, and $20 \leq Re \leq 100$.

The Effect of the Offset Distance

Figures 3(a,b) show the temporal changes in Nusselt number as a function of vortex center initial position (d_0) upstream the droplet. The droplet Nusselt number in an axisymmetric flow (i.e. having the same Reynolds number and without a vortex) is also shown for comparison. The substantial difference in the temporal response is apparent. The droplet Nusselt number increases for $d_0 > 0$ and decreases for $d_0 < 0$; a vortex with a counterclockwise circulation, when positioned at an initial $d_0 > 0$, increases the relative gas-droplet velocity in the vicinity of the droplet and thus increases its convective heat transfer; by contrast, one with $d_0 < 0$ decreases the convective heating of the droplet.

An interesting case is that of $d_0 = 0$ where the droplet Nusselt number goes through a pattern of increase-decrease-increase depending upon the vortex location while advecting. This pattern for $d_0 = 0$ is seen in Figs. 3(a,b). When the vortex is upstream of the droplet, its counterclockwise circulation increases the convective effect, and thereby the droplet Nusselt number; very near the droplet, viscous interactions force it to pass ‘underneath’ the droplet⁶. (‘underneath’ means in the lower half of the x, z symmetry plane in Fig. 2.) In the droplet vicinity, the vortex reduces the convective effect decreasing the droplet Nusselt number. When downstream of the droplet, the vortex once again strengthens the convective effect and increases the droplet Nusselt number.

Moreover, when the vortex is initially positioned on the base flow symmetry axis ($d_0 = 0$), an increase in Nusselt number is followed by a decrease and thus the summed variations yielding \overline{Nu} are small; by contrast, the non-trivial changes in \overline{Nu} occur when $d_0 \neq 0$. The measured values in such case suggest that $\overline{Nu}/\overline{Nu}_{ax} - 1 \sim \tanh(d_0)$; this is shown in Fig. 3(c).

Note also that, in spite of sensitivity of $Nu(t)$ to the passage of the vortex (Fig. 3(a,b)), $\overline{Nu}/\overline{Nu}_{ax} - 1$ is nearly invariant to the vortex for $2 \leq |d_0| \leq 5$ (Fig. 3(c)).

The Effect of the Vortex Tangential Velocity

Figures 4(a,b) show the influence of v_{0max} on temporal Nusselt number when the vortex advects on ($d_0 = 0$, Fig. 4(a)) or off ($d_0 \neq 0$, Fig. 4(b)) the base flow symmetry axis; the corresponding pattern in an axisymmetric flow with the same Reynolds

number has been also shown for comparison. Since $\Gamma_v \propto v_{max}$, vortices with larger v_{max} induce a stronger secondary flow in the uniform stream; thus, droplet Nusselt number shows sensitivity to the vortex v_{0max} .

However, changes in \overline{Nu} due to v_{0max} appear to be small for as long as $d_0 = 0$; (see Fig. 4(a)). This is the same as the previous observation that, as long as $d_0 = 0$, the vortex effect on $Nu(t)$ is sometimes augmenting and sometimes decreasing, yielding trivial changes from the axisymmetric value in \overline{Nu} . This was also seen when studying the effect of d_0 . The observed negligible changes in \overline{Nu} should not be interpreted as the insensitivity of the droplet heat transfer to the passage of the vortex or the vortex v_{0max} ; simply stated, at $d_0 = 0$, we find cancellations in the averaging process. This cancellation is not encountered in computing \overline{Nu} when $d_0 \neq 0$, such as the cases shown in Fig. 4(b); later, we will discuss this more interesting effect of vortex velocity that occur when $d_0 \neq 0$.

Data indicate that, overall, $\overline{Nu}/\overline{Nu}_{ax} - 1$ nearly follows a linear dependence on v_{0max} .

The Effect of the Vortex Radius

Figures 5(a,b) show the influence of σ_0 on temporal Nusselt number when the vortex advects on ($d_0 = 0$, Fig. 5(a)) or off ($d_0 \neq 0$, Fig. 5(b)) the base flow symmetry axis; the corresponding pattern in an axisymmetric flow with the same Reynolds number has been also shown for comparison.

Analogous to the previous observation, since $\Gamma_v \propto \sigma$, vortices with larger radii introduce stronger secondary flow in an otherwise uniform stream near the droplet; thus, droplet Nusselt number appears sensitive to change in the vortex radius. When the vortex advects on the base flow symmetry axis ($d_0 = 0$), in spite of the clear temporal sensitivity, the time-average values of Nusselt number compared to those in an axisymmetric flow (having the same Reynolds number) change by only .5% when $v_{0max} = .2$ and by about 1% when $v_{0max} = .4$ so that we may note $\overline{Nu}/\overline{Nu}_{ax} = 1 \pm 1\%$. Similar to the case in the previous section, the trivial net change in the computed \overline{Nu} in such cases is due to a combined effect of $d_0 = 0$ in the simulation and the nature of time-averaging of Eqn. (8); it should not be interpreted as the insensitivity of the droplet convective heat transfer to the passage of the vortex, (see Fig. 5(a)).

Thus, when studying the effect of σ_0 on $\overline{Nu}/\overline{Nu}_{ax}$, larger values are resulted when the vortex advects off the base flow symmetry axis, (Fig. 5(b)); later, we shall discuss this effect of vortex radius at $d_0 \neq 0$. Data indicate that $\overline{Nu}/\overline{Nu}_{ax} - 1$ has a slightly stronger dependence on σ_0 than it does on v_{0max} .

The Effect of the Flow Reynolds Number

Figures 6(a,b) show the influence of the base flow Reynolds number on the temporal Nusselt number when the vortex advects on ($d_0 = 0$, Fig. 6(a)) or off ($d_0 \neq 0$, Fig. 6(b)) the base flow symmetry axis; the corresponding pattern in an axisymmetric flow with the same Reynolds number has been also shown for comparison.

The higher the Reynolds number, the stronger the heat transfer fluctuations induced by the vortex, even though the strength of the vortex remains the same; thus, for example, a 30% fluctuations (i.e. $v_{0max} = .3$) in a uniform flow with $Re = 100$ has a stronger effect on the droplet Nusselt number than the same fluctuation does in a flow with $Re = 20$. The reason is simple: flows with lower Reynolds numbers are relatively more viscosity-dominated and thus vortex-induced inertial changes are relatively more damped.

Analogous to the previous observations, when $d_0 = 0$ (Fig. 6(a)), there is barely change in time-averaged values of Nusselt number due to change in base flow Reynolds number; $\overline{Nu}/\overline{Nu}_{ax} - 1$ changes over the range of Reynolds number by only .1% when $v_{0max} = .2$ and by .5% when $v_{0max} = .4$. Again, this is mostly the consequence of the choice $d_0 = 0$ and the nature of time-averaging in Eqn. (8). Naturally, when $d_0 \neq 0$ (Fig. 6(b)), the computed changes in $\overline{Nu}/\overline{Nu}_{ax} - 1$ are stronger; such effects are seen in Fig. 6(b) and will be discussed in the next section.

Data indicate that $\overline{Nu}/\overline{Nu}_{ax} - 1 \sim Re^{0.5}$; note since $\overline{Nu}_{ax} \sim Re^a$, where the exponent ranges from .427 to .573 (see Appendix), so that approximately $\overline{Nu} - \overline{Nu}_{ax} \sim Re$. This implies that the time-averaged perturbations in Nusselt number have a stronger dependence on Reynolds number than Nusselt number itself does.

Global Self-Similarity

In the absence of the vortex, Nu and Nu_{ax} are identical, and one may approximate the Nusselt number correlation from Ref.[11] for a spherical droplet in an axisymmetric flow by using the solid sphere correlation⁴

$$Nu = 1 + (1 + Pr Re)^{1/3} Re^{0.77} \quad (9)$$

or one may use the new correlation for axisymmetric flow past liquid spheres presented in the Appendix. With the vortex present near the droplet, however, the axisymmetric flow correlation loses its applicability and a new correlation accounting for the effect of the advecting vortex on the droplet heat transfer is to be used.

We have produced a correlation that includes such effects; all our data collapse into the functional form

$$\begin{aligned} \frac{d_0}{\sigma_0} < -2 : \quad \frac{\overline{Nu}}{\overline{Nu}_{ax}} &= 1 - .008 \left(\frac{\Gamma_0}{2\pi} \right)^{0.9} Re^{0.5} \\ -2 \leq \frac{d_0}{\sigma_0} \leq 2 : \quad \frac{\overline{Nu}}{\overline{Nu}_{ax}} &= 1 + \\ &.010 \sigma_0^{0.2} \frac{\Gamma_0}{2\pi} Re^{0.5} \tanh(0.78 \frac{d_0}{\sigma_0}) \\ \frac{d_0}{\sigma_0} > 2 : \quad \frac{\overline{Nu}}{\overline{Nu}_{ax}} &= 1 + .008 \left(\frac{\Gamma_0}{2\pi} \right)^{0.9} Re^{0.5}. \end{aligned} \quad (10)$$

within the range of our parameter study, $20 \leq Re \leq 100$; $.25 \leq \sigma_0 \leq 4$, $.1 \leq v_{0max} \leq .4$, $-5 \leq d_0 \leq 5$. All our simulations are for an n-octane droplet and so $Pr_l = 8.527$. (For all values of Re in the given range, we have verified the above correlation for $|d_0/\sigma_0| \leq 2$; work is under way to confirm fully the correlation for $|d_0/\sigma_0| > 2$, as well.) Modest modification (< 10%) to the exponents is made by a least-squares fit. The correlation coefficient for the above fit is .985. A plot of this correlation and its comparison with our data is shown in Figs. 7(a,b).

The significance of the our observation should not be underestimated for the following reason: note that the problem at hand is unsteady by nature; by contrast, it has been well-established that majority (but not all) of self-similar patterns in fluid flows and their coupled heat transfer mechanisms establish themselves when the transient response has vanished and only when the equilibrium stage has established itself. The observation made from Eqn. (10) and Figs. 7(a,b) reveals however that, in spite of the unsteady nature of vortex-droplet interaction, self-similar correspondence nevertheless exist in the time-averaged behavior.

4. Conclusions

We have investigated the unsteady interaction between a cylindrical vortex tube and a liquid droplet in a uniform flow by pursuing a study of each of the four parameters affecting the strength of this interaction and the modification of the droplet Nusselt number. We have paid particular attention to the effect of these parameters on the transient and time-averaged values of the droplet Nusselt number. A correlation quantifying the effect of the advecting vortex on the droplet heating has been produced. The reported correlation compliments the existing ones for droplet heating in axisymmetric flows that occur in the absence of an advecting vortex¹¹.

When the vortex advects towards and then past the droplet starting upstream 'on' the symmetry axis of the base flow, the droplet Nusselt number first increases and then decreases in time; thus, the

time-averaged Nusselt number is nearly equivalent to that in an axisymmetric flow even when the vortex simulates up to 40% fluctuation in the base flow. Conversely, when the vortex advects 'off' the base flow symmetry axis, time-averaged Nusselt number is changed due to the vortex-induced fluctuations; whether this has an augmenting or inhibiting effect on the droplet heating depends on two factors: the vortex circulation orientation and also whether it advects 'above' or 'below' the symmetry axis in the plane of symmetry. Time-averaged Nusselt number monotonically varies with the ratio of the vortex initial offset distance to the vortex initial core size varying from 0 to 2 (i.e. $0 \leq |d_0/\sigma_0| \leq 2$); when this ratio is greater than 2, time-averaged Nusselt number remains nearly unchanged (Figs. 7).

In the range $0 \leq |d_0/\sigma_0| \leq 2$, change in the droplet Nusselt number has a linear dependence on the vortex circulation, a weak dependence on the vortex initial core size, and $\sim \tanh(d_0/\sigma_0)$. We believe this occurs because, when the vortex arrives at the vicinity of the droplet, the droplet is encompassed, partly or wholly, within the vortex inner core; thus, the perturbations in flow configuration depend on both the vortex core size and its circulation. (Dependence on the vortex initial maximum tangential velocity is embedded within the dependence on the vortex circulation.)

The situation is different when $|d_0/\sigma_0| > 2$: when the vortex arrives at the vicinity of the droplet, the droplet is totally outside the vortex inner core and thus it is 'only' the vortex circulation that matters to the droplet. Thus, it is not surprising that the computed fluctuations in this range in Eqn. (10) only depend on the vortex circulation.

We emphasize that, in parallel studies investigating changes in fluid dynamic properties of solid spheres (lift and moment coefficients)⁶, similar dependence of fluctuations in fluid dynamic properties on vortex parameters have been observed. When the vortex advects near the sphere, the induced fluctuations appear to depend both on the vortex size and its circulation; by contrast, with the vortex advecting relatively far from the sphere, the changes appear to depend only on vortex circulation. Marked dependence of Nusselt number fluctuations on the fluid dynamics variations explains the similarity between the conclusions of the two studies.

A rather surprising observation here is that, while in the absence of vortical structures $Nu_{ax} \approx O(Re^{0.5})$ thus prompting one to anticipate its perturbations $\overline{Nu} - Nu_{ax} \approx O(Re^{0.5})$ as well, our observations here show that this is *not* the case; instead, the induced perturbations follow $\approx O(Re)$.

Based on our findings, it is speculated that, in a spray combustion system, the vortex-droplet interactions within the Kolmogorov scale can have signif-

icant effects on the droplet convective heat transfer.

Acknowledgement

This work has been supported by the Air Force Office of Scientific Research under grant No. F49620-93-1-0028 with Dr. Julian Tishkoff acting as the technical monitor. We thank Professor S. Elghobashi for his comments on the self-similar correlation. The support of the University of California, Irvine, Office of Academic Computing through the use of their Convex C3840 and the help of Mr. Donald Frederick and Dr. Allen Schiano are gratefully appreciated.

Appendix

In an axisymmetric flow, and following the assumption that the effect of the droplet internal circulation on the droplet heating is small, one may use the Nusselt number correlation from Ref.[11] for a rigid sphere

$$Nu = 1 + (1 + Pr Re)^{1/3} Re^{0.077} \quad (11)$$

for $Re \leq 400$. This correlation has been recommended for spray combustion computations⁴. For particles having $Re \geq 10$ in media with $Pr \approx 1$, this suggests $Nu - 1 \sim Re^{0.410}$.

We have modified this suggested correlation by accounting for the droplet internal circulation. Our calculations (n-octane droplet in air, $10 \leq Re \leq 100$) suggest that a fit of the form

$$Nu - 1 = .927 Re^{0.427} \quad 10 \leq Re \leq 100. \quad (12)$$

The authors note, however, that this form is somewhat clumsy since one should expect $Nu = 2$ at $Re = 0$. A preferred fit therefore is

$$Nu - 2 = .412 Re^{0.573} \quad 10 \leq Re \leq 100. \quad (13)$$

Each of these fits has a correlation coefficient greater than .99.

It is suggested that the slight increase in the exponent of Re (compared to the exponent .410 resulted from Eqn. (11)) is a contribution of the droplet internal circulation. That is, the boundary layer and thermal layer thicknesses are decreased slightly due to the motion along the interface. This results in an increase in heat transfer rate from the hot ambient gas to the cold droplet.

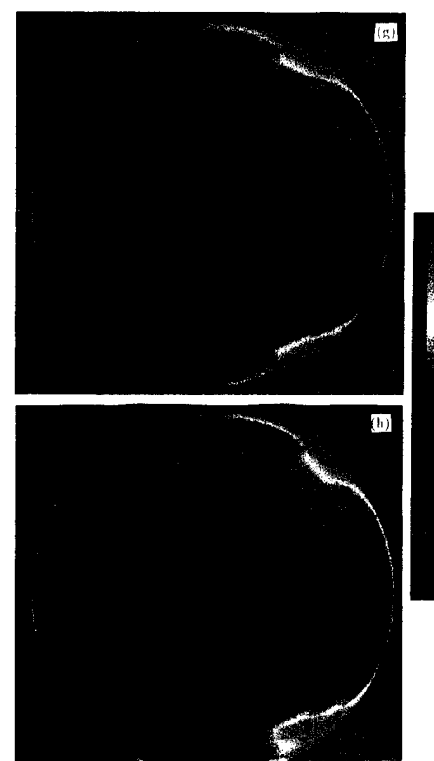
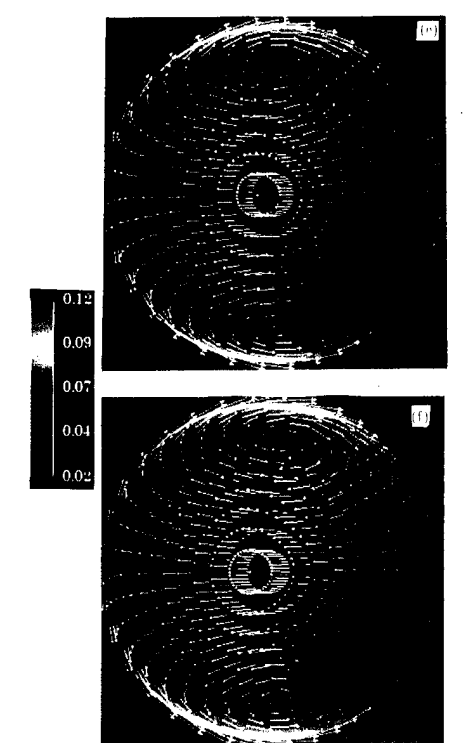
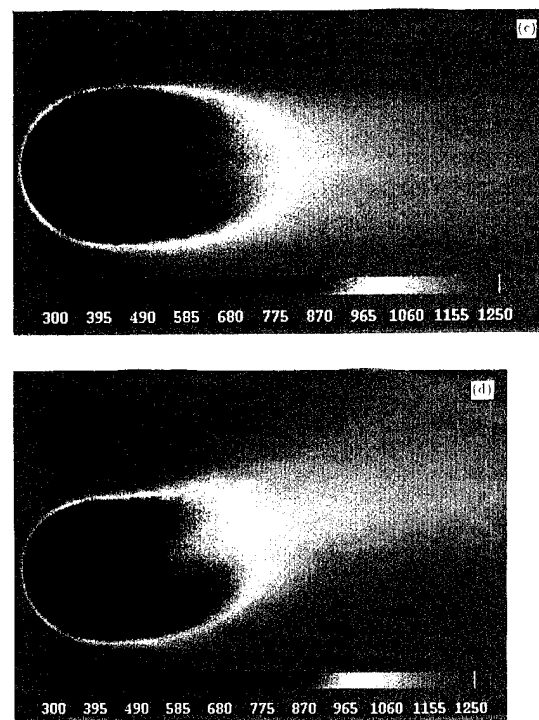
References

- [1] Sirignano, W. A. 1993 Fluid Dynamics of Sprays - 1992 Freeman Scholar Lecture. *J. Fluids Eng.* **115**, N3, 345-378.
- [2] Tong, A.Y. & Sirignano, W. A. 1989 Oscillating Vaporization of Fuel Droplets in an Unstable Combustor. *J. Propulsion and Power* **5**, 257-261.
- [3] Duvuur, A., Chiang, C.H. & Sirignano, W. A. 1996 Oscillating Fuel Droplet Vaporization: Driving Mechanism for Combustion Instability. *J. Propulsion and Power* In press.
- [4] Abramzon, B. & Sirignano, W.A. 1989 Droplet Vaporization Model for Spray Combustion Calculations. *Int. J. Heat Mass Transfer* **32**, 9, 1605-1618.
- [5] Chorin, A.J. *Vorticity and Turbulence*. Springer-Verlag, 1994.
- [6] Kim, I., Elghobashi S. & Sirignano, W. A. 1995 Unsteady Flow Interactions Between an Advecting Cylindrical Vortex Tube and a Spherical Particle. *J. Fluid Mech.* **288**, 123-155.
- [7] Kim, I., Elghobashi S. & Sirignano, W. A. 1995 Unsteady Flow Interactions Between a Pair of Advected Cylindrical Vortex Tubes and a Rigid Sphere. AIAA Aerospace Sciences Meeting, Paper 95-0105.
- [8] Kim, I., Elghobashi S. & Sirignano, W. A. 1993 Three-dimensional Flow Over Two Spheres Placed Side by Side. *J. Fluid Mech.* **246**, 465-488.
- [9] Saffman, P.G. *Vortex Dynamics*. Cambridge University Press, 1992.
- [10] Spalart, P. R. 1982 Numerical simulation of separated flows. Ph. D. Dissertation, Stanford University.
- [11] Clift, R., Grace, J.R., Weber, M.E. *Bubbles, Drops, and Particles*. Academic Press, 1978.

Velocity Boundary Layer



Thermal Boundary Layer



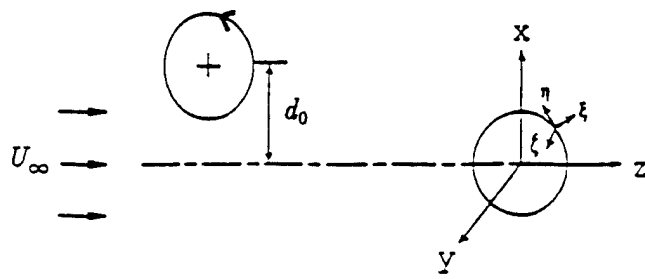
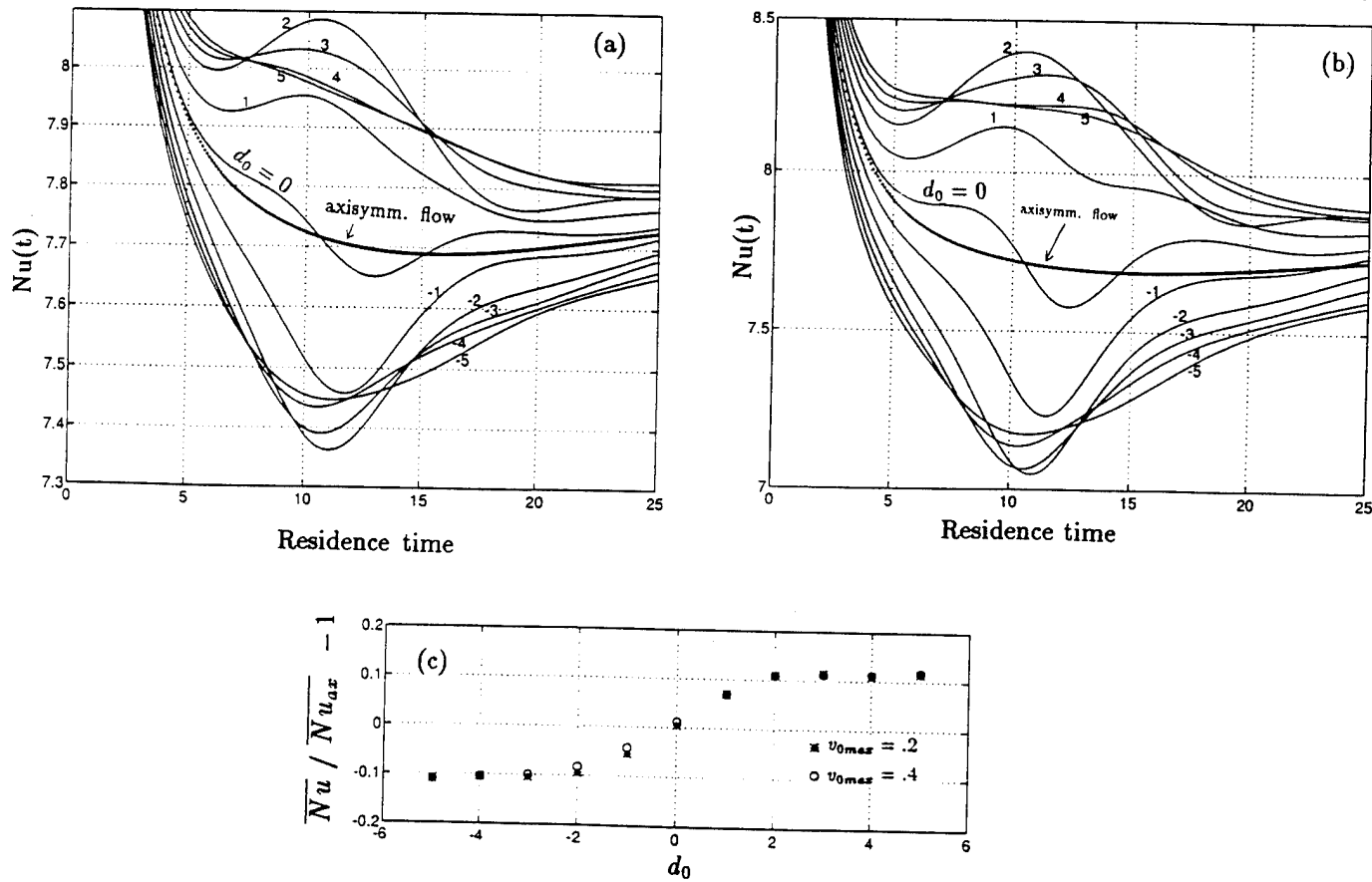


Fig. 1. Flow geometry and coordinates.

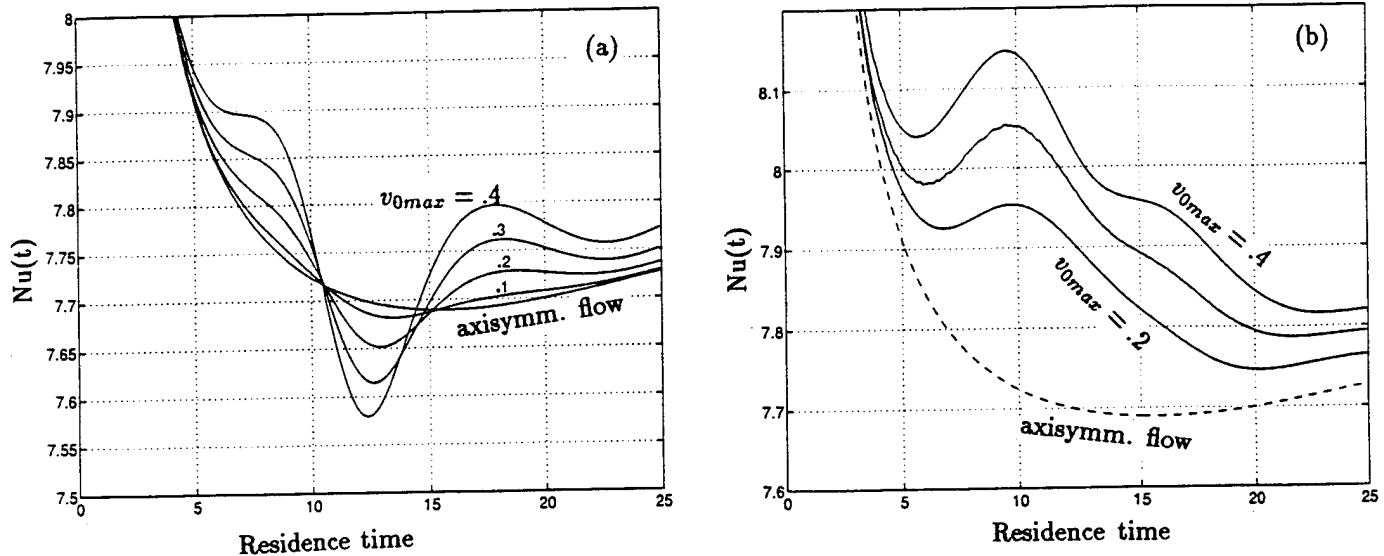
Fig. 2. (Previous page.) Influence of an advecting vortex on the velocity and thermal boundary layers of a moving cold droplet in a hot gas ($d_0 = 2$, $\sigma_0 = 4$, $v_{0\max} = .4$, $Re = 100$, $t = 10.5$).

- (a) gas phase velocity field, axisymm. case.
- (b) same, affected by an advecting vortex.
- (c) gas phase thermal field, axisymm. case.
- (d) same, affected by an advecting vortex.
- (e) liquid interior velocity field, axisymm. case.
- (f) same, affected by an advecting vortex.
- (g) liquid interior thermal field, axisymm. case.
- (h) same, affected by an advecting vortex.



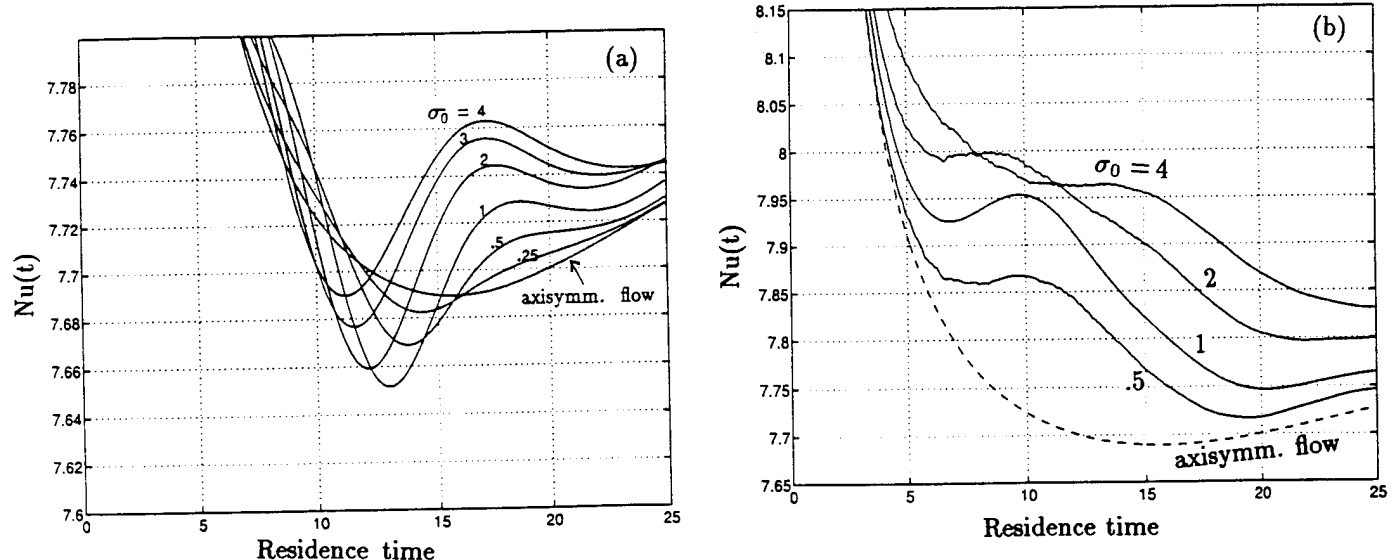
Figs. 3. (Previous page.) Influence of the vortex initial offset distance (d_0) on $Nu(t)$:

- (a) vortex advecting with d_0 in $-5 \leq d_0 \leq 5$, ($\sigma_0 = 1$, $Re = 100$, $v_{0max} = .2$);
- (b) same, $v_{0max} = .4$;
- (c) appearance of $\frac{Nu}{Nu_{ax}} - 1 \sim \tanh(d_0)$.



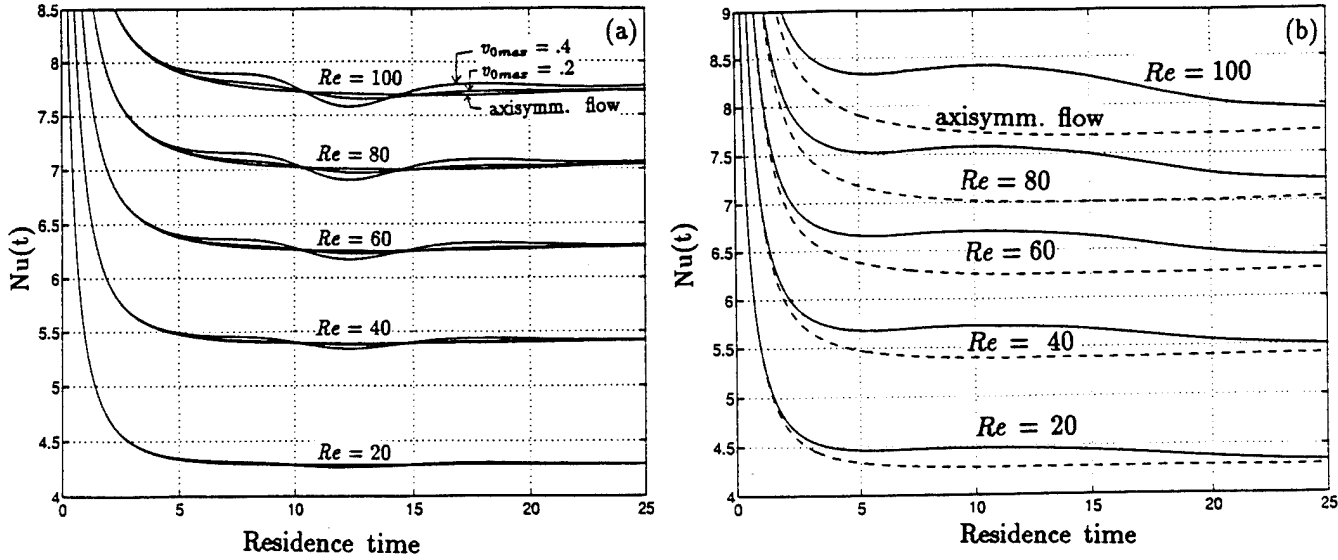
Figs. 4. Influence of the vortex initial tangential velocity (v_{0max}) on $Nu(t)$:

- (a) vortex advecting with $d_0 = 0$, ($Re = 100$, $\sigma_0 = 1$);
- (b) same, $d_0 = 1$.



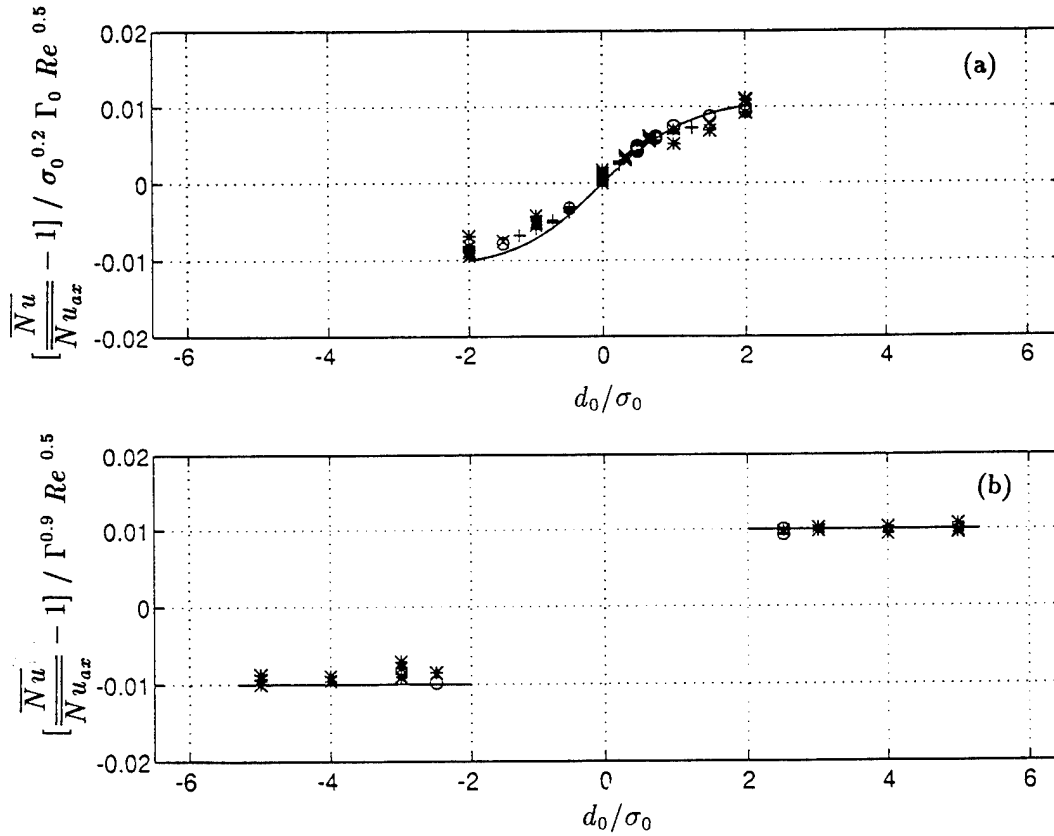
Figs. 5. Effect of the vortex initial radius (σ_0) on $Nu(t)$:

- (a) vortex advecting with $d_0 = 0$, ($Re = 100$, $v_{0max} = .2$);
- (b) same, $d_0 = 1$.



Figs. 6. Effect of the flow Reynolds number on $Nu(t)$:

- (a) vortex advecting with $d_0 = 0$, $(v_{0max} = .2, \sigma_0 = 1)$;
- (b) vortex advecting with $d_0 = +2$, $(v_{0max} = .3, \sigma_0 = 3)$.



Figs. 7. Existence of self-similarity in time-averaged fluctuations in Nusselt number (Eqn. 10):

- (a) in the range $0 \leq |d_0/\sigma_0| \leq 2$;
- (b) in the range $|d_0/\sigma_0| > 2$. Both figures include $-5 \leq d_0 \leq +5$, $0.1 \leq v_{0max} \leq 0.4$, $1 \leq \sigma_0 \leq 4$, $20 \leq Re \leq 100$.